2009

Dense Spectral Beam Combining With Volume Bragg Gratings In Photo-thermo-refractive Glass

Oleksiy Andrusyak
University of Central Florida

DENSE SPECTRAL BEAM COMBINING WITH VOLUME BRAGG GRATINGS IN PHOTO-THERMO-REFRACTIVE GLASS

by

OLEKSIY G. ANDRUSYAK
M.S. University of Central Florida, 2004

A dissertation submitted in partial fulfillment of the requirements
for the degree of Doctor of Philosophy
in the College of Optics and Photonics
at the University of Central Florida
Orlando, Florida

Spring Term
2009

Major Professor: Leonid B. Glebov

ABSTRACT

Beam combining techniques have become an important tool in the design of high-power high-brightness laser systems. Spectral beam combining (SBC) is an incoherent combining technique that does not require phase control of sources, allowing for a stable and robust system. Using SBC, beams from an array of lasers with each element operated at a different wavelength are combined into a single near-diffraction-limited beam with the same aperture using dispersive optical elements. SBC by means of volume Bragg gratings (VBGs) utilizes unique spectral response of VBGs: diffraction efficiency is close to unity when the Bragg condition is satisfied and is close to zero at multiple points corresponding to particular wavelength offsets from Bragg condition. High-efficiency VBGs can be recorded in UV-sensitive photo-thermo-refractive (PTR) glass. Narrow-band reflecting VBGs allow multi-channel SBC with high spectral density of channels.

In this dissertation, experimental results of SBC with high spectral density of combined channels in two spectral regions of interest (1064 and 1550 nm) are reported. The behavior of narrow-band VBGs under high-power laser radiation is investigated. A laser system with kW-level output power and near-diffraction-limited divergence of spectrally-combined output beam is demonstrated. The system combines five randomly-polarized Yb-doped fiber lasers with 0.5 nm spectral separation in central wavelengths using narrow-band reflecting VBGs with absolute efficiency of combining > 90%.

A novel design of a multi-channel high-power SBC system is suggested. In this approach, a common-cavity is created for all channels such that wavelengths of the sources are passively controlled by the combination of a common output coupler and intra-cavity VBGs which also act as combining elements. Laser wavelengths are automatically selected to match resonant wavelengths of respective VBGs. We report successful demonstration of a passively-controlled SBC system consisting of two amplifiers in a common cavity configuration.

A compact and rugged monolithic SBC module based on multiplexed VBGs is introduced. Experimental results of a four-channel implementation of such module are discussed. Modular design of high-power laser systems is suggested with multiple modules arranged in a series. We show that with basic combining parameters achieved up to date, laser systems with 10 kW output power can be constructed using this arrangement. Further scaling to 100 kW power level is discussed.

To my dear parents,

Andrusyak Georgiy Samuilovich and Keller Valentina Sergiivna

Шановні батьки, низький Вам уклін і многая лета!

PREFACE

The research forming the main body of this dissertation was performed at the Photoinduced Processing Laboratory within CREOL, The College of Optics and Photonics, University of Central Florida from 2005 to 2008. This research was performed under supervision of Dr. Leonid Glebov, Research Professor and head of the Photoinduced Processing Laboratory and Dr. George Venus, Research Scientist and head of the Applications Group within this laboratory. Academic supervision was kindly provided by Dr. Boris Zeldovich, Professor of Optics and Physics.

The research presented in the Appendix is not directly related to the topic of the present dissertation, however it is included for it's novelty and promising future prospects. This work was performed at the Nonlinear Optics Laboratory within the Centre de Physique Moleculaire Optique et Hertzienne, University of Bordeaux 1 and ALPhANOV - Centre Technologique Optique et Lasers in 2008-2009. This research was supervised by Dr. Lionel Canioni, Assistant Professor and head of the Nonlinear Optics Laboratory. Academic supervision was kindly provided by Dr. Laurent Sarger, Professor of University of Bordeaux 1.

The dissertation is based on publications by the author with other members of the research group [1-16]. Other publications by the author [17-23], although not directly related to the topic of this dissertation, have resulted in his development as a research scientist. The author has presented results of this research at more than a dozen international scientific conferences.

ACKNOWLEDGEMENTS

First, I would like to extend my deepest gratitude to Dr. Leonid B. Glebov for accepting me into his group and bringing me to a new level of academic and professional development. Thank you for providing my stipend and tuition and awarding me with opportunities to present at world's best conferences and to take part in research exchange program with University of Bordeaux. I have learnt a great deal from you and you have become a role model for me in many respects.

I want to thank Dr. George Venus for being a perfect research supervisor. Your fresh ideas were invaluable at times when it seemed like nothing will work in my experiments. There should be a footnote on every page of this dissertation with credits to George Venus.

I thank my UCF dissertation committee, Dr. Boris Ya. Zeldovich, Dr. Michael Bass, and Dr. Peter Delfyett, my University of Bordeaux jury, Dr. Lionel Canioni and Dr. Laurent Sarger, and my thesis reviewers, Dr. Craig Siders and Dr. Francois Salin for their constructive remarks on my dissertation work and for sharing their expertise and knowledge in optics.

I am also grateful to Larissa Glebova, Irina Popkova, Inna Ciapurina, and Karima Chamma for glass sample preparation, Vadim Smirnov, Eugeniu Rotari, Ion Cohanoschi, and Vasile Rotar for recording of the best holograms in the world for me to use in my research, Julien Lumeau for absorption measurements, and Igor Ciapurin, Nikolai Vorobiev, Alex Gourevitch, and Martin Delaigue for sharing their skills and knowledge with me in the lab.

Overall I wish to express my sincere appreciation to all members of the PPL/OptiGrate team, past and present.

During my Ph.D. work it was a pleasure for me to take part in a research exchange with the University of Bordeaux 1, France, which has later developed into a joint-degree program due to outstanding efforts and long-term vision of Laurent Sarger. I acknowledge the National Science Foundation's financial support through IMI-NFG. I want to thank Lionel Canioni for hosting me in his research group, Leonid Glebov for letting me leave UCF for this time period, Leo Siiman for laying a trail to the beautiful city of Bordeaux for me, and Arnaud Royon for helping me with the French language and the French bureaucracy.

I would like to thank CREOL faculty and staff for providing a great environment for learning and professional growth. I also want to thank Joana Lincoln for editing some parts of this manuscript.

Finally, I want to thank all the friends that I met during my years in Orlando, you know who you are. Thank you for being by my side in rough times and happy times. It does not matter whether we just played pool, dominos, or soccer yesterday or haven't spoken in years – you are in my heart forever! You all have influenced my life and if it wasn't for every one of you, I would not be who I am today.

TABLE OF CONTENTS

LIST OF FIGURES

LIST OF TABLES

CHAPTER ONE: INTRODUCTION

Historical Review of High Power Laser Development

Shortly after the first laser was demonstrated by Theodore Maiman in 1960 [24] and its ability to generate intense beams of light with small divergence was realized, increasing output power and beam brightness of these devices has become a top priority. Theodore Maiman characterized the first laser as having a power of one "Gillette"; as it could burn through one Gillette razor blade. One could say that laser-machining application was demonstrated with the very first laser. This laser produced an irregular pulse-train with pulse duration on the order of a millisecond and peak power on the order of a kilowatt. Peak power of pulsed lasers was rapidly scaled during the 1960s using Q-switching, sometimes known as giant pulse formation, and mode-locking techniques. Q-switching was first demonstrated in 1962 [25]. The 120-ns pulses observed in this experiment had peak power of 600 kW. Mode-locking was first observed in 1963 in ruby [26] and He-Ne lasers [27]. The theoretical description of active mode-locking was developed [28,29] and demonstrated for HeNe lasers [30]. Passive mode-locking, made possible by saturable absorption of dyes, was initially demonstrated in ruby [31] and dye lasers [32,33]. Typical Q-switched pulses have duration on the order of a few nanoseconds, while mode-locking can generate pulses from tens of picoseconds to tens of femtoseconds and shorter, limited by the gain bandwidth of active medium. It was immediately realized that Q-switched and mode-locked pulses can be amplified externally. In 1968, single pulses with 10-15 picosecond duration

selected from the train of mode-locked pulses generated by a Q-switched Nd-glass laser were amplified externally with two Nd-glass rods, resulting in 30 GW peak power [34]. For the next 20 or so years, advancement was based on building large amplifier chains. A Nova laser built by Lawrence Livermore National Laboratory consisted of 10 beam lines, with aperture of Nd-glass amplifiers as large as 46 cm to prevent damage and control nonlinear effects [35]. Actively Q-switched and Q-switched mode-locked lasers were used to inject the amplifier chains, available pulse duration ranged from 10 picoseconds to 100 nanoseconds. By 1990, the Nova laser was capable of delivering 5 TW peak power per beam-line with pulse duration of a few nanoseconds [36], but amplification of shorter pulses was limited by non-linear effects. Nova was built for inertial confinement fusion experiments with the intention of "igniting" a chain reaction of nuclear fusion that powers the sun. Although Nova failed in this goal, the problem was identified as related to magnetohydrodynamic instability, and construction of Nova's successor, National Ignition Facility, subsequently started in the late 1990s. The system is scheduled to be completed in 2009 and first fusion ignition tests are planned for 2010. Meanwhile, the introduction of the chirped pulse amplification (CPA) technique [37] allowed amplification of picosecond and femtosecond pulses to terrawatt power level in a table-top system [38]. Before the Nova laser was disassembled, a CPA laser system was constructed in one of Nova’s arms. This laser was capable of delivering 1.25 petawatts of power in a 440-femtosecond pulse, which is the highest power achieved up to date. This power is still below the theoretical limit imposed by saturation fluence and gain bandwidth of common amplifying materials [39]. In principle, exawatt pulses are achievable with large-aperture Nd-glass systems. These CPA systems will be limited by the technology required to stretch and compress such pulses.

The history of the development of high-power continuous-wave (CW) laser sources is significantly different. The carbon dioxide (CO_2) laser was one of the earliest gas lasers to be developed [40], and is still one of the most widely used. 60 kW of multimode power and 30 kW of single-mode continuous power from a gasdynamic laser operating on a mixture of CO_2, N_2 and H_2O was reported as early as 1970 [41] and today, almost 40 years later, industrial CO_2 lasers with 30 kW power are the highest-power continuous wave lasers commercially available. Multiple laboratory units with up to 150 kW power have been built [42]. A CO_2 laser installed at Laser Hardened Materials Evaluation Laboratory (LHMEL) producing 150 kW of CW power is considered by many as the highest power laser currently in operation, although a chemical deuterium fluoride laser developed by TRW for the US Navy has achieved 1 megawatt of power [43] for a short duration of 70 seconds. An airborne chemical oxygen iodine laser (COIL) is being developed by US Air Force with a goal of achieving megawatt-level power, but it is unclear at this time whether this goal will be achieved. Inherent problems associated with CO_2 and chemical lasers, such as large size and limited mobility, have motivated a search for alternative sources of high-power laser radiation. Recent advances in solid-state, fiber, and diode laser technologies, and various beam combination techniques resulted in a rapid increase of output power available from these devices. Laser systems combining multiple diode-pumped solid-state and fiber lasers are expected to replace CO_2 and chemical lasers in the vast majority of high-power laser applications within the next decade. In the next sub-section, we briefly review the current state of these technologies.

High-power Solid-state Laser Technology

Diode Lasers

Since the first demonstration of coherent light emission from a semiconductor diode in 1962 [44], various diode lasers have been developed by a large number of research groups. Diode lasers are the most common type of lasers with over 825 million devices sold in 2007 [45], roughly 5000 times the number of other types of lasers [46], generating more than half of the total commercial laser revenue. Laser diodes are used in a wide variety of applications: telecommunications, measuring instruments, rangefinders, barcode readers, laser pointers, scanners, printers, CD and DVD players, laser absorption spectrometry and many more. High-power laser diodes are used for pumping other lasers, most commonly fiber and diode pumped solid state lasers (DPSSL). High-brightness diode laser systems have been used for industrial applications such as heat treatment, stainless steel marking, welding, and cutting sheets of aluminum and steel of several mm thicknesses [47]. The main challenges associated with high-power diode lasers are their reliability and failure issues. The physics of diode laser failure is still in the process of being determined and research on this subject remains active. Extension of the lifetime of laser diodes is critical to their continued adaptation to a wide variety of applications. An inverse relationship between driving current (and output power) and MTBF (mean time between failures) for any given diode laser [48] makes it difficult to compare results of different researchers since the latter is rarely reported. What is clear is that both the output power and the reliability of laser diodes are steadily increasing. There are two competing approaches to designing high-power diode laser systems suitable for pumping other lasers or other applications,

both involving some sort of beam combining. The first approach is to use single emitters (laser diodes) mounted on separate heat sinks, while the second approach is to use laser bars (one-dimensional array of broad-area emitters located on the same semiconductor chip) and stacks of bars. In both cases, beam combining (transformation) is used to collect output beams from multiple emitters into a single spot, for example to couple into a multi-mode fiber. While production of high-power stacks is cheaper than manufacturing multiple single emitters, thermal management is more difficult, influencing reliability. Moreover, failure of individual emitters on a stack requires the replacement of the whole stack, while failed single-emitter diode lasers can be easily identified and replaced. While it is currently unclear which approach will eventually prevail, both technologies are being simultaneously developed. Single emitters with power around 20 W and 50-70% power efficiency have been reported up to date [48,49]. Reliability tests obtained for devices with output power 1 order of magnitude lower show MTBF of > 1,000,000 hours (> 100 years) [48]. Single emitters with output power up to 8 W are commercially available [50]. Several diode laser bars with output power exceeding 1 kW have been reported [51,52,53].

Conventional high-power diode laser systems are limited for many applications due to poor beam quality. They have been extensively used to pump other lasers, particularly solid state and fiber lasers capable of producing high-quality beams at the expense of reduced output power and overall system efficiency. DPSSL and fiber lasers are essentially brightness converters for diode laser systems. While this approach has proved very useful and high efficiency of such conversion has been achieved, direct-diode laser systems would make for more efficient and compact laser systems if higher brightness could be achieved without using intermediate lasers. Techniques of transverse mode selection [54,55] and spectral narrowing of laser diodes

[56,57,58] and laser diode bars [59,60] together with an efficient beam combining technique enable a new generation of compact high-power laser systems. This high-efficiency direct-diode system would produce a 10 kW high brightness laser beam with near-diffraction-limited divergence, with scalability to 100 kW [61]. We will discuss experimental results of spectral beam combining of diode lasers achieved by other groups in more detail in a section on spectral beam combining techniques. Also, much of the work performed within the scope of this thesis is related to design and experimental demonstration of beam combiners suitable for such systems.

Diode-pumped Solid-state Lasers

As mentioned in the previous sub-section, unless transverse mode selection or spectral narrowing techniques are implemented, most diode lasers produce spectrally-broad beams with high divergence. Such characteristics of output beams limit their use for a wide range of applications that require narrow-line or high-brightness laser radiation. However, by use of an intermediate laser medium, these characteristics can be improved at the expense of overall efficiency. DPSSLs are based on a solid gain medium pumped by diode lasers [62, 63, 64]. Compared to other types of pumping, like flash-lamp, advantages of diode-pumping include: good spectral overlap between diode emission bandwidth and laser transitions and good overlap of laser mode and pump region, both leading to improved pumping efficiency; compactness; long lifetime; low intensity noise. High electrical-to-optical efficiency of laser diodes in combination with more efficient pumping leads to high overall wall-plug efficiency of DPSSL, smaller power supplies, and lower cooling requirements, compared to lamp-pumped lasers. Along with the development of inexpensive high-power diode lasers, DPSSLs have replaced

other high-power lasers in many applications. The highest output powers from solid-state lasers are now usually achieved with diode pumping. Traditional solid-state lasers use laser medium in a shape of cylindrical rods (Fig. 1.1).

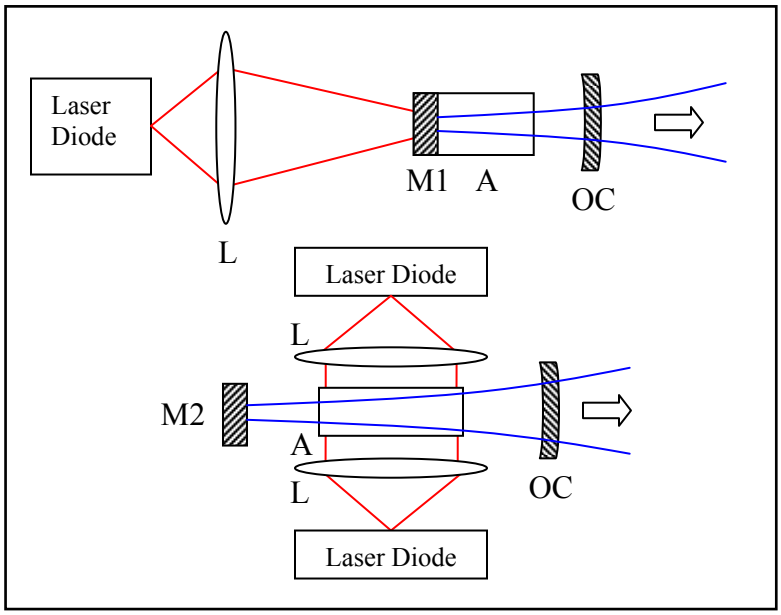

Figure 1.1. Basic schematics of longitudinally (top) and transversely pumped rod-type DPSSLs. A – rod-type active medium, L – pumping optics, M1 – end mirror with high-reflectivity for laser wavelength and high transmission for pump wavelength, M2 – end mirror with high reflectivity for laser wavelength, OC – output coupler, a partially transmitting mirror.

The main factor limiting the maximum power that can be obtained from all solid-state lasers, particularly rod-based, is heat accumulation inside the volume of the rod. The heat has to be conducted to the surface of the rod, where it can be efficiently removed by air convection or liquid cooling techniques. This causes a transverse temperature gradient in the gain medium. As a result, a thermal lens is formed inside the gain medium [65, 66, 67, 68], mainly through the change in refractive index due to the thermo-optic effect, quantified by the thermo-optic coefficient of the gain medium, dn/dT. When gain medium without birefringence is used in a laser cavity with a polarizing element (for example Brewster-cut gain medium), mechanical stresses induced by the temperature gradient can also result in induced birefringence and loss of

power due to depolarization [69, 70]. Further increase of power leads to output beam quality degradation and can result in stress fracture of the gain medium.

For most laser materials more efficient heat removal can be achieved when the gain medium is cooled to cryogenic temperatures by liquid nitrogen (77 K) or liquid helium (4 K). Interestingly, one of the very first lasers built was a cryogenic one [71], although the reasons for low temperature were other than heat removal. A number of thermal effects limiting the high-power operation of a variety of gain materials can be mitigated by cryogenic cooling [72]. Most importantly, thermal conductivity of gain materials is strongly increased, for example by a factor of 7 for YAG [73] and by a factor of 30 for Ti:Al_2O_3 [74] as the temperature is decreased from 300 to 77 K. The thermo-optic coefficient dn/dT and coefficient of thermal expansion are reduced, lowering thermal lensing and preventing stress fracture. Finally, emission and absorption cross sections of rare-earth ions are increased [73,75] and thermal population of the lower laser level is decreased [76], resulting in lower lasing threshold and higher slope efficiency. A combination of these effects results in strong improvement of laser efficiency, allowing much higher power to be generated from cryogenically-cooled rod-based lasers, compared to room-temperature operation. Using known values for the available sizes of crystals and the ratio of inversion power to heat power for diode-pumped Nd:YAG and Yb:YAG, it was theoretically shown that average power levels of >60 kW can be achievable from a single crystalline rod [73]. However, even with cryogenic cooling, operation of rod-based lasers above 1 kW leads to severe beam distortion. Near-diffraction-limited beam quality is possible only up to several hundred Watts. Up to date, good beam quality (M^2 = 1.4) from a cryogenically cooled Yb:YAG laser has been achieved up to output power of 455 W [76].

Besides operation at cryogenic temperatures, modification of geometry of gain medium that facilitates efficient heat removal can be used to reach higher output powers with acceptable beam quality. One of such geometries, that became popular in the last decade of the 20-th century, has earned enough recognition to be separated into a special type of solid-state lasers. Thin-disk (or active mirror) lasers utilize gain medium with thickness that is much smaller than beam diameter. One face of the gain medium is coated with a dielectric mirror that reflects both the laser beam and the pump radiation. Cooling of the thin-disk crystal is performed from the same side, thus extracting the heat in a longitudinal direction, as opposed to the transverse direction used in rod-type lasers (Fig. 1.2).

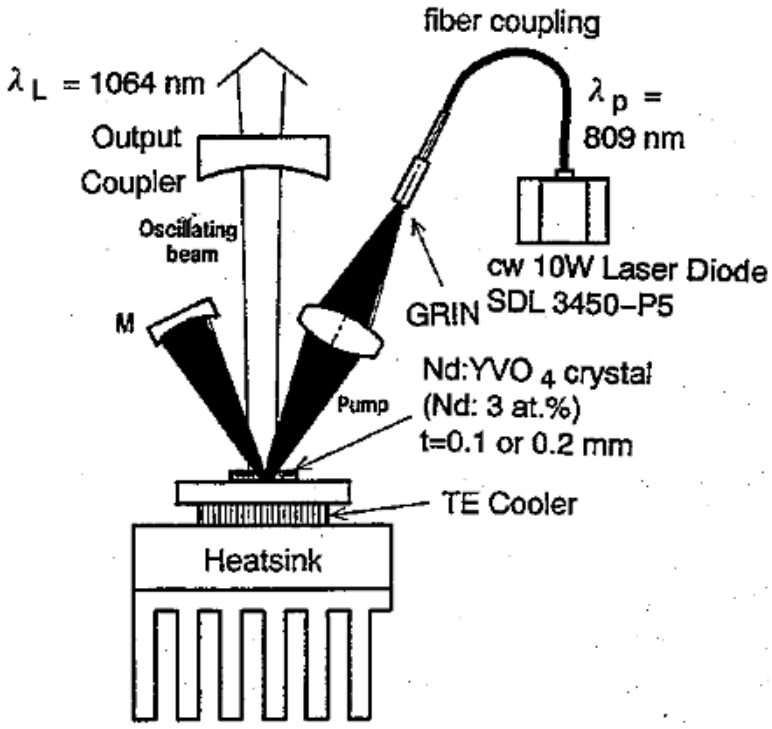

Figure 1.2. A single-thin-disk laser, from [77].

Using diode pumping, wall-plug efficiency of thin-disk lasers is usually about 25%. Efficient heat removal allows for room temperature, without significant temperature rise and

consequent thermal effects. Thin-disk lasers can be scaled by increasing the laser beam diameter. Due to the lateral geometry of heat removal, such scaling does not lead to significant increase of thermal effects. With of hundreds of Watts achieved in a near-diffraction-limited beam from single disks [78,79,80], diffraction-limited beam quality at a power level of a few kW appears to be feasible from a single disk. Up to 5 kW has been achieved from a single in a highly multi-mode operation and scaling laws for this laser design show that the power limit for CW operation is beyond 40 kW for a single disk [81].

An alternative way to scale the output power is the use of several disks in one resonator. Fig. 1.3 shows the design of a multi-mode laser where four disks are coupled together in one resonator. Output power up to 10 kW has been demonstrated in this arrangement, used by TRUMPF Laser to offer commercially-available 8-kW lasers with $M^2 \sim 24$ (Fig. 1.4).

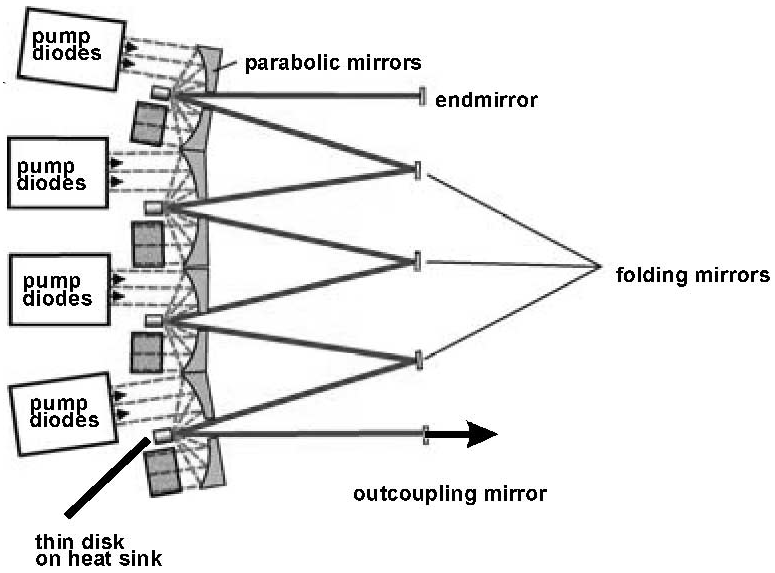

Figure 1.3. Design of the 8-kW thin-disk laser using four disks (TRUMPF Laser), from [81].

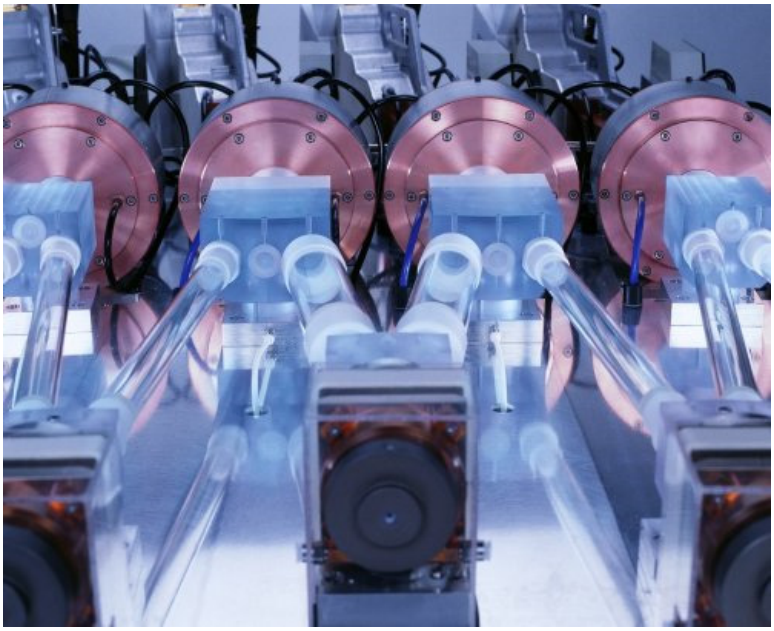

Figure 1.4. Optics layout of a high-powered disk laser (TRUMPF Laser), from [82].

Fiber Lasers and Amplifiers

Fiber lasers are solid-state lasers that use optical fibers as gain medium. Fiber amplifiers are optical amplifiers based on optical fibers. In most cases, the gain medium of fiber lasers and amplifiers is an optical fiber doped with rare-earth ions such as such as erbium, ytterbium, neodymium, praseodymium, and thulium. Selection of the doping material determines spectral and other properties of a fiber laser. The underlying idea behind fiber lasers, namely utilization of wave-guiding properties of optical fibers for mode selection was suggested as early as 1961 [83]. However, due to technological limitations of fiber fabrication and lack of high-efficiency pumping sources, little development on fiber lasers has been reported until late 1980s to early 1990s. Together with development of high-power high-brightness laser diodes and advancements in telecommunications industry in the 1990s, fiber lasers and amplifiers have gained

considerable popularity. Today, fiber lasers and amplifiers are almost exclusively pumped with diode lasers, due to the availability of high-power diodes at a variety of wavelengths that correspond to absorption bands of the different doping ions.

With a variety of fiber laser and amplifier configurations developed and the constantly improving output power and efficiency, it is not a big exaggeration to call the beginning of the 21-st century "the renaissance of fiber lasers" [84]. Fiber lasers are explosively pushing traditional lasers out of the market in a wide variety of applications. Tens of scientific conferences around the world are held and thousands of scientific papers are published annually on the subject of fiber lasers. A number of excellent reviews and books has been written on the topic, [85, 86, 87, 88] to name a few. It would be impossible to cover even a small fraction of the variety of fiber lasers with unique properties that have been developed. Instead, just a brief outline of the most prominent designs and characteristics will be discussed in this section with the emphasis on high-power operation and scalability issues. Also, mostly Yb-doped fiber lasers and amplifiers are considered in this work for two reasons: the highest power operation is usually achieved with these lasers compared to other rare-earth ions, and most high-power beam combining experiments, including the ones described in this thesis, use Yb-doped fiber lasers.

A resonator cavity of fiber lasers can be formed by ordinary dielectric mirrors located at each end of the active fiber, much like for other types of lasers. However, this approach is not the most practical or robust. Fresnel reflection from a polished tip of the fiber can often be used as an output coupler, or dielectric coatings can be deposited onto the ends of the fiber. However, this approach does not allow for control of spectral properties of laser emission. Commercial products typically use fiber Bragg gratings recorded directly in the active fiber, or spliced to fiber ends. One of the most widely used configurations of a fiber laser is shown in Fig. 1.5. Even

single-frequency operation with very narrow linewidth of a few kHz can be achieved in short fiber lasers with narrow-band fiber Bragg gratings [89].

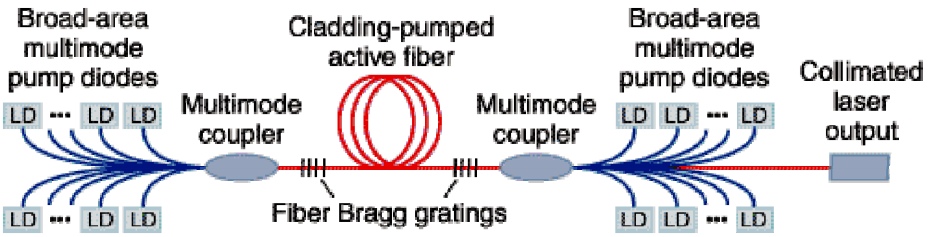

Figure 1.5. Design of a fiber laser used by IPG Photonics, from [90].

Fiber lasers have gained much popularity due to a number of advantages over other types of lasers, including free-space solid-state lasers. All-fiber design allows for much more stable operation and robustness, avoiding the influence of the environment and requiring virtually no alignment. Glass host of the active fiber results in broad gain bandwidth, which permits wide spectral tuning and can support ultrashort pulse generation. Also, broad absorption regions allow for efficient pumping at different wavelengths. Very high optical-to-optical and wall-plug efficiency is a special characteristic of fiber lasers. Ytterbium-doped fiber laser, which have a quantum defect of less than 10%, can provide optical-to-optical efficiencies well above 80%. High surface-to-volume ratio in optical fibers facilitates heat dissipation, while wave-guiding properties of fiber help to avoid thermo-optical problems, even under significant heating. Diffraction-limited output beam quality is usually obtained from single-mode fibers and from some slightly multi-mode fibers under certain conditions.

Most high-power fiber lasers use a master oscillator power amplifier (MOPA) configuration, where a lower power laser is used to seed a cladding-pumped high-power amplifier. This concept allows scaling of output power, while preserving other optical characteristics of the low-power seed laser. Fiber amplifiers are usually based on double-clad

fibers. An inner cladding that is much larger in diameter and has a higher numeric aperture than the signal core is used for pumping. Double-clad fibers with single-mode core are capable of producing near-diffraction-limited output beams, which means that the brightness of the output beam is orders of magnitude higher than that of pump light. Therefore, similarly to other solid-state lasers, fiber lasers are essentially brightness converters for pumping radiation.

The limitations in scaling a single fiber laser or fiber MOPA system include thermal self-focusing, non-linear effects [91,92], facet and volume damage, and/or the availability of high brightness pump diodes. Large-mode-area (LMA) step-index fibers [93] and photonic crystal fibers (PCF) [88,94] designs allow to mitigate these effects to a certain degree [95]. Fiber lasers based on PCF and LMA fiber have been demonstrated with output power of 1.53 kW [96] and 1.36 kW [97] respectively.

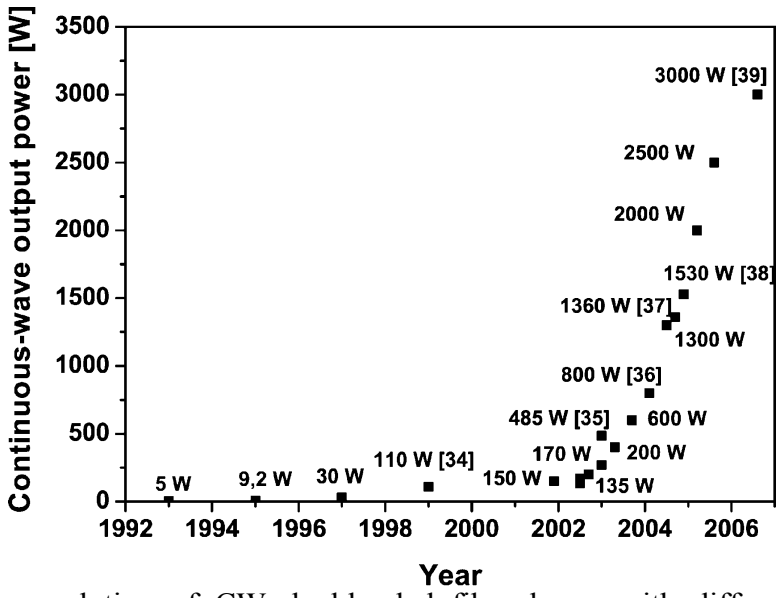

Figure 1.6. Power evolution of CW double-clad fiber lasers with diffraction-limited beam quality, from [98].

Fig. 1.6 shows the rapid progress in output power available from CW fiber lasers with near-diffraction-limited beam divergence over the recent years [98]. Similar rate of growth at somewhat lower power levels was demonstrated by fiber lasers with narrow emission linewidth.

Up to date, the highest power demonstrated from a single fiber laser with near-diffraction-limited beam is about 0.5 kW with narrow linewidth [91,99] and 6 kW with a broad bandwidth of about 10 nm [100]. However, the rapid progress in this field is expected to slow down, as limitations to power-scaling of single fiber lasers are more clearly shown and better understood. Rigorous analysis shows that interaction of thermal effects, finite pump brightness, limited doping concentrations, non-linear effects and damage limit the scalability of a single aperture fiber laser. The hard limits on the output power of broad-band fiber lasers at around 36 kW and narrow-band fiber lasers at around 2 kW are identified [101]. While waveguide designs which suppress Raman and Brillioun effects may increase these limits somewhat, the upper limit to the scalability of the core diameter somewhere in the area of 50 μm diameter limits the output power of a simple compact single-aperture fiber laser with $M^2 = 1$ to around 10 kW.

This analysis suggests that output power of such lasers can only be increased by a factor of 3-5 from the current records. Beyond that, further power-scaling of fiber lasers can only be performed by combining beams from multiple such lasers externally. The following sub-section describes a variety of combining techniques that can be used for further power scaling of fiber lasers, with an emphasis on those that capable of preserving near-diffraction-limited divergence of beams. In contrast to these methods, 20 kW fiber laser systems available from IPG Photonics use side-to-side combining of ten 2-kW broad-band fiber lasers, which results in deterioration of beam quality to $M^2 = 6$ [102].

Beam Combining Techniques

Introduction to Beam Combining

With fundamental limitations to power scaling of single-emitter lasers, described in the previous sub-sections, further power scaling can be achieved by combining the output of multiple lasers into a single beam. Many methods of beam combining have been developed over the years, from straight-forward aperture-tiling (side-by-side) and polarization combining to fiber-based combining, spectral beam combining and sophisticated coherent beam combining. A good review of strengths and advantages of the different methods is made in [103]. Schematics of the most popular classes of beam combining are shown in Fig. 1.7.

Side-by-side beam combining is the simplest form of incoherent beam combining where no effort is made to control the phase or frequency of individual elements. The combined power and the size of the source aperture are both proportional to the number of elements, while the far-field divergence is that of a single element. Therefore, the radiance is the same as that of a single element, and the overall brightness is decreased in side-by-side combining. Conventional diode laser arrays fall into this class of beam combining. Side-by-side combining is not considered in this review, since it does not allow power scaling with near-diffraction-limited divergence of the combined beam.

Three classes of beam combining that can result in increased brightness and are capable of producing near-diffraction-limited output beams have been identified: coherent beam combining, spectral beam combining, and polarization beam combining. The latter, however cannot be considered as a method of power scaling in a strict sense, because it is not repeatable.

In this method, two linearly-polarized beams are combined using a polarization-selective optical element. Beam quality can be preserved and power and brightness can be doubled. It requires polarized input beams and leads to an unpolarized output beam, so the maximum number of elements that can be combined is two. This method is often used to combine two pump beams with different polarization [104, 105]. It can be utilized in conjunction with other methods of beam combining, like spectral beam combining, as the final combining step.

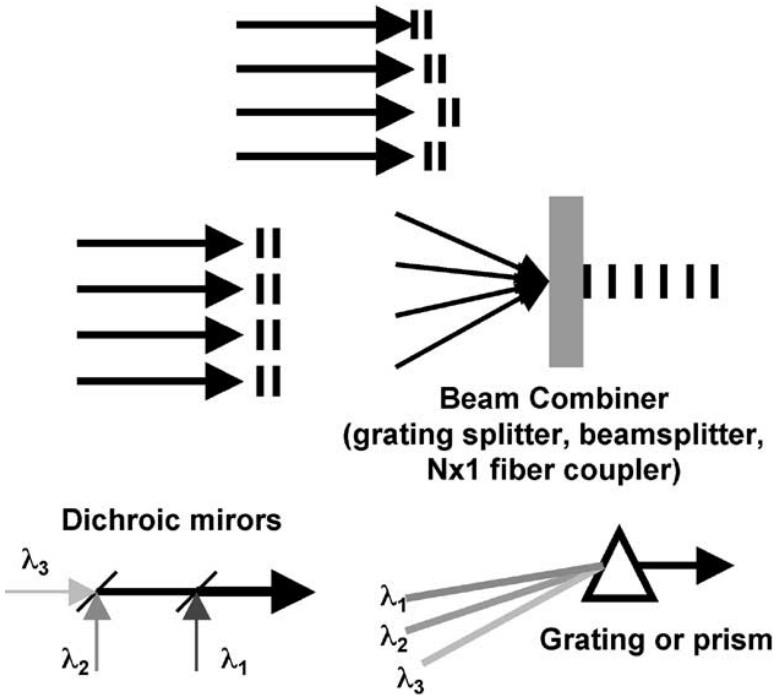

Figure 1.7. Notional schematics of the broad classes of beam combining. Top – side-by-side beam combining; middle – coherent beam combining with tiled apertures on the left and with filled-aperture on the right; bottom – spectral beam combining in serial configuration on the left and parallel configuration on the right, from [103].

Coherent Beam Combining

Coherent beam combining can be realized for mutually coherent beams. Using this method, relative phases of beams from an array of elements that operate with the same spectrum are controlled such that constructive interference between the output beams facilitates formation of a single beam with improved brightness. Historically, most of the effort to obtain good beam quality through laser beam combining has attempted to use this class of techniques. This is the analog of phased-array transmitters in the radio-frequency (RF) and microwave portions of the electromagnetic spectrum, but in the optical domain coherent beam combining has proven to be difficult because of the shortness of an optical wavelength. The phases of the array elements need to be controlled to a small fraction of a wavelength; for the optical portion of the spectrum, the wavelength is on the order of 1 μm. Until very recently, coherent beam combining has been demonstrated for small arrays, but identifying robust simple phased array approaches for combining large arrays (tens to hundreds of elements) with nearly ideal beam quality has been elusive [103]. Most common methods of coherent beam combining are: common resonator, evanescent-wave or leaky-wave coupling, self-organizing, active feedback, and nonlinear optical (Fig. 1.8). Excellent reviews of coherent beam combining have been published [106, 107, 108, 109, 110].

When high-power coherent beam combining is considered, time varying thermal loads and other disturbances influence the optical paths of each of the fibers. Active feedback is required in order to provide for stable coherent addition. To date electronic phase locking methods [111, 112, 113, 114, 115] have exceeded the performance of the self-organized and other coherent combining approaches in beam quality, in efficiency of coupling power to the central lobe and in setting the record for phase locked fiber laser power [116].

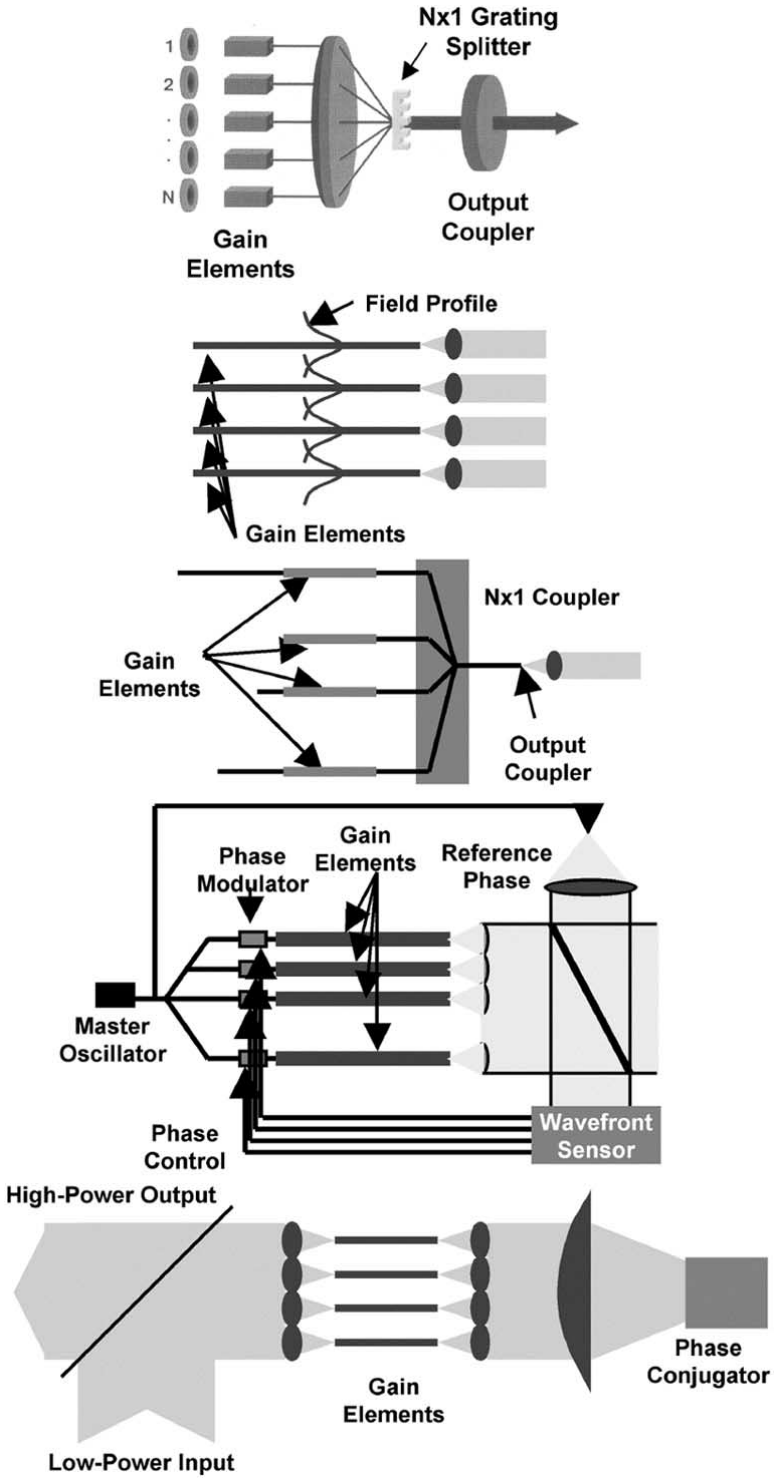

Figure 1.8. Schematics of coherent beam combining approaches. From the top: common resonator, evanescent or leaky wave, self-organizing or supermode, active feedback, and nonlinear optical (phase conjugation), from [103].

The highest fiber laser power that is coherently combined to date is 725 W [115]. Phase-locking of five 145-W fiber amplifiers is achieved with rms phase error of λ/60 by using a Self-Synchronous Locking of Optical Coherence by Single-detector Electronic-frequency Tagging (LOCSET) technique (Fig. 1.9). A distinguishing feature of this technique is that the array elements are phase modulated at unique RF frequencies. The phase error signal for an individual phase modulated element originates from the RF beat note generated by the interference between the overlapping fields of the individual array element with the fields from the other array elements. With this technique phase-locking of individual elements can be performed without a requirement for a reference beam. This result is closely followed by a 2 × 2 passively phase-locked fiber array with 710 combined power [117]. Similar results were achieved by another group by using a frequency-shifted reference beam that is interferometrically combined with a portion of each channel's output signal [118]. Maximum power of 470 W from a 2 × 2 tiled fiber laser array.

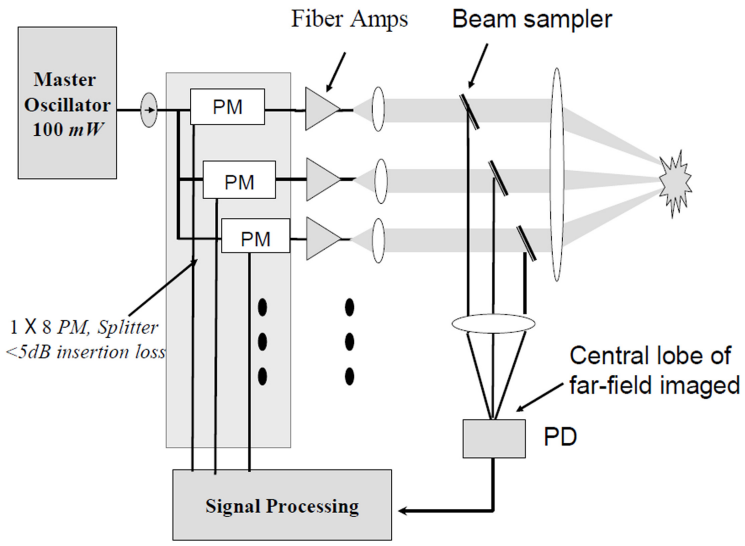

Figure 1.9. LOCSET beam combining block diagram. PM represents phase modulators and PD represents the photo-detector, from [116].

All of these results suffer from an important drawback, related to the properties of tiled aperture spectral beam combining architecture. When the laser elements are single-mode fiber lasers, which generate near-Gaussian intensity profiles, the loss in beam quality of a close-packed tiled array can be substantial. This is illustrated in Fig. 1.10, in which only 63% of the 470W from a 2 × 2 tiled fiber laser array is contained within the far-field central lobe [118]. The fraction of power in the far-field side-lobes can be reduced only by reducing the spacing between beamlets, which unavoidably reduces the overall combination efficiency owing to near-field clipping of the Gaussian beamlet wings. To avoid this problem, the authors suggested using a diffractive optical element (DOE) as a beam combiner for an actively phase-locked array of fiber lasers.

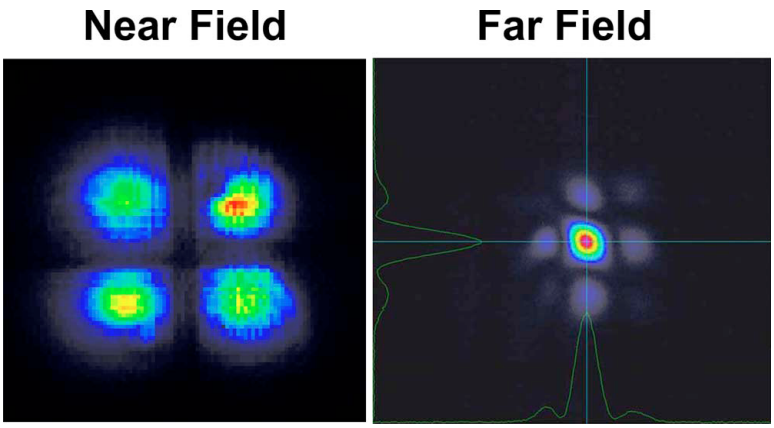

Figure 1.10. Near-field and far-field intensity distributions measured with a close-packed, phase-locked array of four ~ 100W fiber beamlets, from [118].

Use of a DOE allows coherent combining in a filled-aperture geometry, where beams from all elements are overlapped at the DOE and emerge collinearly (Fig. 1.11), which eliminates the far-field side-lobes and the accompanying loss of beam quality. Using this technique, coherent combination of five fiber lasers with 91% efficiency and M^2 = 1.04 was demonstrated at low power ~ 0.1 W. However, calculations and power handling measurements suggest that this approach can be scaled to both high channel counts and high powers [119].

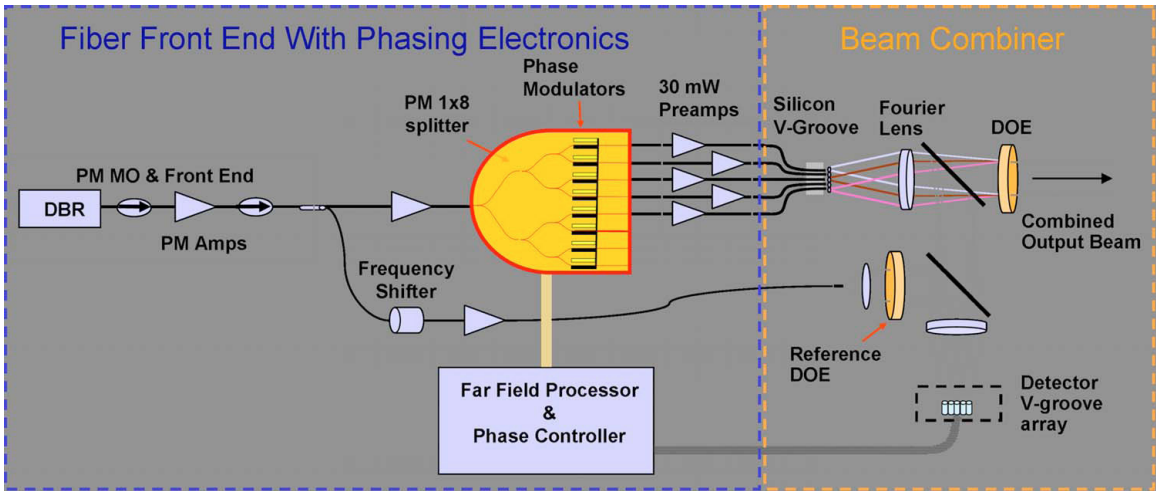

Figure 1.11. System architecture for DOE-based coherent beam combining, from [119].

Spectral Beam Combining

Spectral beam combining (SBC, or wavelength beam combining) is an incoherent combining technique that does not require phase control of sources, allowing for a stable and robust system. Using this method, beams from an array of lasers with each element operated at a different central wavelength can be combined into a single near-diffraction-limited beam using dispersive optical elements. Such arrays are also inherently power scalable since the laser elements are uncoupled. Using spectral beam combining, the energy brightness of the combined beam is increased compared to individual sources, while spectral brightness is decreased, since combined beam spectrum consists of multiple peaks corresponding to individual sources.

SBC can be implemented with either spectrally-dispersive or spectrally-selective optical elements. The former include prisms, transmitting and reflecting surface diffraction gratings, and transmitting volume Bragg gratings (when used to combine beams with spectral separation smaller than spectral selectivity). Spectrally-selective optical elements that have been used for

SBC include dichroic and step-edge interference filters, reflecting volume Bragg gratings, and transmitting volume Bragg gratings (when used to combine beams with spectral separation equal to or larger than spectral selectivity). Spectral beam combining using these two types of optical elements is based on fundamentally different properties. In the case of spectrally-dispersive elements, dependence of the angle of deviation on the wavelength of incident beam is utilized for combining, whereas combining with spectrally-selective elements is based on the spectral dependence of transmission and reflection of these elements. This difference in properties of the two types leads to significant differences in performance when sources with relatively large bandwidths are combined. For SBC with spectrally-selective elements increased bandwidth can lead to decreased efficiency of combining, however it does not influence the beam quality of the combined beam. This is usually the opposite for SBC with spectrally-dispersive elements: combining efficiency is not affected because of wide spectral selectivity of these elements, however beam quality can be significantly deteriorated due to additional divergence imposed by angular dispersion of beam combiner.

An early implementation of spectral beam combining used dichroic interference filters to combine six diode lasers operating at different wavelengths [120]. The output of an individual diode was transmitted through an interference filter that reflected all other wavelengths. Recently, a similar technique was used to combine three Yb-doped fiber lasers with central wavelengths offset by about 3 nm with > 90% efficiency yielding 52 W combined power [121]. It is important to note that lasers with wide bandwidth of 1-2 nm are combined by step-edge interference filters in that work. It would be theoretically impossible to combine such sources into a single beam with acceptable beam quality using spectrally-dispersive combining elements.

Early efforts of spectrally combining diode lasers by means of diffraction gratings [122, 123] had limited success because wavelength instability of the sources degraded the output beam quality [103]. In the late 1990s, an SBC setup based on a surface diffraction grating with spectral control of sources by optical feedback was proposed (Fig. 1.12) and used to demonstrate spectral beam combining of 2 fiber lasers [124] and outputs of an 11-element array of broad-stripe laser diodes [125] at relatively low power levels. This configuration was later theoretically described and analyzed [126]. To date, the highest CW power achieved in this configuration for diode lasers is 30 W from a 100-element array with total spectral width ~ 15 nm and $M^2 \sim 2$ [127]. For the sake of a later discussion, we will note that spectral power density is 2 W/nm for this combiner.

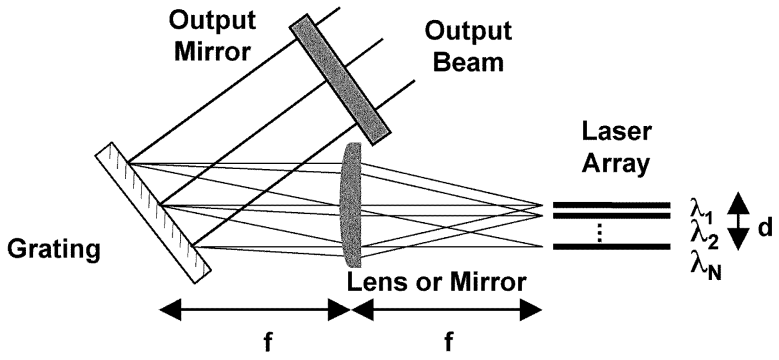

Figure 1.12. SBC with optical feedback for spectral control of elements, from [103].

The setup of Fig. 1.12 has been scaled to 100 W of combined power with $M^2 = 2.7$ by combining three fiber lasers, separated by 6.5 nm [128]. The corresponding spectral power density is about 5 W/nm. The scaling potential of this setup suffers from a possible cross talk between different fibers lasers. An additional problem is that, especially at higher power levels, a trade-off has to be made between a feedback sufficient to suppress self-lasing of the fiber and sufficient output coupling for good laser performance [129]. A modified setup, suitable for combining fiber lasers in a MOPA configuration was proposed [130]. However, a high-precision

alignment of fibers is necessary to guarantee high performance of all fiber lasers. The maximum output power reported with such setup to date is 73 W from three fiber MOPA lasers [131] with corresponding spectral power density of about 20 W/nm.

Much higher power levels have been reached in a configuration that uses a surface-grating to combine fiber MOPA lasers without control of emission wavelengths by optical feedback (Fig. 1.13). Although alignment of such system is more complicated, stable operation at higher power can be achieved. 522 W of average power with near-diffraction-limited (M^2 ~ 1.2) beam quality of combined beam has been reported [132]. Three wavelength-tunable fiber MOPA channels with narrowband polarized near-diffraction-limited output are spectrally combined with spectral power density of combining 25-70 W/nm (channel separation 2.5 and 7.5 nm).

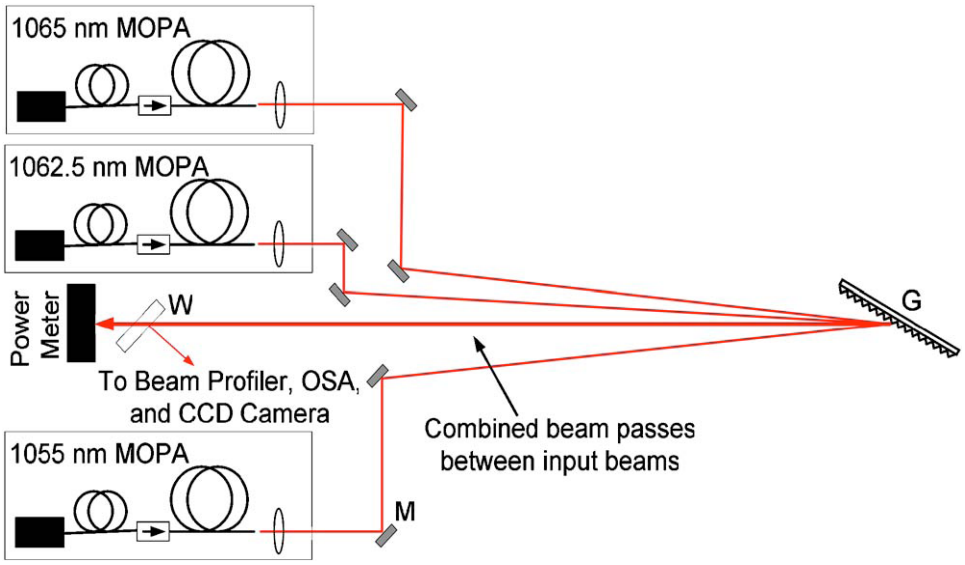

Figure 1.13. Spectral combining of fiber MOPA lasers with a reflecting diffraction grating, from [132].

Just before this thesis was submitted, another group has reported spectral beam combining in a configuration very similar to that of Fig. 1.13. In their experiment four narrow-linewidth fiber MOPA chains, delivering 500 W optical output power were spectrally combined

for total output power of 2 kW using a dielectric reflective diffraction grating [133]. Spectral separation of channels is about 5 nm and spectral power density of combining is 100 W/nm, which is the record high value for experimentally demonstrated spectral beam combining using surface diffraction gratings. Spectral width of sources is 60 pm. A less dispersive surface grating is used in this experiment, which helps to mitigate the effect of beam quality degradation due to additional divergence imposed by dispersion. A simple calculation shows that for 3 mm diameter of the beams used in the experiment, divergence of beams after the grating increases by about 10% in the plane of diffraction due to spectral width of sources. M^2 values reported are consistent with this estimation: $M^2x = 1.6$ and $M^2y = 1.4$ for a single beam diffracted by the grating and $M^2x = 2.0$ and $M^2y = 1.8$ for the combined beam. However, from the collection of data presented it is not clear which part of the beam quality degradation (for both single beams and the combined beam) can be attributed to grating non-uniformities and which part is related to thermal distortions of the grating that can be expected at these power levels. The author states that thermo-optical issues are not expected at that power level, referring to FEM-analysis published earlier [98]. However, extremely low value of grating absorption (2 ppm) is used in that analysis, hardly achievable by the modern technology. Extrapolating results of that analysis, thermal distortion of grating period that will cause noticeable deterioration of beam quality will occur at absorbed power of less than 1 W, which corresponds to grating absorption of 0.05%. It is not trivial that the grating used in this experiment has total absorption lower than this very impressive value. Since absorption of the grating is not given, it is not possible to conclude whether or not thermal distortions play a role in beam quality deterioration.

Spectral beam combining with surface diffraction gratings in a configuration of Fig. 1.13 is usually performed with spectral separation of channels about 5 nm. This is related to

dispersion properties of these combining elements. Angular dispersion of a grating with density of 1700 gr/mm is about 4 mrad/nm for wavelengths in the vicinity of 1 μm. Such grating represents roughly the highest dispersion that can be achieved. We consider the possibility of 0.2 nm spectral separation of channels, which corresponds to 0.8 mrad angular dispersion between channels. To angularly separate the beams from neighboring channels, divergence of each beam should be no more than 0.2 mrad, which corresponds to diffraction-limited divergence of a 6.5 mm beam. Fig. 1.14 shows the calculated minimum distance between the source (or a steering mirror) and the beam-combining grating, required to provide lateral shift of beams equal by twice the beam diameter.

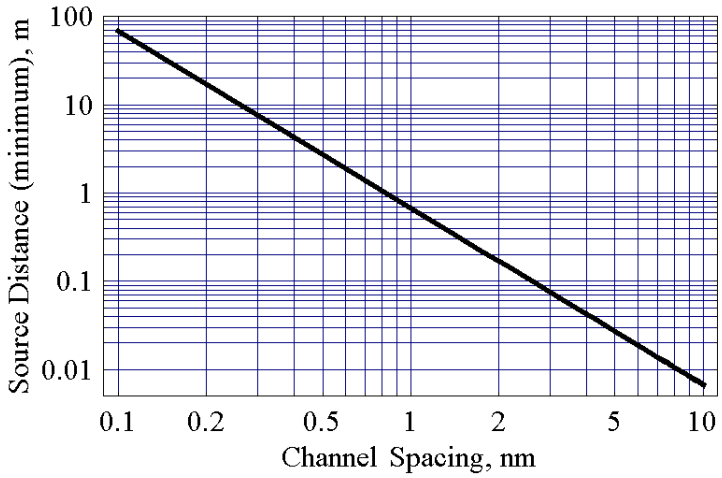

Figure 1.14. Minimum distance between the sources and the beam-combining grating, required to provide lateral shift of beams in a spectral beam combining setup of Fig. 1.13.

This very conservative estimation shows that channel spacing between 1-10 nm can be comfortably achieved in a laboratory. However, further decrease of channel spacing results in large distance required between the sources and the grating. For 0.2 nm channel spacing, this distance becomes 16 m. This results in a proportional increase of beam-combiner dimensions. Besides the overall size concerns, increasing of source to grating distances makes the system susceptible to vibrations, since the output collimators of fiber amplifiers and the combining

element can hardly be mounted on a common vibration-isolating table. Vibrations can result in relative pointing instabilities between the channels, with the result of combined beam quality deterioration.

Reflecting VBGs, described in this thesis, used at near-normal incidence are much more advantageous for high-density spectral beam combining (2 channels/nm and higher) due to wide angular acceptance and the small source-to-grating distances required. Table-top SBC systems that combine multiple beams with spectral separation down to 0.25 nm are demonstrated with high combining efficiency. The largest dimension of these 5-channel beam combiners is on the order of 1 meter. The high-power spectral beam combining setup that combines five fiber lasers with spectral separation of 0.5 nm (Section 6) demonstrates output power of 773 W. This corresponds to over 300 W/nm spectral power density of the beam combiner achieved in a compact table-top arrangement. This spectral power density is at least 3-5 times higher than the best experimental results of spectral beam combining with surface diffraction gratings. Moreover, in contrast to the surface grating based SBC, further scaling of spectral power density of the volume Bragg grating based combiner can be achieved by decreasing channel separation (demonstrated) in a very straight-forward way that does not require increase in the size of beam combiner. This and other differences between the two approaches are analyzed in the following sub-section.

Comparison of Grating-based Beam Combining Approaches

Three approaches to beam combining that can potentially be scaled to produce diffraction-limited beams with power level on the order of 10 or even 100 kW have been

identified in the previous sub-sections. These approaches are: spectral beam combining using surface diffraction gratings in a geometry of Fig. 1.13 (we will refer to it as SBC SDG), coherent beam combining using diffractive optical elements in a geometry of Fig. 1.11 (CBC DOE), and spectral beam combining using volume Bragg gratings (SBC VBG). The first approach is used by Aculight and University of Jena [129, 132, 133], the second one has been recently developed by Northrop Grumman [118, 119], and the third one has been pioneered by our group at the University of Central Florida [134] and further improved by the work presented in this thesis. In this sub-section, the strengths and weaknesses of the three approaches are analyzed.

The main requirements for the system are high brightness of the combined beam, low weight and size of the total system, high tolerance to high power laser radiation, vibrations and environmental contaminations, and manufacturability. Table 1.1 provides a comprehensive comparison of the three approaches, based on requirements for laser sources, parameters of a beam combiner, and parameters of a combined beam.

The first area of consideration concerns properties of laser sources which could be combined by these different methods. SBC with VBGs can be realized with either single stage lasers (i.e. power oscillators) or MOPAs. This property leads to several consequences. First, the spectral width of lasers for SBC with VBGs could be several orders of magnitude wider than that of other two methods. Coherent beam combining by definition requires a master oscillator emitting a beam with a long coherence length which is then split between a number of channels and combined after amplification (a MOPA configuration). To provide the coherence length needed, a single frequency master oscillator with spectral width in the Megahertz range is usually used. Spectral beam combining does not require coherence of the combined beams, and the spectral width of each beam is determined by the particular dispersive elements which are

used in the different designs. Thus, nonlinear processes which restrict the maximum power of fiber laser systems would have a significantly higher threshold for SBC with VBGs. However, it should be noted that the highest-power implementation of spectral beam combining with SDGs demonstrated by Aculight is based on a MOPA configuration with a single frequency master oscillator [132]. This is done in order to avoid additional divergence that results from dispersion of SDGs over the spectral width of the beam. This well-known effect imposes limitations on the maximum beam size that can be used for SBC with SDGs and can deteriorate beam quality of beams with appreciable spectral width [135]. While beam-quality issues are mitigated by using a single frequency master oscillator, maximum power that could be obtained from the amplifiers was limited due to onset of stimulated Brillouin scattering in the amplifier fiber. This limitation was overcome in [132] by temporally modulating the seed signal to produce a quasicontinuous-wave pulse trains (~5 ns pulse duration, 10 MHz repetition rate) that suppress stimulated Brillouin scattering by providing narrowband signals only on time scales less than the 10 ns stimulated Brillouin scattering buildup time [136]. While this solution worked for now, further power scaling of each MOPA appears to be complicated since pulsed operation will lead to non-linear self-phase-modulation in fiber amplifiers, which will increase the bandwidth of the amplified signal, which in turn will lead to deterioration of beam quality if the beams are combined with a SDG. These complications can be avoided all-together when spectrally-selective non-dispersive elements (like reflecting VBGs) are used for beam combining.

Another significant advantage of reflecting VBGs developed at UCF is insensitivity to polarization of laser radiation whereas the DOE and SDG approaches are polarization-sensitive. This means that a more robust laser design having a random polarization can be used for SBC VBG, while SBC DOE and CBC SDG approaches can be used to combined polarized laser light

only (at least when high efficiency of combining is required). In many cases use of unpolarized radiation is beneficial, since losses and beam quality deterioration due to birefringence of any optical elements preceding the combiner and the use of polarizing and polarization-maintaining components can be avoided.

Spectral beam combining with VBGs or SDGs does not require beam splitting for feedback purposes, but coherent combining with DOEs does. This means that the complex subassembly which requires fine adjustment and stability of the splitting coefficients has to be used for CBC DOE. Fourth, a MOPA architecture is sensitive to back-reflected radiation. This means that SBC SDG approach using MOPA and CBC DOE approach require optical isolators to be placed in the high power beam. It appears that an isolator for a 100 kW or even a 10 kW beam does not exist yet. Isolators are based on materials that undoubtedly will have lower tolerance to laser radiation than PTR glass (which has tolerance to high power radiation compared to that of fused silica).

As mentioned earlier, coherent combining requires a complex system of relative phase control of the channels, while it is not needed in SBC with VBGs or SDGs. Thus, spectral beam combing with VBGs provides both a significantly reduced need for associated optics as well as a relaxation of the required laser properties (wider spectrum, unpolarized beams, reduced nonlinearity, etc.) and therefore allows a more robust system design using higher power single emitters.

An important parameter of a combiner is the spectral power density. The atmosphere has two windows of transparency in the near IR region centered at 865 and 1040 nm with spectral widths of about 50 nm. Since coherent combining does not change the spectral width of the combined narrow band radiation, its total spectral width is not an issue. However, for spectral

beam combining the overall spectral width needs to be addressed. It is necessary to have a spectral power density of at least 2000 W/nm to provide a 100 kW laser beam propagating within a 50 nm window of transparency. If one can consider a 1 kW Yb-doped fiber laser with a diffraction limited divergence and a narrow spectral width (0.1 nm) that can be achieved in the near future, it would require 100 channels with 0.5 nm channel separation to provide a 100 kW combined beam. The highest spectral power density of a SDG-based spectral beam combiner reported to date is about 100 W/nm [133]. The spectral combiner developed by Aculight has spectral power density 25-70 W/nm. As discussed in the previous sub-section, further decrease of channel separation leads to a higher spatial frequency of the grating and to a significant increase in dimensions of a combiner. For comparison, a channel separation of 0.5 nm with maximum power density above 300 W/nm has already been demonstrated with VBG-based beam combiner (160 W per channel) discussed in Section 6 of this thesis. The desirable level of 2000 W/nm can be readily achieved with the same combiner for 1 kW fiber lasers.

Spectral beam combining with any grating typically uses a passive optical system and, therefore, is more robust and reliable in comparison with coherent combing. A comparison of the various components of these combiners has several aspects. First, beam combining with SDGs and DOEs requires several elements in a high power beam: beam splitters, lenses and optical isolators. The architecture of spectral beam combining with VBGs does not require the use of these elements in a high power system. Beam splitters are not needed for feedback purposes as they are in DOE systems. Optical signal reflected from a target can be amplified and affect MOPA systems used in CBC DOE and some SBC SDG approaches, which require isolators. SBC VBG combiner with power oscillators is not significantly affected by such feedback. This

means that the SBC VBG approach will not suffer from problems with thermal aberrations and birefringence of lenses, beam splitters, and optical isolators.

Comparing SDGs and VBGs, the most important difference from a practical point of view is that volume Bragg gratings have flat polished surfaces coated with a simple antireflection coating. Surface gratings with a metal coating are not considered for use at all because of their low tolerance to laser radiation. Recently developed surface gratings with dielectric coatings have a higher laser damage resistance. However all tests of this characteristic were done in laboratories with environmentally controlled conditions and not in field tests. It is clear that surfaces with complex micro-structure are difficult to clean, leading to higher maintenance and inevitable decrease of laser damage threshold over time. Even in laboratories, surface gratings used for high-power applications usually have to be protected from dust accumulation when not used. By comparison, volume Bragg gratings can be easily cleaned and used in harsh environments. For example, holographic target boards fabricated from PTR glass were successfully field-tested by the Georgia Tech Research Institute at a laser range in New Mexico in 6 kW laser beams. No excessive special care to prevent dust collection on the surface was exercised.

There is an argument that reflecting SDGs are superior relative to VBGs because there is no bulk material to absorb the radiation. However, surface absorption of optical elements with complex profiles is usually significantly higher than volume absorption of high-quality PTR glass. Surface heating of SDGs can cause beam distortion and a gradient of the grating period, which in turn will cause a variation of the diffraction angle, contributing to divergence of diffracted beams. Even very low surface absorption of a SDG on the order of 20-30 ppm (hardly achievable with modern technology, typically 2-3 orders of magnitude higher) can result in a

temperature rise of tens of K, localized in the center of the beam and on the surface of the grating, when operation in a 100-kW beam is considered (an estimation based on the modeling results presented in [98]). The thermal gradient formed by this temperature rise is sufficient to distort the grating period and cause detrimental effects to the quality of diffracted beam due to non-uniform angular dispersion value across the beam aperture (based on the same reference). With absorption level of the best currently-available SDGs, the onset of these effects is somewhere around 1 kW, slightly dependent on beam size. Small but detectable distortion of diffracted beam on the order of $\lambda/10$ is observed in one of the best state-of-the-art dielectric gratings even under relatively low 70 W of power with 1.5 kW/cm^2 peak irradiance on the grating [132].

The material used for fabrication of volume Bragg gratings at the University of Central Florida, PTR glass, currently has an absorption coefficient after UV exposure and thermal development approaching 2×10^{-4} cm^{-1} (400 ppm/cm) for wavelengths around 1 μm. It should be noted that absorption in both fused silica and PTR glass is not an intrinsic property but is determined mainly by impurities of iron and water. Absorption of undeveloped PTR glass is about 6×10^{-5} cm^{-1} (140 ppm/cm). We expect to fabricate developed PTR glass with absorption decreased by factors of two to four in the near future.

Due to beam propagation inside the volume of a VBG, temperature rise associated with absorption of high-power radiation is more evenly distributed through the volume of the grating, compared to the case of reflecting SDGs. It means that the change in grating period is more uniform. Moreover, non-uniformity of grating period does not have a significant effect on the quality of diffracted beams, as opposed to SDGs. This is related to the fact that VBGs are spectrally-selective elements, while SDGs are spectrally-dispersive. As a consequence,

temperature rise in VBGs leads to a shift of resonant wavelength, but not to deterioration of beam quality. It was shown in [3, 6] and in this thesis (Sections 5, 6) that for temperature rise on the order of 30 degrees K due to absorption of laser radiation, resonant wavelength of a VBG is shifted by about 0.3 nm, as a result of period expansion. However, the most important properties of the grating, peak diffraction efficiency and spectral selectivity bandwidth, are virtually unchanged. No beam quality deterioration is observed for beams diffracted by such thermally-loaded grating (M^2 of diffracted beams is measured at ~ 1.15). Since the time these experiments were conducted, absorption of VBGs has been improved by about 5-8 times and is expected to improve by another 2-4 times from the current level. These results allow expecting similar behavior from gratings with improved absorption at power levels of 10-30 kW. At the present time it is difficult to say whether any significant beam degradation will or will not occur at power levels higher than 30 kW.

The effect of the resonant wavelength shift due to expansion of VBG period can be easily compensated by angular tuning (as was done in the experiment described in Section 6). However, a more elegant solution was suggested in [10, 12] and in Section 8 of this thesis. Wavelengths of individual emitters can be controlled by the beam-combining VBGs by using an external-cavity configuration with a broad-band output coupler. Wavelengths of the lasers in this configuration are forced to follow the resonant wavelength of the beam-combining VBGs. It was shown that source wavelengths are shifted by about 0.3 nm for temperature rise of beam-combining VBGs about 30 K. System efficiency and other characteristics remain unchanged during this process. It should also be noted that PTR glass is a type of glass that can be modified to produce a negative dn/dT sufficiently large to cancel the positive dL/dT of the glass. It is possible, at least in principle, to make athermal windows, lenses, volume Bragg gratings and

other optical elements which would not be affected by temperature rise associated with absorption of high-power laser radiation.

Manufacturability is also an issue in beam combining design. Low-absorption multi-layer dielectric diffraction gratings for spectral combining and low-spatial-frequency DOEs with multiple equal diffraction orders for coherent combining are one-of-a-kind experimental samples that are quite difficult and expensive to manufacture. Volume Bragg gratings for spectral beam combining are simple in design, less difficult to manufacture, lower-cost and are already in commercial production.

One of the biggest advantages of coherent beam combining is that this method provides an opportunity for both conventional and non-mechanical (i.e. electronic) beam steering. The output of spectral combiners is an incoherent multi-wavelength beam which can only be steered by conventional beam scanners.

Finally, there is a major concern about robustness of spectral combiners related to the size and length of their optical system (optical lever arm) and the corresponding tolerance to vibrations. It was shown in the previous sub-section that low angular dispersion of SDGs leads to long distances between the lasers and the dispersive element. This is not an issue for SBC with reflecting VBGs. In fact, a compact 4-channel beam combiner with 0.7 nm spectral separation of channels, 18x7x6 cm^3 actual size of combiner with delivery optics, and < 20 cm optical lever arm has been demonstrated in [14] and in Section 4.2 of this thesis. Scaling of this prototype to 10 and 100 kW with total length of combiner 100 cm and 240 cm respectively and optical lever arm for each channel ~ 20 cm is described in Section 9. For the case of coherent combining with DOE, optical lever arm will be determined by the number of channels which is equal to the number of diffraction orders utilized. Design of DOEs with tens and hundreds of diffraction

orders of equal diffraction efficiency is a new area of work, and it is not clear at this point how this design will be implemented. However, given a large solid angle that can be utilized, design of a combining system with short to moderate optical lever arm seems feasible, even for a large number of channels.

Based on the presented comparison, our conclusion is that spectral beam combining with volume Bragg gratings in PTR glass provides the shortest roadmap to compact and robust 10 and 100 kW class fiber laser systems.

Table 1.1. Comparison of spectral beam combining by volume Bragg gratings, surface gratings and coherent combining by diffractive optical elements.

Parameters	Volume grating	Surface grating	Coherent DOE
1. Laser sources			
1.1. Architecture	Laser	Laser*	MOPA
1.1. Spectral width	30 GHz	1 GHz	10 MHz
1.2. Threshold of SBS and SRS	High	Lower	Lowest
1.3. Polarization	Random	Linear	Linear
1.5. Beam splitting	No	No	Yes
1.6. Collimating lenses	No	Yes	Yes
1.7. Isolators	No	No	Yes
1.8. Phase control	No	No	Yes
2. Combiner			
2.1. Architecture	Passive	Passive	Active
2.2. Simplisity	Simple	More complex	Very complex
2.3. Tolerance to high power	High	High	High
2.4. Tolerance to environment	High	Low	Low
2.5. Optical lever arm	Small	Large	Small
2.6. Manufacturability	Commercial	Experimental	Experimental
3. Combined beam			
3.1. 100 kW in 50 nm	Feasible	More complex	Most complex
3.2. Divergence	Narrow	Narrow	Narrow
3.3. Sensitivity to back reflection	Low	Low	High
3.4. Demo at kW level	Yes	Yes	No
3.5. Steering	Conventional	Conventional	Nonmechanical

* If a MOPA is used, some of these ratings become more negative

CHAPTER TWO: VOLUME BRAGG GRATINGS IN PHOTO-THERMO-REFRACTIVE GLASS FOR SPECTRAL BEAM COMBINING

Modeling of Diffraction by Volume Bragg Gratings

Numerous papers on theoretical and experimental studying of volume Bragg gratings have been published over the last decades. A most widely used basis for description of such gratings is the theory of coupled waves developed by Kogelnik in 1969 [137]. Its results were applied for the further theoretical consideration [138,139,140,141] and treatment of experimental results observed for VBGs. There are several more approaches describing VBGs, e.g. rigorous coupled-wave analysis [142] and beam-propagation method [143]. However, Kogelnik's theory is still the most used approach for modeling volume gratings. This rather complicated theory has been reduced to simple practical formulae which could assist in design of diffractive optics based on volume Bragg gratings [2,144]. These papers consider diffraction of plane monochromatic, divergent, and polychromatic laser beams on uniform sinusoidal lossless transmitting and reflecting volume gratings. The following sections make extensive use of formulae and figures presented in these papers in order to explain properties of volume Bragg gratings, pertinent to spectral beam combining applications.

Basic Definitions

A sinusoidal uniform phase grating is a volume structure produced by refractive index modulation as it shown in Fig. 2.1. Each such structure recorded inside a plane-parallel plate of a photosensitive material could be considered as either transmitting or reflecting Bragg grating depending on its orientation in regard to the front surface and wavelength of a readout beam. Fig. 2.1 illustrates a comparison of transmitting and reflecting gratings produced by the same periodical structure in a photosensitive medium. Dotted arrows illustrates the beam tracing in transmitting grating geometry, and dashed arrows - in reflecting one. Solid arrows are the wave vectors of beams and the grating vectors as it is noted in this Figure's caption. In general case, volume Bragg gratings could be entirely described by the following set of parameters: the grating thickness t, an average refractive index of a medium n_{av}, an amplitude of refractive index modulation δn, the grating period Λ (or spatial frequency f=1/Λ), and the grating inclination angle φ between the normal to the grating front surface $\boldsymbol{N_f}$ and grating vector $\boldsymbol{K_G}$.

Grating vector $\boldsymbol{K_G}$ is directed as a medium normal to the planes of a constant refractive index and has a module $|\boldsymbol{K_G}|=2\pi f$. It is important to emphasize that a volume sinusoidal grating itself has doubled degeneration of directions of grating vectors due to its symmetry. For example, a volume grating is a transmitting grating for short wavelength radiation with large wave vector which crosses the left vertical surface and directed down to the bottom of the Fig. 2.1. The same grating is a reflecting one for long wavelength radiation with small wave vector which crosses the bottom surface and the grating vector is directed to the top of this Figure. An inclination angle φ which is the angle between the normal to the front surface $\boldsymbol{N_f}$ and the grating vector $\boldsymbol{K_G}$, is positive in counter-clockwise direction and can vary from $-\pi/2$ to $+\pi/2$. Transmitting grating

excited through the left vertical side of Fig. 2.1 has negative inclination; the same grating excited through the bottom side is a reflecting grating with positive inclination.

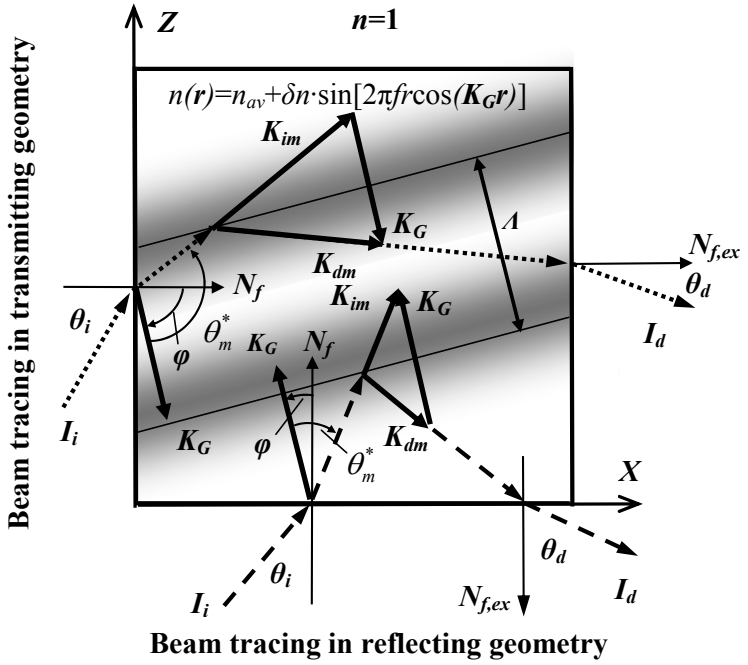

Figure 2.1. Ray tracing through a volume Bragg grating in transmitting (dotted lines) and reflecting (dashed lines) geometry. $\boldsymbol{N_f}$ and $\boldsymbol{N_{f,ex}}$ – normals to the front surface for incident (I_i) and diffracted (I_d) beams; $\boldsymbol{K_{im}}$, $\boldsymbol{K_{dm}}$ – wave vectors of incident and diffracted beams inside the grating medium; $\boldsymbol{K_G}$ - grating vector; φ – grating inclination; θ_i, θ_d – incident and diffraction angles; θ_m^* – incident Bragg angle.

Determination of angles in Bragg gratings is similar to those in classical geometrical optics. Fig. 2.1 shows an incident beam $\boldsymbol{I_i}$ approaches the front surface of the plate at angle θ_i, refracted into the medium at angle θ_{im}, and diffracted at angle θ_d. For describing of Bragg diffraction in all types of volume gratings regardless of type and inclination, let us introduce an incident Bragg angle in a medium, θ_m^*. This angle is determined as an angle between a grating vector $\boldsymbol{K_G}$ and a wave vector $\boldsymbol{K_i}$ of a refracted beam inside the medium, and it can vary from -π to +π. One can distinguish the following possible cases of Bragg diffraction depicted in Fig. 2.2. Positive orders of Bragg diffraction are for incident Bragg angle ranged from 0 to +π, i.e. for

counter-clockwise direction of an incident beam from grating vector. Similarly, negative orders of Bragg diffraction are for incident Bragg angle ranged from 0 to -π. The forward orders of Bragg diffraction are for a module of an incident Bragg angle less than π/2. The backward orders of Bragg diffraction are for a module of an incident Bragg angle more than π/2. Thus, depending on mutual orientation of grating and incident wave vectors, one can distinguish four Bragg orders, e.g. “plus forward” or “minus backward”, etc.

Traditionally used (beginning from its crystallography applications) conventional Bragg angle in the media θ_m has been determined as a positive angle not exceeding 90° between the plane of a constant refractive index and a direction of the beam propagation. As one can see from Fig. 2.2, the relationship between a Bragg angle and an incident Bragg angle is $\sin\theta_m = \left|\cos\theta_m^*\right|$. It is important to note that θ_m does not describe backward orders of diffraction which are important for practical modeling of volume Bragg gratings.

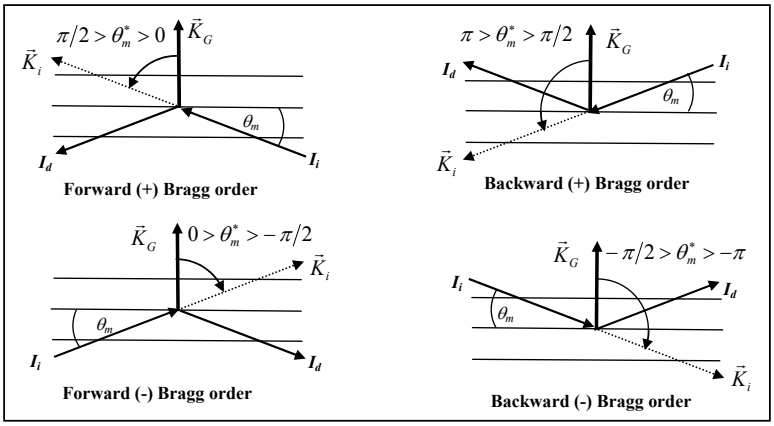

Figure 2.2. Possible orders of Bragg diffraction inside a medium.

Diffraction of Plane Waves by Transmitting Gratings

For volume Bragg gratings, diffraction of a beam with a certain wavelength occurs for the only one certain angle which depends on grating spatial frequency according to Bragg's condition:

$$\left|\cos\theta_m^*\right| = \frac{\lambda_0 f}{2n_{av}}. \tag{2.1}$$

In accordance with Kogelnik's theory [137], a solution of the scalar wave equation for transmitting VBG gives the following formula for diffraction efficiency (DE):

$$\eta = \frac{\sin^2\left(\xi^2 + \Phi^2\right)^{1/2}}{1 + \xi^2/\Phi^2}. \tag{2.2}$$

Here phase incursion Φ is the parameter which determines the maximum diffraction efficiency of VBG (grating strength) when the Bragg condition is obeyed while dephasing parameter ξ describes deviation from the Bragg condition by detuning from either θ_m^* or λ_0. Phase incursion in Bragg condition could be written as:

$$\Phi = \frac{\pi t \delta n}{\lambda_0 F_\varphi}, \tag{2.3}$$

where parameter F_φ is an inclination factor:

$$F_\varphi = \left[-\cos\left(\varphi - \theta_m^*\right)\cos\left(\varphi + \theta_m^*\right)\right]^{1/2}. \tag{2.4}$$

For normal transmitting gratings with $\varphi = \pm\pi/2$, the expression for the inclination factor is simplified and becomes:

$$F_{\pi/2} = \sin\theta_m^* = \sqrt{1 - \left(\frac{\lambda_0 f}{2n_{av}}\right)^2}. \tag{2.5}$$

The inclination factor describes additional optical path of incident and diffracted beams in a medium resulted from deviation of propagation from the normal to the grating surface.

According to Eq. (2.2), DE of a transmitting grating in Bragg condition (ξ=0) is a periodic function of phase incursion Φ and reaches 100% when

$$\Phi = \pi/2 + j\pi \text{, where } j=0, 1, 2\ldots \tag{2.6}$$

Substitution of this phase incursion into Eq. (2.3) at j=0 and considering a Bragg angle value from Eq. (2.1) gives a minimum thickness of grating t_0 which provides a 100% DE for a given refractive index modulation δn:

$$t_0 = \frac{\lambda_0 F_\varphi}{2\delta n}. \tag{2.7}$$

Dephasing parameter ξ takes into account small angular deviations $\Delta\theta_m$ from an incident Bragg angle θ_m^* and/or small deviations $\Delta\lambda$ from central wavelength λ_0:

$$\xi = \frac{\pi f t}{\cos\left(\varphi - \theta_m^*\right) - \dfrac{f\lambda_0}{n_{av}}\cos\varphi}\left(\Delta\theta_m \sin\theta_m^* - \frac{f}{2n_{av}}\Delta\lambda\right). \tag{2.8}$$

For a normal transmitting grating (φ=π/2) this expression is simplified and can be written as:

$$\xi_{\pi/2} = -\pi f t\left(\Delta\theta_m - \frac{f}{2n_{av}F_{\pi/2}}\Delta\lambda\right). \tag{2.9}$$

Interrelation between spectral and angular parameters could be obtained from differential form of Bragg condition (2.1):

$$\frac{\Delta\theta_m}{\Delta\lambda} = \frac{f}{2n_{av}F_{\pi/2}}. \tag{2.10}$$

Eq. (2.10) is a universal interrelation between spectral and angular selectivity of VBG that allows easy calculating of one of them from a given (or measured) another.

Angular selectivity of normal transmitting VBGs could be determined by substituting of Eqs. (2.3) and (2.8) into (2.2) at $\Delta\lambda=0$:

$$\eta(\Delta\theta_m)=\frac{\sin^2\left(\pi t\left(\left(\delta n/\lambda_0 F_{\pi/2}\right)^2+\left(f\Delta\theta_m\right)^2\right)^{1/2}\right)}{1+\left(\frac{\lambda_0 f F_{\pi/2}\Delta\theta_m}{\delta n}\right)^2}. \tag{2.11}$$

Dependence of diffraction efficiency on detuning from Bragg angle is shown in Fig. 2.3. Curve 1 corresponds to a 2-mm-thick VBG with 250-ppm refractive index modulation which provide 100% diffraction efficiency at 1085 nm. One can see a well known central maximum and a number of side lobes with gradually decreasing magnitude.

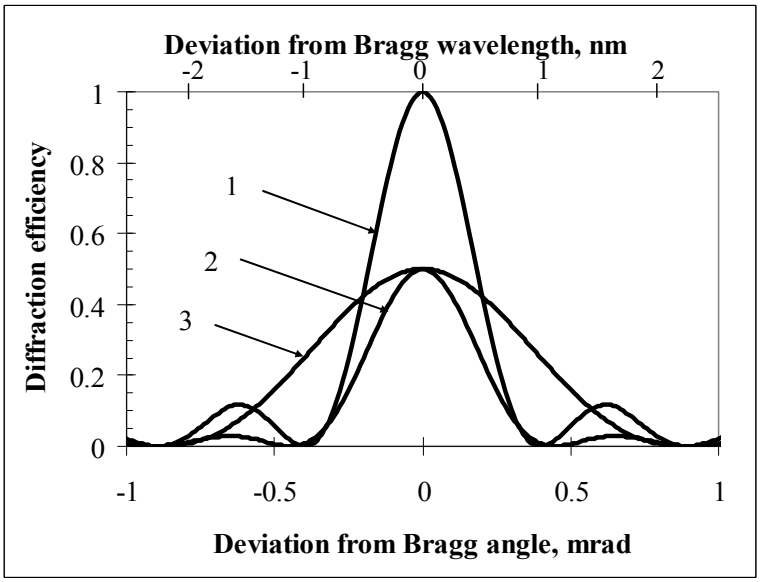

Figure 2.3. Angular and spectral selectivity of transmitting Bragg gratings for λ_0=1085 nm, n_{av}=1.4867. Grating thickness, mm: 1 and 2 – 2.0, 3 – 1.0. Refractive index modulation, ppm: 1 and 3 – 250, 2 – 125.

Curve 2 shows decreasing of DE resulted from decrease of refractive index modulation down to 125 ppm at the same grating thickness; this decreases diffraction efficiency at the central maximum down to 50%, but positions of minima and maxima of the side lobes practically are not changed. Curve 3 shows decreasing of DE resulted from decreasing of the thickness down to

1 mm at δn=250 ppm; this also provides DE of 50% but it causes dramatic widening of angular selectivity, when the first minimum moves to the position of the second minimum for a 2-mm-thick gratings.

It is important to note that Eq. (2.2) imposes the following criterion for equalizing of diffraction efficiency to zero:

$$\left(\xi^2 + \Phi^2\right)^{1/2} = j\pi \text{, where } j=1, 2, \ldots \text{ n, } \ldots \tag{2.12}$$

Let us determine angular selectivity inside the VBG medium at the HWFZ (Half Width at First Zero) level, $\delta\theta_m^{HWFZ}$, as the angle between the central maximum and the first minimum at the diffraction efficiency curve. For VBGs with 100% diffraction efficiency the following expression for the HWFZ angular selectivity could be given:

$$\delta\theta_m^{HWFZ} = \frac{\sqrt{3}}{2ft_0} \approx \frac{0.87}{ft_0}. \tag{2.13}$$

It should be noted that the HWFZ angular selectivity $\delta\theta_m^{HWFZ}$ is slightly smaller than the widely used grating parameter of FWHM angular selectivity which for 100%-efficient grating could be estimated as $\delta\theta_m^{FWHM} \approx 1/ft_0$.

By the same way as it was described above for angular selectivity, $\delta\lambda^{HWFZ}$ spectral selectivity is determined as a distance between the central maximum and the first zero in spectral distribution of DE which could be expressed by substitution of Eqs. (2.3) and (2.8) into Eq. (2.2) at $\Delta\theta_m$=0. In the case of normal transmitting grating, this expression is simplified by the use of Eq. (2.9):

$$\eta(\Delta\lambda) = \frac{\sin^2\left(\frac{\pi t}{F_{\pi/2}}\left(\left(\delta n/\lambda_0\right)^2 + \left(f^2\Delta\lambda/2n_{av}\right)^2\right)^{1/2}\right)}{1 + \left(\frac{f^2\lambda_0\Delta\lambda}{2n_{av}\delta n}\right)^2}. \tag{2.14}$$

Spectral selectivity has the same shape as angular selectivity due to their linear interrelationship described by Eq. (2.10). For the grating parameters of Fig. 2.3, this ratio is $\Delta\lambda/\Delta\theta \approx 500$ mm^{-1}. Thus, in addition of showing the angular selectivity of 2- and 1-mm-thick transmitting VBGs, Fig. 2.3 shows spectral selectivity of the same gratings which is represented by the upper horizontal axis of the figure. For normal transmitting gratings with 100% diffraction efficiency $\delta\lambda^{HWFZ}$ could be derived by substitution of Eq. (2.13) into Eq. (2.10):

$$\delta\lambda^{HWFZ} = \frac{\sqrt{3} n_{av} F_{\pi/2}}{f^2 t_0}. \tag{2.15}$$

HWFZ spectral selectivity of transmitting VBG could be easy varied from values below 0.1 nm to more than 100 nm by proper selection of grating parameters.

Diffraction of Plane Waves by Reflecting Gratings

Generally, diffraction efficiency of reflecting Bragg grating is described by the following formula [137]:

$$\eta = \left(1 + \frac{1 - \xi^2/\Phi^2}{\sinh^2\sqrt{\Phi^2 - \xi^2}}\right)^{-1}. \tag{2.16}$$

Here Φ and ξ are the same phase incursion at Bragg condition and dephasing parameter at certain detuning from Bragg condition. According to [137], these parameters should be redefined for reflecting VBGs:

$$\Phi = \frac{i\pi t \delta n}{\lambda_0 F_\varphi}, \tag{2.17}$$

$$\xi = \frac{\pi f t}{\cos\left(\varphi - \theta_m^*\right) - \dfrac{f\lambda_0}{n_{av}}\cos\varphi}\left(-\Delta\theta_m \sin\theta_m^* + \frac{f}{2n_{av}}\Delta\lambda\right). \tag{2.18}$$

For un-slanted reflecting gratings (φ=0), these parameters become:

$$\Phi_0 = \frac{\pi t \delta n}{\lambda_0 \left|\cos\theta_m^*\right|} = \frac{2\pi n_{av} t \delta n}{\lambda_0^2 f}, \tag{2.19}$$

$$\xi_0 = \frac{\pi f t \Delta\lambda}{\lambda_0}. \tag{2.20}$$

Spectral selectivity could be described in the terms of Bragg grating parameters:

$$\eta(\Delta\lambda) = \left(1 + \frac{1 - \left(\dfrac{\lambda_0 f^2 \Delta\lambda}{2n_{av}\delta n}\right)^2}{\sinh^2\left(\left(\dfrac{2\pi n_{av} t \delta n}{\lambda_0^2 f}\right)^2 - \left(\dfrac{\pi f t \Delta\lambda}{\lambda_0}\right)^2\right)^{1/2}}\right)^{-1}. \tag{2.21}$$

Diffraction efficiency of reflecting Bragg grating strongly depends on grating thickness t and refractive index modulation δn. If reflecting VBG is at exact Bragg condition ($\Delta\theta_m$=$\Delta\lambda$=0), ξ=0, and maximum of the grating diffraction efficiency could be simplified from Eq. (2.16) as

$$\eta_0 = \tanh^2 \frac{\pi t \delta n}{\lambda_0 \left|\cos\theta_m^*\right|}. \tag{2.22}$$

Following the behavior of a hyperbolic tangent function, diffraction efficiency maximum asymptotically approaches the 100% value by increasing of grating thickness and/or refractive index modulation.

Fig. 2.4 illustrates this interrelation for four different values of diffraction efficiency η_0: 90% which correspond to 10-dB transmitted-beam-attenuation, 99% (20 dB), 99.9% (30 dB), and 99.99% (40 dB) at λ_0=1085 nm for normal beam incidence onto a grating. It should be noticed that refractive index modulation δn is less than 1000 ppm only when the grating thickness is more than 1 mm for securing the diffraction efficiency level of η_0=99% (20 dB

attenuation). Therefore, reflecting VBGs should be thick enough for securing of their efficient reflection at relatively low values of refractive index modulation.

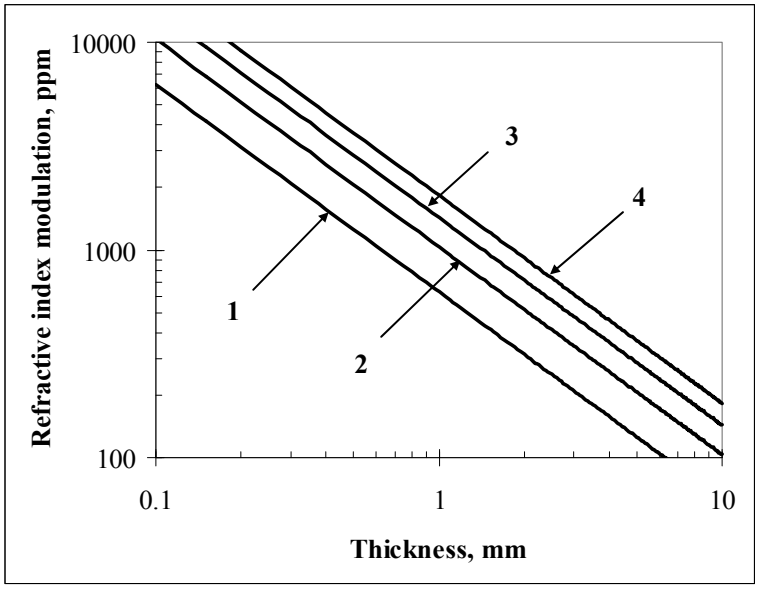

Figure 2.4. Dependence of refractive index modulation on grating thickness that provides the following diffraction efficiency of a reflecting VBG: 1 – 90%, 2 – 99%, 3 – 99.9%, 4 – 99.99%. λ_0=1085 nm, n_{av}=1.4867.

To determine spectral selectivity $\delta\lambda^{HWFZ}$ at HWFZ level, Eq. (2.16) should be equalized to zero. Diffraction efficiency reaches zero value at multiple points:

$$\left(\xi^2 - \Phi^2\right)^{1/2} = j\pi, \text{ where } j=1, 2, \ldots, n, \ldots \tag{2.23}$$

Generally, for determining of spectral selectivity as the HWFZ level, $\delta\lambda^{HWFZ}$, one should substitute Eqs. (2.17) and (2.18) into (2.23) at j=1. However, this general result could be considerably simplified for un-slanted gratings with diffraction efficiency η_0:

$$\delta\lambda^{HWFZ} = \frac{\lambda_0\left(\left(\operatorname{atanh}\sqrt{\eta_0}\right)^2 + \pi^2\right)^{1/2}}{\pi f t}. \tag{2.24}$$

Estimation of typical values of spectral selectivity $\delta\lambda^{HWFZ}$ for η_0=99%, λ_0=1085 nm, n_{av}=1.485, gives the following formula for normal beam incidence:

$$\delta\lambda^{HWFZ}\left[nm\right]\cong\frac{0.55}{t\left[mm\right]}. \tag{2.25}$$

It should be noted that a grating with fixed thickness t exhibits lower diffraction efficiency η_0 for smaller δn, and spectral selectivity of such a grating is narrower.

Derivation of a basic interrelation between angular and spectral parameters for reflecting VBGs could be performed similarly to the procedure described for transmitting Bragg gratings. Expressing Bragg condition, Eq. (2.1), in its differential form and considering of the second order for angular deviation from exact Bragg angle, one can write the interrelation formula for spectral and angular parameters for reflecting gratings:

$$\Delta\theta_m^{1,2}=\pm\left(\tan^2\theta_m^*+\frac{2\Delta\lambda}{\lambda_0}\right)^{1/2}+\tan\theta_m^*. \tag{2.26}$$

Angular selectivity of reflecting VBGs can be calculates by substitution of $\Delta\lambda=\delta\lambda^{HWFZ}$ into Eq. (2.26). Two different definitions of spectral selectivity can be introduced. The difference between the two definitions and applicability to particular diffraction problems is described in [144]. For gratings and geometry used in spectral beam combining, Half-Width at First Zero level, $\delta\theta_m^{HWFZ}$, definition should be used. HWFZ selectivity determines angular distance between the maximum of diffraction efficiency and its first zero in angular selectivity curve:

$$\delta\theta_m^{HWFZ}=\left|\Delta\theta_m^1\right|=\left(\tan^2\theta_m^*+\frac{2\delta\lambda^{HWFZ}}{\lambda_0}\right)^{1/2}-\tan\theta_m^*. \tag{2.27}$$

Fig. 2.5 shows that HWFZ angular selectivity dramatically depends on both incident Bragg angle θ_m^* and VBG thickness t. For instance, 10-mrad HWFZ selectivity is secured at θ_m^*=10° for 0.3-mm-thick grating, or at θ_m^*=2° for a grating with 1.25 mm thickness.

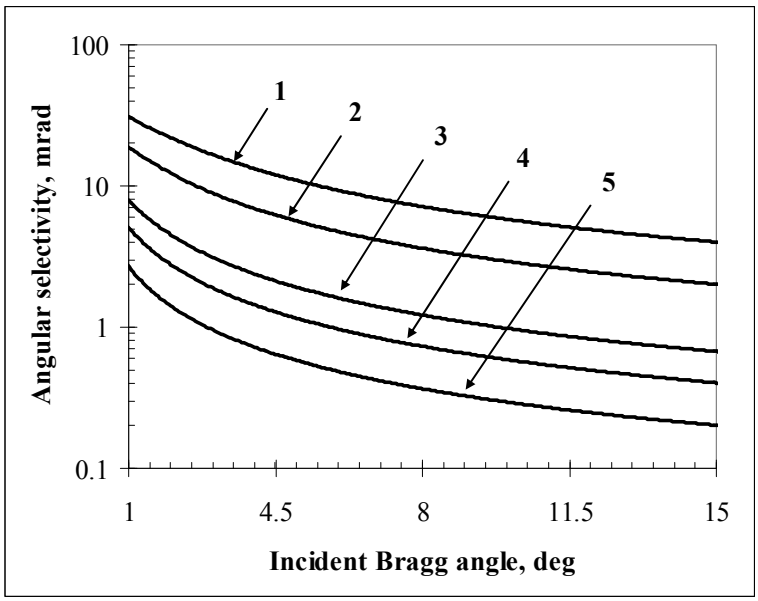

Figure 2.5. HWFZ angular selectivity of reflecting VBGs as a function of incident angle for different VBG thickness: 1 – 0.5 mm, 2 – 1.0 mm, 3 – 3.0 mm, 4 – 5.0 mm, 5 – 10.0 mm. (λ_0=1085 nm, n_{av}=1.4867).

Diffraction of Divergent and Polychromatic Beams

Let us consider diffraction of a monochromatic beam which has divergence that could be approximated by a Gaussian function. If the direction of the beam propagation matches the Bragg condition, normalized intensity in the angular space could be expressed as:

$$G_1(\theta, b) = \exp\left[-2\left(\frac{\theta - \theta_m}{b}\right)^2\right]. \tag{2.28}$$

For diffraction-limited beams, $HWe^{-2}M$ divergence b is inversely-proportional to beam diameter. Diffraction of a divergent beam by a volume Bragg grating is described by a convolution in the angular space of functions given by Eqs. (2.2) and (2.28) for a transmitting VBG or Eqs. (2.16) and (2.28) for a reflecting VBG:

$$\eta_\theta(b) = \sqrt{\frac{2}{\pi}} \frac{1}{b} \int \eta(\theta) G_1(\theta, b) d\theta \,. \tag{2.29}$$

Fig. 2.6. shows angular selectivity of a transmitting VBG with $\delta\theta_m^{HWFZ}$=0.4 mrad and 100% diffraction efficiency for a plane monochromatic wave at 1085 nm for four beams with different divergence *b*. As long as beam divergence is much smaller than angular selectivity of the grating (curve 1 corresponding to *b*=0.04 mrad), there is no decrease of diffraction efficiency compared to the plane wave case and minima of the curve reach zero values.

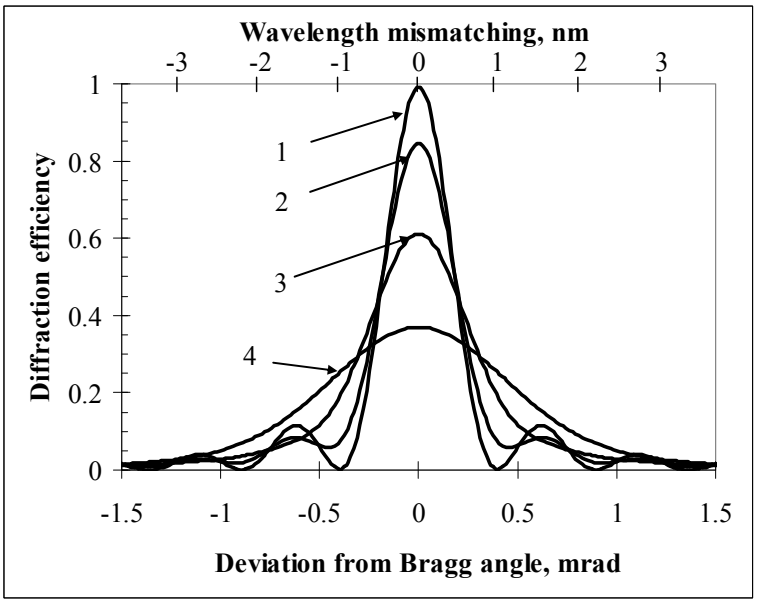

Figure 2.6. Diffraction efficiency of a transmitting VBG with angular selectivity 0.4 mrad for Gaussian beams with different divergence: 1 – 0.04 mrad, 2 – 0.2 mrad, 3 – 0.4 mrad, 4 – 0.8 mrad.

However, if beam divergence becomes comparable to the grating selectivity, dramatic decrease of diffraction efficiency occurs (curves 2-4). When beam divergence and grating selectivity values are equal, $b=\delta\theta_m^{HWFZ}$, maximum diffraction efficiency is only about 60%. Additionally, the side-lobes are flattening for beams with increased divergence, local minima of angular

selectivity start to differ from zero significantly, and at $b \geq \delta\theta_m^{HWFZ}$ =0.4 mrad the selectivity curve does not have any local minima at all.

Similarly, Bragg diffraction of polychromatic beams can be considered. For simplicity, let us assume Gaussian shape of spectral distribution:

$$G_2(\lambda, w) = \exp\left[-2\left(\frac{\lambda - \lambda_0}{w}\right)^2\right], \tag{2.30}$$

where w is the $HWe^{-2}M$ spectral width and λ_0 is a central wavelength of the beam. Modeling of diffraction can be performed similarly to modeling for divergent beams. Diffraction efficiency of for such beams could be calculated from a convolution of diffraction efficiency for a monochromatic wave described by Eq. (2.14) for transmitting VBGs or Eq. (2.21) for reflecting VBGs with the Gaussian spectral distribution described by Eq. (2.30). This gives us the adjusted value of diffraction efficiency $\eta_\lambda(w)$:

$$\eta_\lambda(w) = \sqrt{\frac{2}{\pi}}\frac{1}{w}\int \eta(\lambda) G_2(\lambda, w) d\lambda\,. \tag{2.31}$$

Similarly to diffraction of Gaussian beams on transmitting Bragg gratings described above, we will consider diffraction by reflecting Bragg gratings by comparing grating selectivity with the beam spectral width and/or angular divergence. Results of numerical calculations of Bragg diffraction by reflecting gratings are shown in Fig. 2.7, where different polychromatic beams are diffracted by a 1.1-mm-thick grating which has DE=99% at normal incidence. According to Eq. (2.24), this VBG has 0.5 nm spectral selectivity. One can see that diffraction efficiency is decreased for beams with larger spectral width; diffraction efficiency is about 60% when $w=2\delta\lambda^{HWFZ}$. In comparison with the same dependence of spectral selectivity for transmitting gratings described above, where 60%-level of DE corresponds to $w=\delta\lambda^{HWFZ}$, one can conclude that spectral width of incident beams is twice less restrictive parameter for reflecting

VBGs in comparison with the transmitting ones. Also, side lobes in the spectral selectivity curves are beginning to disappear when spectral width of the beam is approximately half of spectral selectivity of the grating ($2w \geq \delta\lambda^{HWFZ}$); total flattening of the DE curve occurs when spectral width of the beam is equal or higher than spectral selectivity of the grating ($w \geq \delta\lambda^{HWFZ}$).

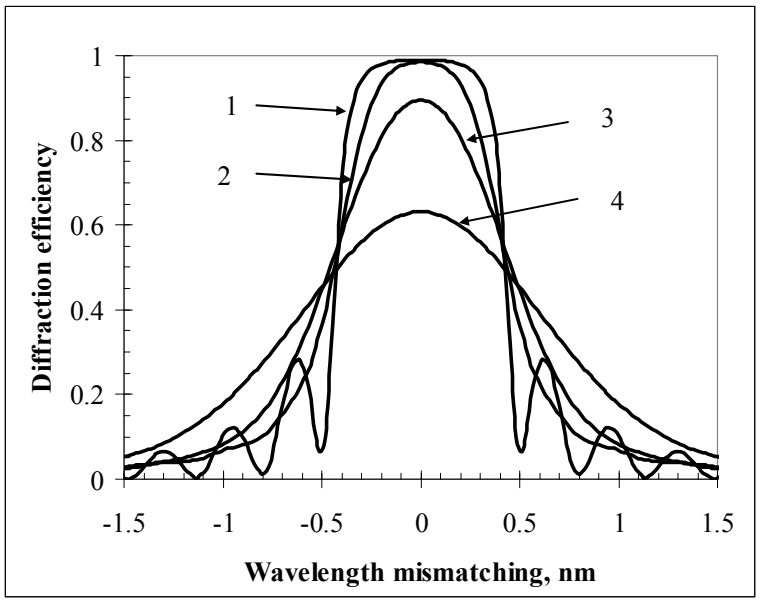

Figure 2.7. Diffraction efficiency of a reflecting VBG with 99% plane-wave efficiency 0.5 nm spectral selectivity at normal incidence for polychromatic beams with different spectral width: 1 – 0.05 nm, 2 – 0.25 nm, 3 – 0.5 nm, 4 – 1.0 nm.

Fig. 2.8 shows diffraction efficiency versus beam divergence and spectral width for a transmitting VBG that has 100% efficiency for plane monochromatic waves. One can see that about 60% when beam spectral width w is equal to the grating spectral selectivity $\delta\lambda$ and divergence b is equal to the grating angular selectivity $\delta\theta$. Diffraction efficiency is 99% when either w or b is approximately 8 times smaller than grating selectivity $\delta\lambda$ or $\delta\theta$. This is the main factor which determines efficiency of SBC for real laser systems.

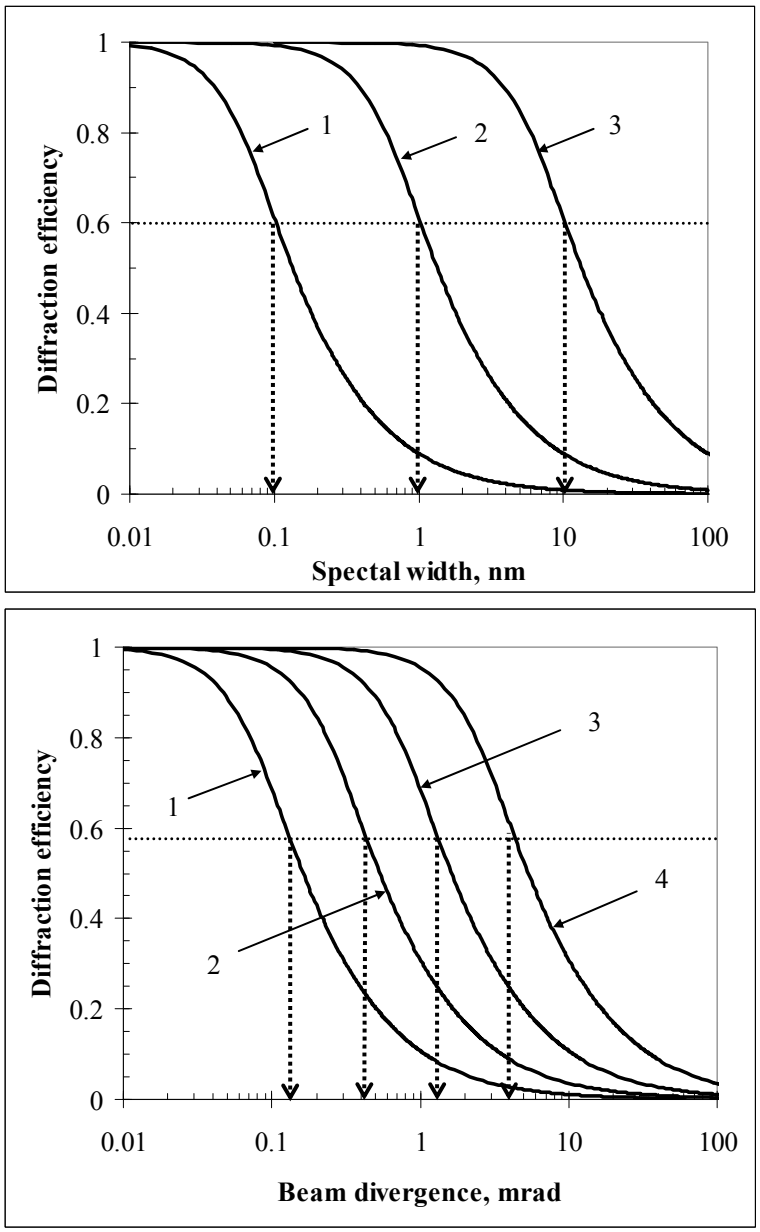

Figure 2.8. Diffraction efficiency of a transmitting VBG with 100% diffraction efficiency for a plane monochromatic wave at λ_0=1085 nm versus spectral width w (top) and divergence b (bottom) of laser beam. HWZ spectral selectivity of the grating: 1 – 0.1 nm, 2 – 1.0 nm, 3 – 10 nm (top). HWZ angular selectivity of the grating: 1 – 0.12 mrad, 2 – 0.4 mrad, 3 – 1.2 mrad, 4 – 4.0 mrad (bottom). Dotted lines correspond to diffraction efficiency of a beam with w and b equal to grating selectivity.

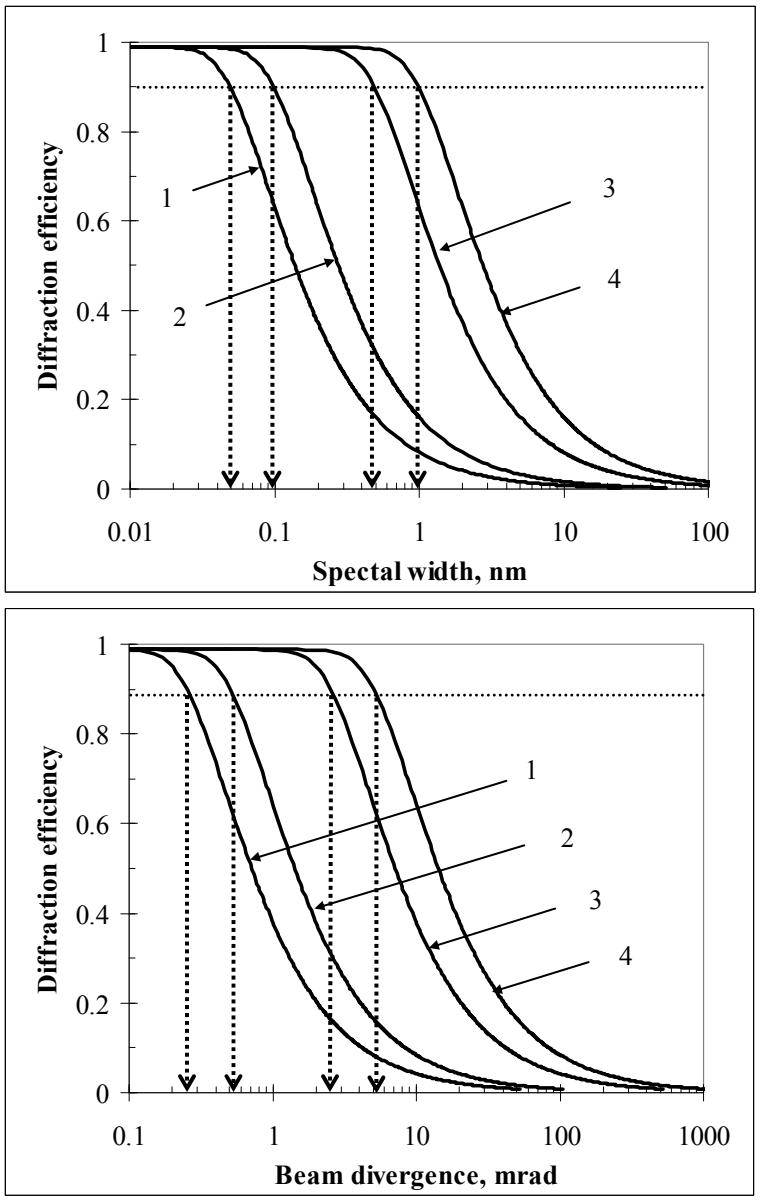

Figure 2.9. Diffraction efficiency of a reflecting VBG with 99% diffraction efficiency for a plane monochromatic wave at λ_0=1085 nm versus spectral width w (top) and divergence b (bottom) of laser beam. HWZ spectral selectivity of the grating: 1 – 0.05 nm, 2 – 0.1 nm, 3 – 0.5 nm, 4 – 1.0 nm (top). HWZ angular selectivity of the grating: 1 – 0.26 mrad, 2 – 0.52 mrad, 3 – 2.6 mrad, 4 – 5.2 mrad (bottom). Dotted lines correspond to diffraction efficiency of a beam with w and b equal to grating selectivity.

Fig. 2.9 shows diffraction efficiency versus beam divergence and spectral width for a reflecting VBG that has 99% efficiency for plane monochromatic waves. One can see that diffraction efficiency is about 90% when beam parameters w and b are equal to HWZ selectivity

of the grating. Decreasing of diffraction efficiency to 98% occurs when beam spectral width w and angular divergence b are approximately half of HWZ selectivity of the grating. Thus, high efficiency reflecting VBGs are less restrictive to spectral width and angular divergence of laser beams compared to transmitting VBGs.

Design of Volume Bragg Gratings for Spectral Beam Combining

Design of volume Bragg grating for spectral beam combining of real beams is a procedure of optimizing grating parameters such as period, thickness, and refractive index modulation based on the combining geometry, parameters of individual lasers (beam diameter, divergence, spectral width), and desired spectral separation of channels. The goal of this procedure is to minimize diffraction losses in the spectral beam combining system.

Design procedure is different for transmitting and reflecting gratings. The main difference is behavior of peak diffraction efficiency of gratings as thickness or refractive index modulation is increased. It can be seen from Eq. (2.22) that diffraction efficiency maximum asymptotically approaches 100% as grating thickness and/or refractive index modulation is increased. On the contrary peak diffraction efficiency of transmitting gratings cycles between 0 and 100% following a sine-squared function as can be seen from Eq.(2.2) by substituting Φ from Eq. (2.3) and setting ξ=0. Therefore, transmitting Bragg gratings require much careful selection of thickness and refractive index modulation in order to achieve diffraction efficiency close to 100%. Fig. 2.10 illustrates design procedure for transmitting VBGs used for spectral beam combining [145]. Design procedure consists of the following steps. First, desired spectral separation between channels determines a curve with specific $\Delta\lambda$. Next geometry of SBC system

is considered and desired Bragg angle is specified. Since spatial frequency of the grating is related to Bragg angle by Eq. (2.1), this determines a vertical line in Fig. 2.10. Intersection of these two lines allows determination of exact grating thickness and refractive index modulation required for efficient spectral beam combining. Therefore, all basic parameters of a required grating are determined.

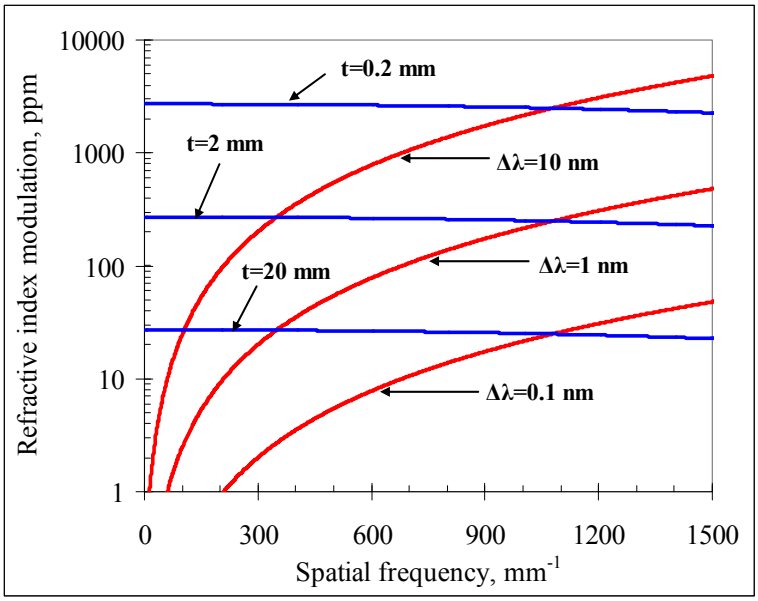

Figure 2.10. Refractive index modulation as a function of spatial frequency for transmitting VBGs optimized for spectral beam combining. Curves for different grating thicknesses correspond to 100% peak diffraction efficiency. Curves for different Δλ correspond to the respective distance between the peak and first zero of spectral dependence of diffraction efficiency. Gratings suitable for spectral beam combining are determined by intersections of the two sets of lines.

It can be seen from Fig. 2.10 that transmitting VBGs are suitable for spectral beam combining with spectral separation of channels > 1 nm. This corresponds to the top-left part of the figure. Transmitting gratings suitable for spectral separation have relatively small thickness and low spatial frequency (small Bragg angle). Such gratings are not very sensitive to polarization of incident beams and provide sufficient angular selectivity to combine beams with divergence > 50 μrad. For example, spectral beam combining of two beams with 2.2 nm spectral

separation using a transmitting Bragg grating with absolute efficiency > 90% is discussed in the experimental part of this thesis.

However, when smaller channel spacing is considered, corresponding to lower-right part of Fig. 2.10, thick gratings with large Bragg angles (>20 degrees) are required. Narrow angular selectivity of such gratings requires large-aperture near-diffraction-limited beams with angular divergence < 50 μrad. Another consequence of large Bragg angles is polarization sensitivity. It was found that thin reflecting VBGs used at near-normal incidence are much more advantageous for high-density SBC (2 channels/nm and higher) due to polarization insensitivity and wider angular selectivity. Wide angular selectivity means that smaller beams with higher divergence can be used. Additional technological advantage is that better grating uniformity can be achieved over the smaller aperture of gratings.

Design of reflecting gratings for spectral beam combining is more straight-forward. Grating frequency is determined by desired Bragg angle, which is selected based on system geometry considerations. If polarization insensitivity is desired, Bragg angle should be kept below 10-15 °. Next, grating thickness is calculated based on the required spectral separation of channels using Eq. (2.24), where η_0 is usually set to 99% for practical reasons. Finally, refractive index modulation necessary to achieve specified efficiency is calculated from Eq. (2.22).

It should be noted that according to Eq. (2.27), smaller spectral selectivity of reflecting gratings results in smaller angular selectivity. This means that reflecting VBGs designed for a particular case of spectral beam combining of small-diameter beams with high divergence and small spectral separation of channels will experience diffraction losses, as described previously. Due to the shape of spectral selectivity curve of high-efficiency reflecting VBGs, primary losses occur for beams that are transmitted through the grating, due to wavelength offset from Bragg

condition, during spectral beam combining. These losses, resulting from finite beam divergence, can significantly deteriorate SBC system efficiency. An effective solution to minimizing these losses is to restrict the range of refractive index modulation and place neighboring channels into higher-order minima of spectral selectivity curve. Using an optimization procedure, gratings that provide high efficiency for diffracted beams and low losses for transmitted beams can be designed. An abundant number of examples of reflecting VBGs optimized for high-spectral-density combining of small-diameter beams can be found in the following chapters. For illustrative purposes spectral selectivity of a reflecting VBG optimized for combining of beams with 1 mrad divergence with 0.2 nm spectral separation of channels at 5° angle of incidence is shown in Fig. 2.11.

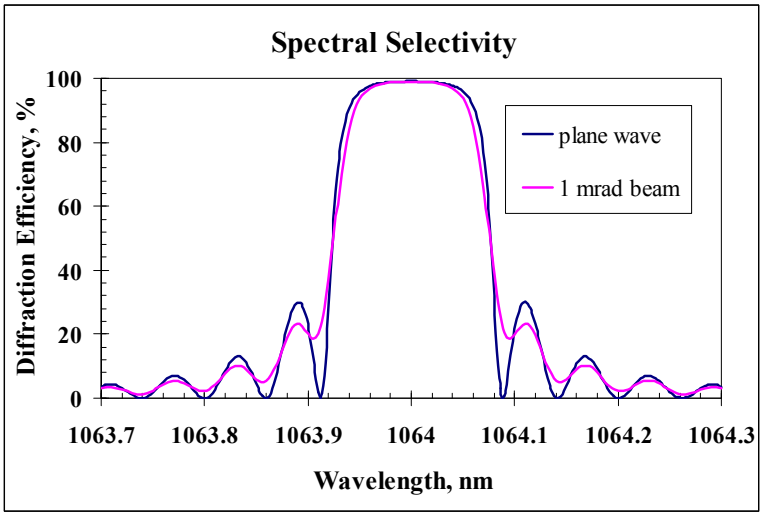

Figure 2.11. Spectral selectivity of a VBG designed for SBC with 0.2 nm channel spacing.

Optimized grating has thickness of 6.0 mm, refractive index modulation of 170 ppm and Bragg wavelength of 1065.83 nm at normal incidence. Diffraction efficiency of such grating is ~ 99% at Bragg condition and ~ 2% at +/-0.2 nm detuning (3-rd minimum). Losses at detuned wavelength can be further decreased if this grating is used at Bragg angles smaller than 5°.

Photo-thermo-refractive Glass

High-efficiency VBG recording in photo-thermo-refractive (PTR) glass has been developed [146]. While being photo-sensitive in the UV, PTR glass offers high transmittance in the near-IR and visible parts of spectrum with absorption comparable to the best available commercial optical glasses. Moreover, PTR glass has excellent thermo-mechanical properties with refractive index practically independent of temperature ($dn/dT<10^{-8}$ K^{-1}). These features enable VBGs in PTR glass to withstand high-power laser radiation, making them ideal elements for high-power SBC. In this section, a short review of basic properties of PTR glass, adopted from [147], is presented.

Table 2.1. Typical PTR glass composition, from [148].

Glass component	mol.%	Function
SiO_2	72.3	Glass matrix
Na_2O	13.6	
ZnO	5.2	
Al_2O_3	2.3	
NaF	3.7	Microcrystal constituents
AlF_3	1.3	
Ag_2O	0.01	Photosensitive agents, optical sensitizer
KBr	1.5	
CeO_2	0.01	
Sb_2O_3	0.03	Thermal sensitizers, redox agents, refining agents
SnO_2	0.02	

PTR glass is a highly homogeneous and transparent sodium-zinc-aluminum-silicate glass doped with silver, cerium, fluorine, and bromine. Table 2.1 summarizes the importance of each

element in the composition of PTR glass. Absorption spectrum of PTR glass is given in Fig. 2.12. An absorption band peak characteristic of Ce^{3+} ions is located at about 4 eV (305 nm).

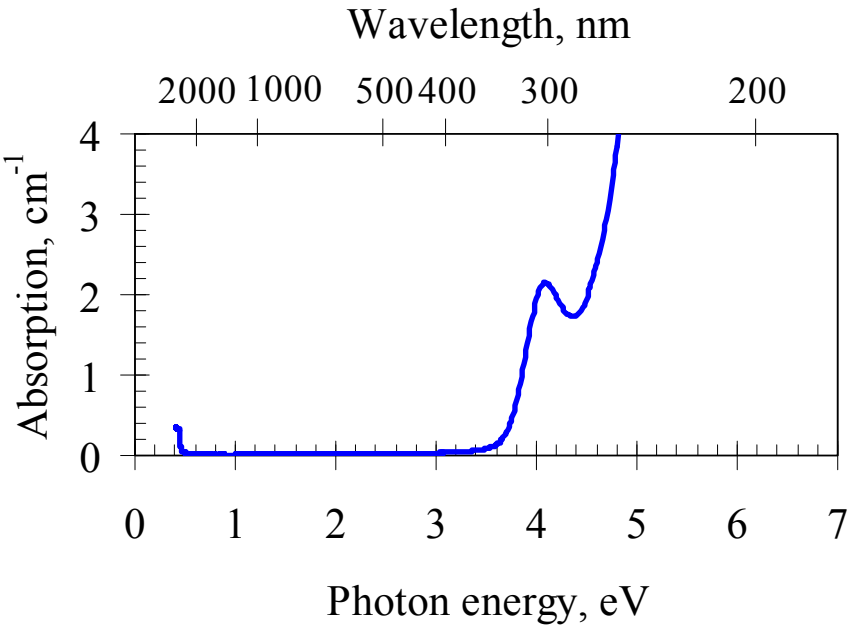

Figure 2.12. Absorption spectrum of typical PTR glass.

PTR glass is a crown-type optical glass characterized by having a refractive index at 587.5 nm equal to 1.4959 and an Abbe number of 59.2. Linear photosensitivity is determined by photoexcitation of Ce^{3+} ions. Typically near ultraviolet radiation is used for exposure. The electrons that are released from cerium are trapped by silver ions to form neutral silver. Thermal development at temperatures in the range 450-500 °C leads to diffusion of silver atoms and formation of silver containing particles. These particles serve as nucleation centers for sodium fluoride crystal growth at temperatures between 500 and 550 °C. After this final step a refractive index change of up to 10^{-3} occurs between exposed and unexposed areas in the glass. The refractive index change is actually a decrement because NaF crystals have a lower index value than the surrounding glass. However because the volume fraction of NaF is limited the maximum refractive index decrease amounts to 10^{-3}. The linear photosensitivity characteristics

of PTR glass exposed to continuous-wave laser light from a Helium-Cadmium laser at 325 nm are shown in Fig. 2.13.

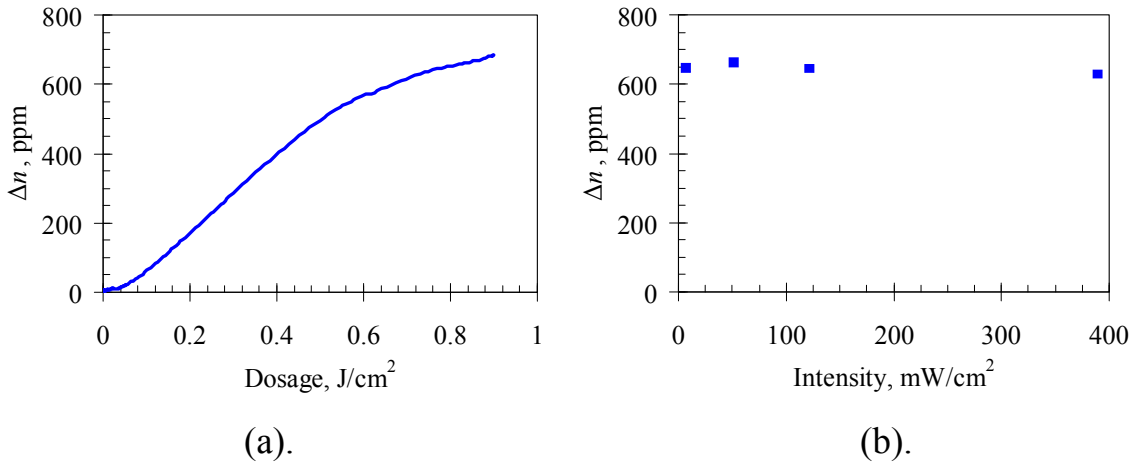

Figure 2.13. Linear photosensitivity of PTR glass.

A major advantage of PTR glass is that is has crystalline phase embedded in a glass matrix. The consequence is that the NaF crystals responsible for refractive index change are able to handle high temperatures and are resistant to high-energy laser irradiation.

CHAPTER THREE: SPECTRAL BEAM COMBINING WITH TRANSMITTING VOLUME BRAGG GRATINGS

Prior to this experiment, our research group demonstrated that transmitting volume Bragg gratings are suitable dispersive optical elements for spectral beam combining of high-power laser beams. Two Yb-fiber lasers with 11 nm difference in their central wavelengths (1085 and 1096 nm) were combined into a single near-diffraction-limited beam with total power of 165 W by means of a transmitting VBG [134]. Combining efficiency of 95% at 30 W output power and 92% at 165 W output power was achieved. However, the design of a high-power spectrally-combined laser system with a large number of channels requires the reduction of spectral separation between channels. The experiment described in this section is the first of the series of experiments aimed at reducing spectral separation of channels in spectral beam combiners is based on volume Bragg gratings. The goal of the experiment was to reduce the spectral separation of channels by a factor of 5 compared to the previous demonstration (from 11 to 2.2 nm) and identify possible limitations of high-density spectral beam combining using transmitting volume Bragg gratings.

A transmitting VBG for spectral beam combining with 2.2 nm channel spacing around 1090 nm has been designed and recorded in PTR glass. The grating has refractive index modulation of 165 ppm, period of 1.6 μm, and thickness of 3.1 mm. The Bragg condition is satisfied for this grating at angle of incidence about 20° (in air). The Spectral selectivity of this grating (defined here as half width to first zero) is about 2.2 nm and angular selectivity (half

width to first zero) is about 715 μrad. Spectral dependence of theoretical diffraction efficiency for a plane wave and diffraction efficiency measured with a near-diffraction-limited beam with 7 mm diameter ($FWe^{-2}I$) are shown in Fig. 3.1. The Small difference between the two curves is attributed to finite divergence and spectral width of the laser beam and small grating vector non-uniformity across the beam aperture.

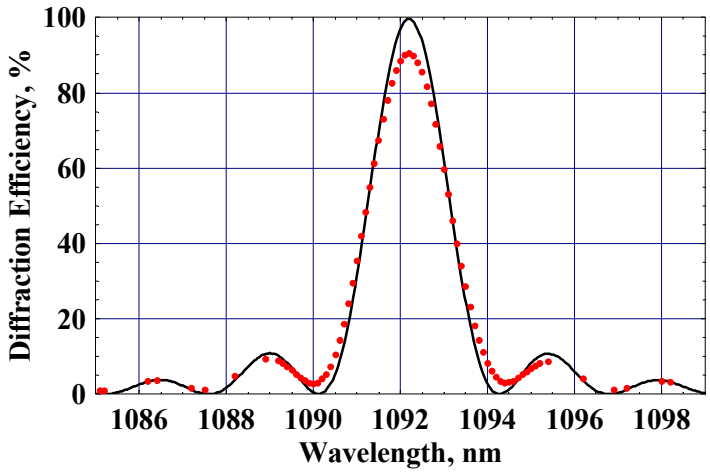

Figure 3.1. Spectral dependence of diffraction efficiency of a transmitting VBG used for spectral beam combining with 2.2 nm spectral separation of channels. Line – modeling for a plane monochromatic wave; points – scanned with a 7-mm-diameter near-diffraction-limited beam, 0.1 nm laser linewidth.

This grating was used to combine two laser beams with combining efficiency > 90%. Efficient beam combining is achieved when one of the beams satisfies the Bragg condition and is diffracted by the grating, while another beam is detuned from the Bragg condition to correspond to one of the minima. This detuning defines channel separation in a beam combiner. The two beams with offset wavelengths (λ_1=1090.0 nm, λ_2=1092.2 nm) are incident on the grating at equal angles from the opposite sides of a normal to the grating vector $\boldsymbol{K}_G$, as shown in Fig. 3.2. The angle of incidence α is determined by Bragg condition for λ_2 (about 20°). Since Bragg condition is satisfied for a beam with wavelength λ_2, this beam is mostly diffracted (deflected by twice the Bragg angle). The beam with wavelength λ_1 is offset from the Bragg condition into the

first minimum of diffraction efficiency curve (Fig. 3.1) and is mostly transmitted. The system is aligned such that the two beams emerging from the grating are overlapped and collinear. We define absolute system efficiency as a ratio of power in a combined beam divided by the sum of powers of incident beams, for incident beams of the same power. This definition ensures equal contribution of losses that each beam experiences (which are usually not the same) to the overall system efficiency. In other words, absolute system efficiency is the average of absolute propagation efficiencies of the two beams. Sources of losses in the system arise from diffraction efficiency being < 100% at Bragg condition and > 0% at the first zero of spectral selectivity, as well as from scattering and absorption of the grating and small reflection from AR-coated sample surfaces. Absolute combining efficiency for this system is measured at 90.6%.

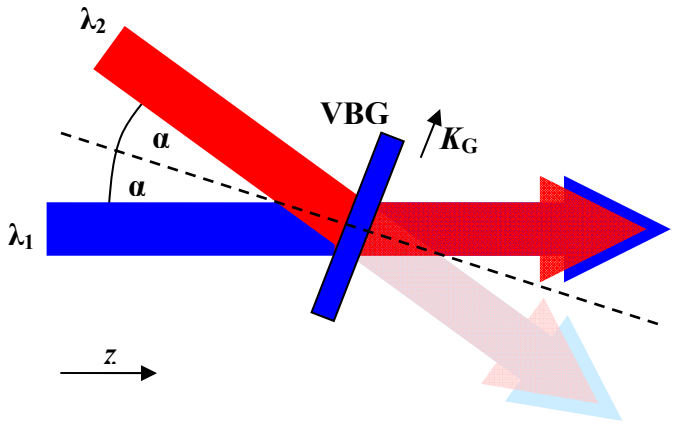

Figure 3.2. Optical layout of spectral beam combining with a transmitting volume Bragg grating (top view). Combined beam propagates along z axis.

Propagation properties of output beams (diffracted, transmitted and combined) are studied in two orthogonal directions, perpendicular to the direction of propagation z. For simplicity, we call direction that is perpendicular to z and lies in the plane of diffraction as "horizontal" and direction perpendicular to the plane of diffraction as "vertical," according to our laboratory coordinate system. Propagation properties of the studied beams are characterized by a

"times-diffraction-limit" (TDL) factor, commonly known as M^2 [149]. It shows how many times far-field divergence of a real beam is greater than divergence of a perfect diffraction-limited Gaussian beam of the same size. The International Standard Organization (ISO) determines that beam sizes have to be measured by the second moment definition [150]. To find the TDL factor, the beams are focused with a lens and scanned with 2.5 μm slits in 5 planes along the direction of propagation (z). Beam sizes in 5 planes, calculated by the second-moment integral, are fit to a hyperbolic equation to find the TDL factors (or M^2) along with z_0 and W_0 [150,151]:

$$W(z) = W_0 \sqrt{1 + \left(\frac{M^2 \lambda}{\pi W_0} \right)^2 (z - z_0)^2} , \tag{2.1}$$

where z is position along direction of propagation, $W(z)$ – beam size at position z, W_0 – minimum beam size (at the waist), and z_0 – location of the waist.

Table 3.1. TDL factors (M^2) of laser beams in two orthogonal directions, indicating the ratio of beam divergence to diffraction-limited divergence of a Gaussian beam with the same diameter. Absolute accuracy of measurement ±0.05; incident beams have $M^2 = 1.05$ in both planes.

Measurement direction	Transmitted beam	Diffracted beam	Combined beam
Vertical	1.08	1.12	1.13
Horizontal	1.09	1.30	1.35

Input beams are collimated using a wedge-plate shearing interferometer and have M2 ~ 1.05 due to single-mode fiber and high-quality collimators used for beam delivery. It was found that the transmitted beam has almost the same TDL factor as the incident beam in both vertical and horizontal directions (Table 3.1). This shows that optical homogeneity and surface quality of a PTR-glass volume Bragg grating are sufficiently high and do not increase divergence of laser beams significantly. The TDL factor of the diffracted beam is almost unchanged in the vertical plane, while it is increased to ~ 1.3 in the horizontal plane.

Fig. 3.3 shows dependence of beam diameters on position along the direction of beam propagation. One can see that propagation properties of transmitted, diffracted and combined beams are the same in the vertical plane. In the horizontal plane, however, not only are beam waist diameters different, but their positions are also different for transmitted and diffracted beams. As a result, the combined beam has divergence of 1.35 times diffraction limit. It is important that due to different locations of waists for transmitted and diffracted beams, the TDL factor of the combined beam is not an average of the values of the individual beams, but exceeds the TDL factor of both beams.

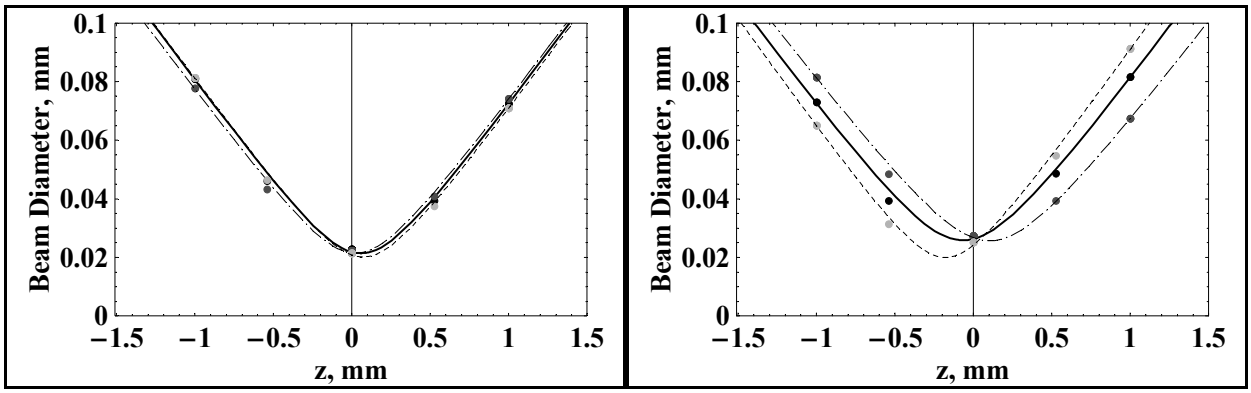

Figure 3.3. Dependence of beam diameter on position along direction of beam propagation around focal point of a test lens (f = 110 mm) in vertical (left) and horizontal (right) directions. Transmitted beam – dashed; diffracted beam – dot-dashed; combined beam – solid.

Because the angle of incidence and angle of diffraction are equal for Bragg diffraction on un-tilted volume gratings (ones that have grating vector parallel to sample surface), the beam diameter does not change due to diffraction by the grating, therefore diffraction-limited divergence is unchanged. However, divergence of the diffracted beam is increased by 30% in the horizontal plane. It was found that this additional divergence is not caused by grating-induced beam distortion. Additional divergence is acquired due to angular dispersion of the grating, as shown in Fig. 3.4. Modeling shows that a grating with parameters described above has an angular dispersion of about 670 μrad / nm. The bandwidth of the laser is about 100 pm FWHM,

meaning that additional divergence should be on the order of 70 μrad which is approximately 35% of diffraction-limited divergence of a 7-mm diameter beam (~ 200 μrad). This effect was experimentally confirmed by observing the spectrum of the diffracted beam in the far-field (in focal plane of a long-focal-length lens). The central wavelength of the far-field beam spot varies in transverse direction by ~90 pm as the spot is scanned with a pinhole over the spot diameter (between the e^{-2} intensity levels). In other words, the diffracted beam is angularly chirped.

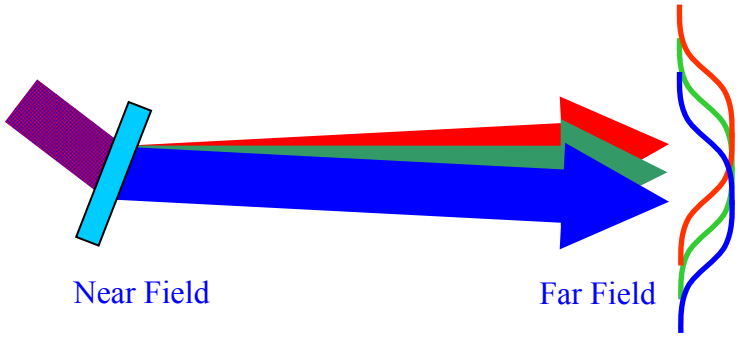

Figure 3.4. Additional far-field divergence acquired by a polychromatic beam due to dispersion of a transmitting volume Bragg grating.

The dispersive component of divergence is diminished when narrow-band sources are used. It was well known that sources with narrow spectral widths are necessary for efficient spectral beam combining in order to maximize diffraction efficiency for the diffracted beam and minimize diffraction efficiency for the transmitted beam. We emphasize that the newly found contribution to beam divergence, arising from angular dispersion, imposes more stringent requirements for spectral widths of sources that can be combined with transmitting volume Bragg gratings.

CHAPTER FOUR: SPECTRAL BEAM COMBINING WITH REFLECTING VOLUME BRAGG GRATINGS

Serial Combining in Linear Geometry

Three SBC systems with varying spectral separation of channels have been designed and assembled. Each system spectrally combines five beams with offset wavelengths into a single near-diffraction-limited beam by a stack of reflecting VBGs. The parameters of gratings used and the absolute efficiency of the 5-channel SBC systems which were achieved experimentally are summarized in Table 4.1. As an example, spectral selectivity of one of the gratings used for SBC with channel separation of 0.43 nm around 1064 nm is shown in Fig. 4.1. Bragg condition of this grating is satisfied for λ_0=1064.0 nm when angle of incidence is ~ 3.8° relative to the grating vector. This grating provides diffraction efficiency of 99.7% at Bragg condition and diffraction losses < 1% for a beam with wavelength offset by 0.43 nm (corresponding to the fourth minimum of the selectivity curve).

Optical layout and photographs of one of the 5-channel SBC systems with a set of VBGs having the same period are shown in Fig. 4.2. The gratings are angle-tuned to diffract beams of respective wavelengths, while the beams with other wavelengths are transmitted undisturbed. Alternatively, if gratings with offset periods are used, angles of incidence of all beams can be made the same.

Table 4.1. Parameters of gratings optimized for SBC experiments.

5-channel SBC system		**Parameters of beam-combining gratings**		
Wavelength / channel separation, nm	Absolute system efficiency (experiment), %	Bragg wavelength at normal incidence, nm	Thickness, mm	Refractive index modulation, ppm
1064 / 0.43	93.7	1065.1	3.7	420
1550 / 0.51	92.6	1552.8	6.5	200
1550 / 0.25	91.7	1550.1	10.3	140

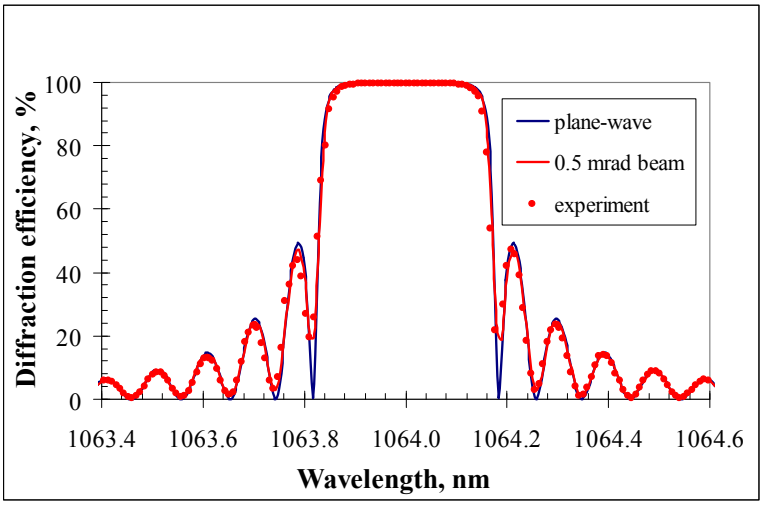

Figure 4.1. Spectral selectivity of a reflecting VBGs used for 5-channel SBC with 0.43 nm channel spacing around 1064 nm.

Commercially available narrow-line fiber-pigtailed diode lasers terminated by high-quality adjustable collimators are used in the experiments, producing near-diffraction-limited (M^2<1.1) beams with 3 mm diameter ($FWe^{-2}M$). Proper collimation is achieved by using a wedge-plate shearing interferometer and by minimizing beam spot size in a focal plane of a focusing lens. The angular divergence of beams is 0.5 mrad and 0.7 mrad ($FWe^{-2}M$) for 1064 nm and 1550 nm cases respectively. The output power of all lasers is set to 5 mW. Central wavelengths of input channels are offset by 0.43 nm (around 1064 nm), 0.5 nm and 0.25 nm (around 1550 nm). The output of each 5-channel SBC system is a spectrally-combined beam with total bandwidth of 1.7 nm (around 1064 nm), 2 nm and 1 nm (around 1550 nm). Spectra of

output beams of the three SBC systems are shown in Fig. 4.3, where individual linewidths are limited by resolution of an optical spectrum analyzer.

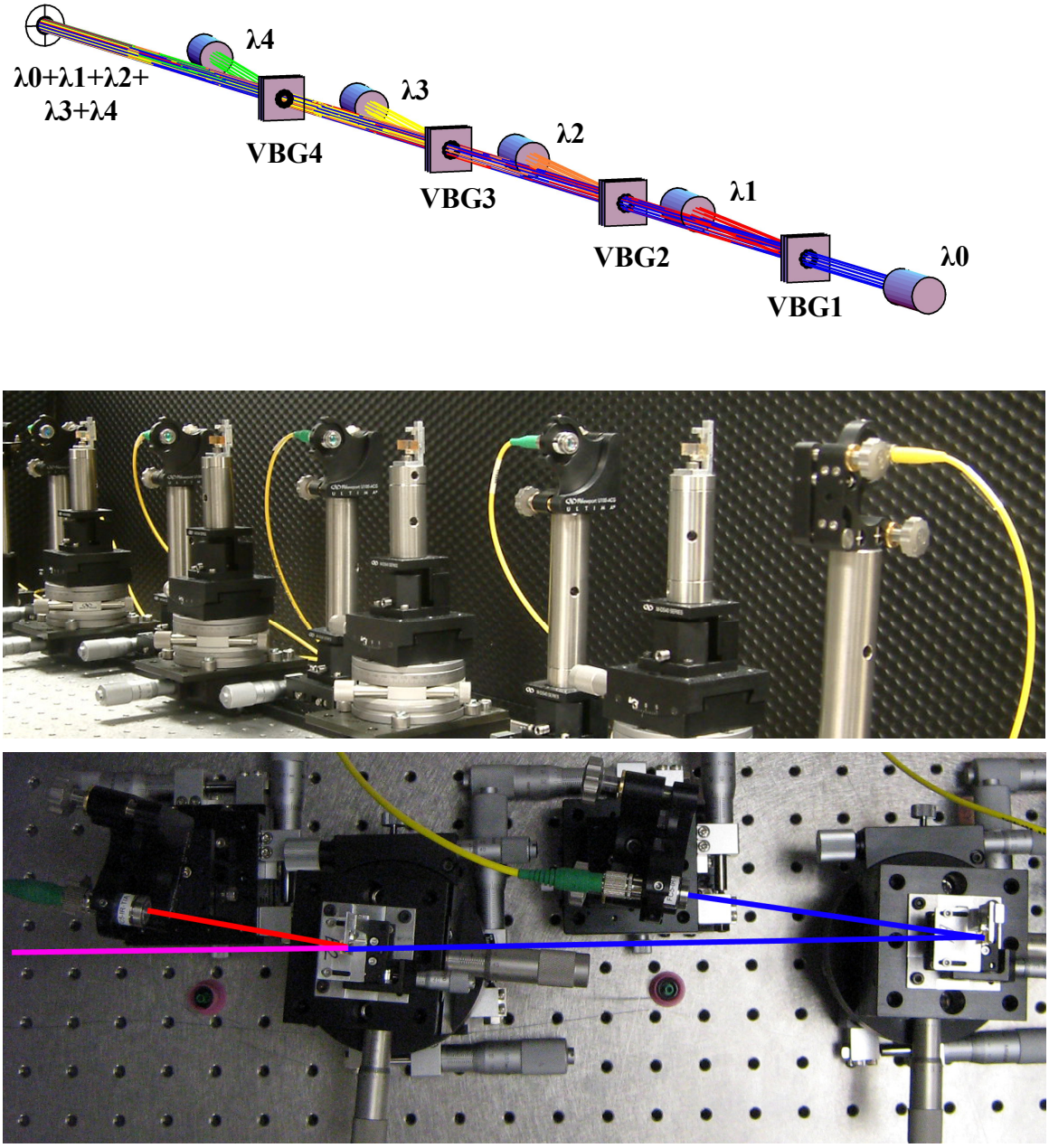

Figure 4.2. Optical layout (top) and a photograph (middle) of spectral beam combining of five laser sources using a stack of identical reflecting volume Bragg gratings. Top view of 2 of the channels (bottom).

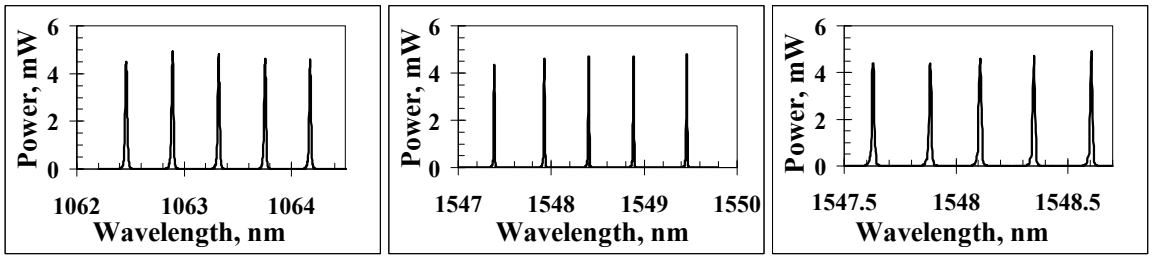

Figure 4.3. Output spectra of three SBC systems using reflecting VBGs.

Alignment of the SBC systems is performed by using an alignment collimator pointing in a reverse direction that defines the axis of the output beam. The channels are aligned sequentially, starting with one that is closer to the output and ending with one that is transmitted through all gratings. The laser source of respective channel is connected to the alignment collimator and a VBG corresponding to that channel is aligned to satisfy the Bragg condition for that wavelength (the beam is diffracted with high efficiency). Next, a working collimator is placed in a location where the alignment beam is diffracted to and output of the laser is switched to the working collimator. The working collimator is aligned to couple light diffracted by the VBG into the alignment collimator with maximum efficiency. As this procedure is repeated to align next channel, the beam is transmitted through the VBGs of previous channels due to offset wavelength. After all channels are aligned, output beams from all channels are overlapped and collinear, resulting in a near-diffraction-limited spectrally-combined beam. This method allows aligning beams with accuracy better than 10-20 μrad.

Times-diffraction-limit factors, commonly known as M^2 of spectrally-combined output beams, are measured by focusing beams with an appropriate test lens. A slit-based beam profiler is used to scan beams in 5 planes along the direction of propagation. Beam widths calculated by second moment definition are fit to a hyperbolic equation to find M^2 of the beams. The results of these measurements are summarized in Fig. 4.4.

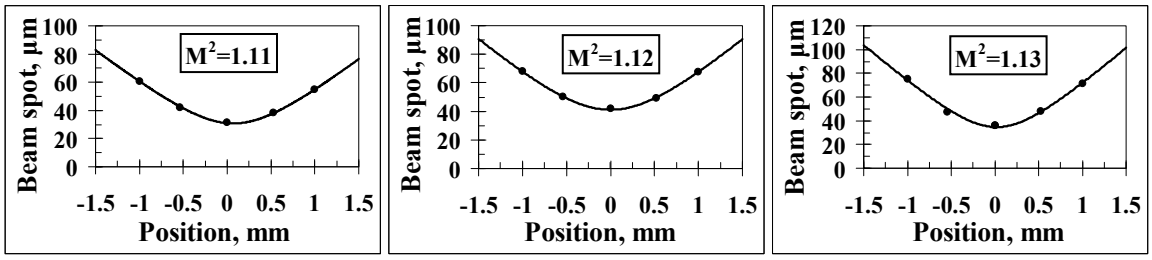

Figure 4.4. Spectrally combined output beams from three SBC systems around focal point of a test lens: 0.43 nm channel separation around 1064 nm (left), 0.51 nm channel separation around 1550 nm (center) and 0.25 nm channel separation around 1550 nm (right).

Spectrally-combined output beams from three SBC systems are near-diffraction-limited with roughly the same M^2 as input beams. This indicates that the accuracy of alignment is much better than the divergence of beams and combining elements do not introduce beam distortions. Brightness of output beams is enhanced by ~ 5 times compared to individual input beams.

Parallel Combining Using a Monolithic 3D Module

In the previous section we described three table-top setups for spectral beam combining of lasers with small spectral separation using reflecting volume Bragg gratings. These setups are based on a linear geometry of combining and have total length of 1-1.5 meters. Successful demonstrations of these SBC setups open up a new direction of engineering – the development of compact modules for multi-channel spectral beam combining. Such modules can become building blocks for a system combining a very large number of channels. They would be based on multiple tilted volume Bragg gratings recorded in single PTR-blank, capable of combining multiple channels simultaneously in a 3-D geometry. This design allows the reduction of beam combiner size by an order of magnitude. A prototype of 4-channel high-spectral-density beam

combiner with actual size 18x7x6 cm^3 and performance similar to linear table-top SBC systems has been developed (Fig. 4.5).

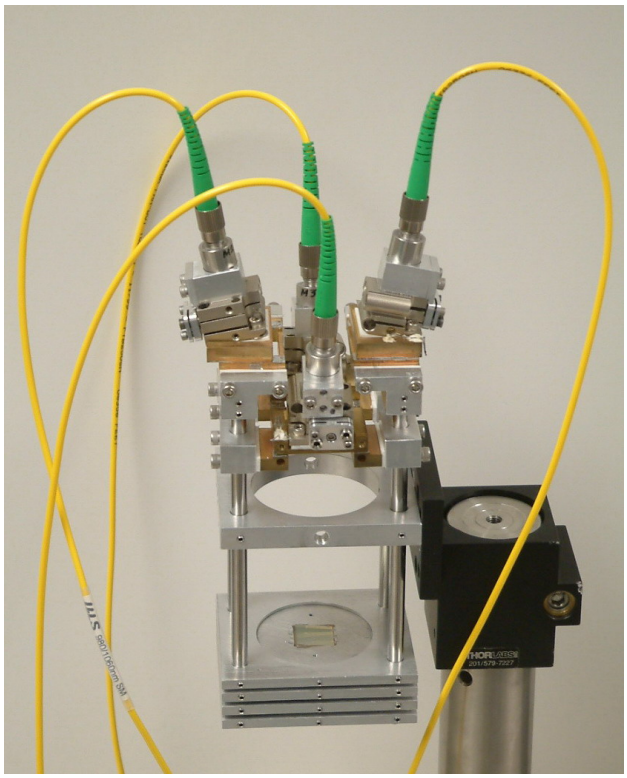

Figure 4.5. Multi-channel monolithic high-spectral-density beam combiner.

The schematic view of a 4-channel beam combiner is shown on Fig. 4.6. In this construction, output fiber collimators (#1 on Fig. 4.6) of fiber coupled laser sources are located symmetrically in the same plane around main optical axis of the system. Collimated laser beams (#3-6 on Fig. 4.6) with shifted wavelengths illuminate a stack of 4 tilted volume Bragg gratings (#2 on Fig. 4.6). The tilt angle and period of each grating in the stack is chosen in such way that each grating diffracts a corresponding laser beam with desirable wavelength. Upon diffraction, the beam propagates in the opposite direction, along the main optical axis of the system. Fine tuning of grating angle and incident beam wavelength for each channel allows for a minimizing of system losses and cross-talk between neighboring channels during the final alignment

procedure. Conceptually, this considered optical scheme is not different from the linear table-top scheme described in the previous section. However, it allows for reducing the size of the setup by 8 times and offers increased mechanical stability of a monolithic construction.

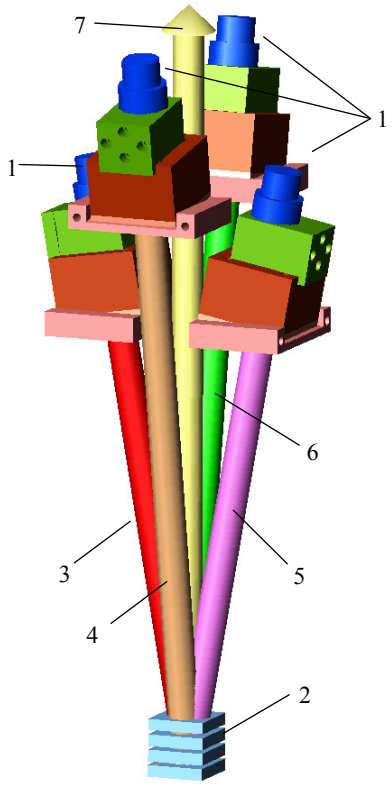

Figure 4.6. Schematic view of a compact monolithic 4-channels spectral beam combiner: 1 – fiber collimators, 2 – stack of tilted reflective VBGs, 3-6 – collimated lasers beams with shifted wavelengths, 7 – combined output beam (main optical axis of the system).

The alignment procedure of a monolithic spectral beam combiner has significant limitations in comparison with the alignment of the previously described table-top version of SBC. First of all, stacking of volume Bragg gratings imposes limitations on the range of angle tuning of grating. Gratings have to be recorded with high accuracy of tilt angle and precisely fixed in a desirable location. Secondly, mechanical stages cannot be used for the proper positioning of fiber collimators in XY-plane due to small size of the SBC head and requirements

for compactness and light weight. Nevertheless, the accuracy of positioning in this plane better than 20 μm has to be achieved in order to obtain proper overlapping of output beams and avoid deterioration of beam quality of the spectrally-combined output beam. A special fixture for positioning of collimators was developed. It is mounted to the beam combiner frame using an In-based alloy with a low melting point (118 °C) and has slots for a removable compact resistive heater. After the fixture is heated to 125-130 °C, the alignment of fiber collimators in XY-plane can be performed using external high-precision translation stages. After alignment is finished, the heater is removed from its slots and external translation stages are disconnected from the fixture. The proper design of the fixture provides its main expansion/compression along the Z-axis, which does not influence alignment precision. Experimental results show that alignment precision using this procedure is sufficient and no additional alignment of collimators is required after cooling.

The following procedure for alignment of a monolithic spectral beam combiner has been developed. Initially, alignment collimator (#2 on Fig. 4.7) is aligned and fixed pointing down an axis that goes through the center of combining module (#1 on Fig. 4.7). This axis defines the future optical axis of spectrally-combined output beam. The alignment collimator is not moved for the rest of the procedure. Fiber collimators for each channel are collimated and located in initial positions on the frame of the SBC head. Next, the fiber-coupled laser source of 1st spectral channel is connected to the input of alignment collimator. The fiber connected to the 1st channel collimator is connected with a high-sensitivity fiber-coupled photodiode. Grating for the 1st spectral channel is mounted on a vacuum holder with an internal photodiode (#4 on Fig. 4.7) and is positioned in a desired location within the SBC head. The grating diffracts the beam coming from the alignment collimator toward the 1st channel collimator.

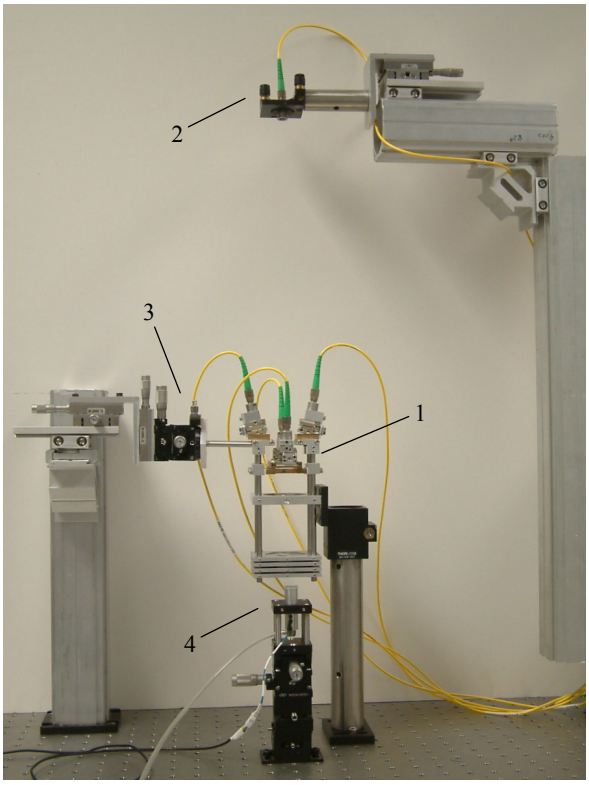

Figure 4.7. Common view of experimental setup for alignment of a 4-channel monolithic beam combiner. 1 – SBC module head; 2 – alignment collimator sets optical axis of SBC head (common direction for output beams); 3 – external precision translation stages for alignment of fiber collimator fixture in XY-plane; 4 – vacuum holder and precision stages for final alignment of beam-combining gratings.

The grating is angularly adjusted to satisfy Bragg condition and achieve maximum diffraction efficiency by minimizing the signal from a photodiode located under the grating. After this, the grating is fixed in the VBG stack holder using UV-cured optical adhesive. Next, the 1st channel collimator is angularly adjusted to achieve good coupling by maximizing the signal from the photodiode that it is connected to. Then, the fiber-coupled laser source of the 1st spectral channel is connected to the input of the 1st channel collimator, while the output of alignment collimator is connected to the fiber-coupled photodiode. The fixture holding the 1st channel collimator is heated and its position is adjusted to obtaining maximum coupling efficiency of 1st beam into the alignment collimator (#2 on Fig. 4.7) after it is reflected from the grating. Adjustment for the channel is considered finished when coupling efficiency exceeds 65-70%. Coupling efficiency is

re-checked after collimator fixture has cooled. The same alignment procedure is repeated for the rest of the channels.

For an experimental demonstration of a monolithic SBC system, four reflecting VBGs with tilted grating vectors were recorded in PTR glass. These VBGs have grating vectors tilted by ~ 3.4° relative to the surface normal. Bragg wavelengths of these gratings are offset by ~ 0.7 nm, ranging from 1063.9 to 1066.0 nm for light incident normally to the grating planes. For light incident normally to the surface of the VBGs, resonant wavelengths are shifted by ~ 1.9 nm into the shorter-wavelength side of the spectrum. In this geometry, beams of respective wavelengths are diffracted by the gratings such that Bragg angle in air is ~ 5° (deflection angle is ~170°). The VBGs are rotated by 90° and stacked so that each channel is diffracted by only one of the gratings while it is transmitted through the rest of the gratings.

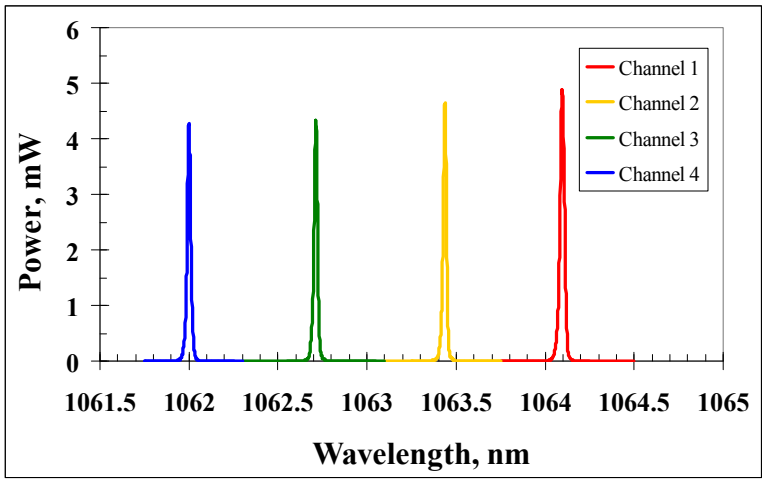

Figure 4.8. Output spectrum of a monolithic spectral beam combiner. Individual linewidths are limited by the resolution of an optical spectrum analyzer.

After proper alignment of the system, beams from each channel are reflected by respective VBGs so that the all beams emerge overlapped and collinear. The spectrum of the near-diffraction-limited output beam consists of a comb of spectral lines corresponding to the wavelengths of individual channels (Fig. 4.8). Absolute efficiency of the monolithic spectral

beam combiner was measured at 90.7%. High combining efficiency of a monolithic SBC module allows it to be used as an elementary cell for further increases of the number of combined channels.

CHAPTER FIVE: NARROW-BAND VOLUME BRAGG GRATINGS UNDER HIGH-POWER LASER RADIATION

Volume Bragg gratings in photo-thermo-refractive glass are extensively used in high-power applications such as spectral beam combining, spectral stabilization of lasers, transverse mode selection, etc. Narrow-band reflecting VBGs are of particular interest in these applications, because spectral selectivity determines the channel density of spectral beam combining or linewidth of a stabilized diode laser. It is important to investigate the behavior of these gratings under high-power laser radiation in order to properly design gratings for high power applications.

VBGs in PTR glass have been shown to withstand a power density of 100 kW/cm^2 [134]. No irreversible changes to PTR glass and VBG were observed after high-power irradiation. At the same time, little attention has been paid to the behavior of the grating while under high-power laser radiation. When VBGs are irradiated by high power laser beams, even a small residual absorption of PTR glass can cause heating which results in thermal expansion and leads to a shift of Bragg wavelength. The Bragg wavelength of a "hot" grating is shifted into the red part of the spectrum. In this section, we present a set of experiments aimed at understanding the amount of this shift as well as possible grating distortion when under high power radiation.

A narrow-band reflecting VBG with thickness t = 2.5 mm, refractive index modulation Δn = 340 ppm and resonant wavelength λ_0=1074 nm at normal incidence has been recorded in PTR glass. A tunable diode laser coupled with a high-quality collimator is used for spectral scanning of the grating. The grating is angle-tuned so the Bragg condition is satisfied for the

scanning beam at 1070 nm in the absence of high-power radiation. The spectral profile of diffraction efficiency is obtained by tuning the wavelength of the test beam. Peak diffraction efficiency of the grating is 96.6%.

100-W single-transverse-mode Ytterbium fiber laser with spectrum centered at 1096 nm is used to irradiate the sample non-resonantly. Collimated beam diameter of 5 mm results in 0.5 kW/cm^2 power density on the grating. The high-power beam is overlapped with the scanning beam at the grating. A focusing lens with long focal length is used to change beam power density at the grating. After the lens, the beam spot at the grating is reduced to 1.6 mm, resulting in 5 kW/cm^2 power density. This setup is illustrated in Fig. 5.1.

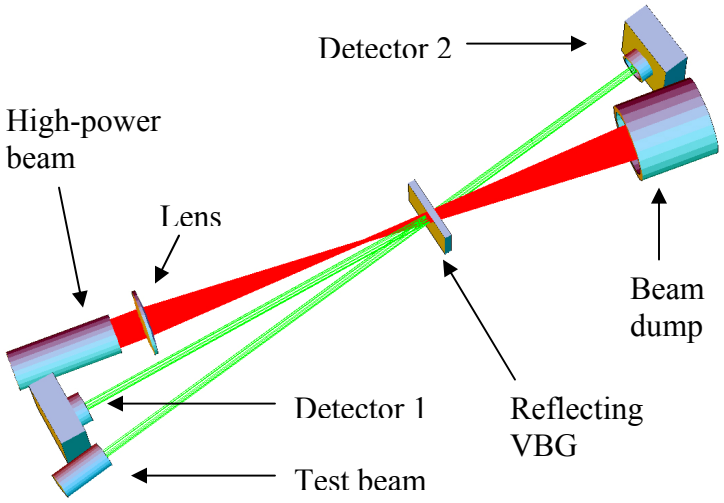

Figure 5.1. Optical setup used for testing behavior of a narrow-band reflecting VBG under high-power irradiation of 100 W with 0.5 kW/cm^2 power density on the grating.

When the high-power beam is incident on the grating, resonant wavelength of the grating is shifted into the red part of the spectrum due to heating. A steady-state is reached within a few minutes for both 0.5 kW/cm^2 and 5 kW/cm^2 power densities. The amount of thermal shift is 56 pm for 0.5 kW/cm^2 power density and 95 pm for 5 kW/cm^2 power density (Fig. 5.2). Peak diffraction efficiency of the grating is almost unchanged under irradiation with 0.5 kW/cm^2

power density (96.6%) and 5 kW/cm^2 power density (96.4%), indicating no grating distortion due to non-uniform temperature distribution across the grating aperture.

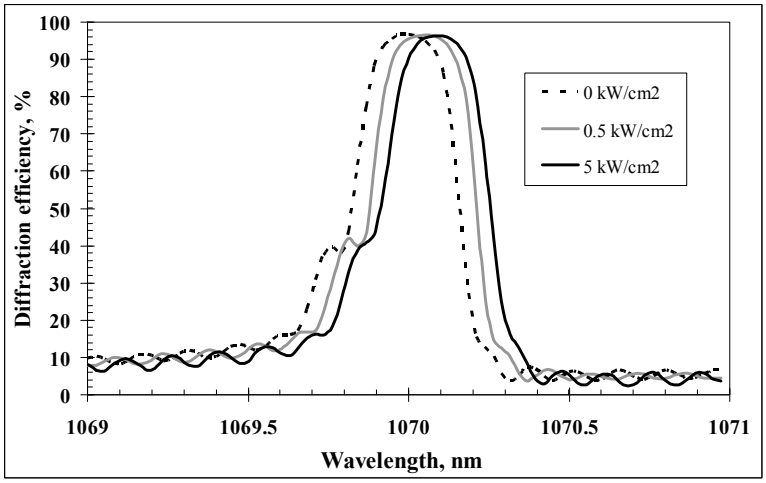

Figure 5.2. Spectral selectivity of a reflecting VBG under 100 W high-power radiation at 1096 nm for different power density on the grating.

When high-power operation of grating is desired, the thermal shift of resonant wavelength can be compensated by pre-tuning the source wavelength or angle of incidence on the grating. Fig. 5.3 shows diffraction efficiency of a grating as a function of time after high power radiation is turned on. The grating is pre-tuned for high-power operation by angular adjustment. Although diffraction efficiency is 91.3% (pre-adjusted for 0.5 kW/cm^2 power density) and 87.9% (pre-adjusted for 5 kW/cm^2 power density) in the absence of high-power radiation, it is rapidly restored once the high power beam is introduced. After reaching steady-state within 3 minutes, diffraction efficiency is roughly the same as the maximum diffraction efficiency in the absence of high-power radiation: 96.6% for 0.5 kW/cm^2 power density and 96.3% for 5 kW/cm^2 power density.

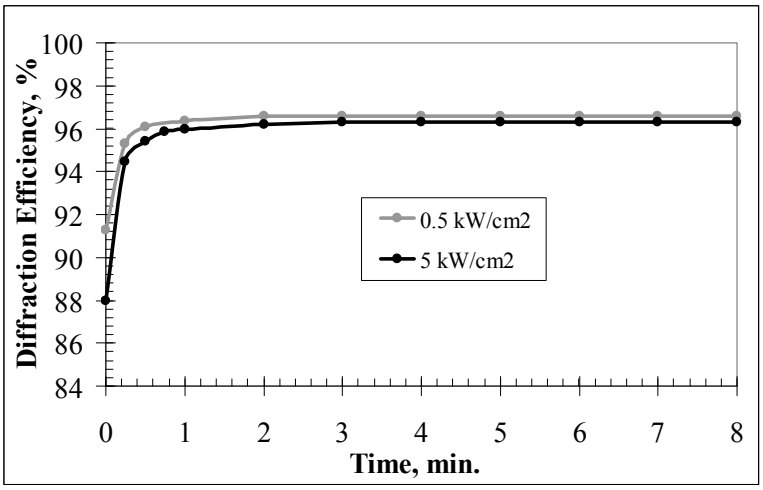

Figure 5.3. Temporal evolution of diffraction efficiency of a reflecting VBG in high-power radiation at 1096 nm (grating is pre-tuned for high-power operation by angular adjustment).

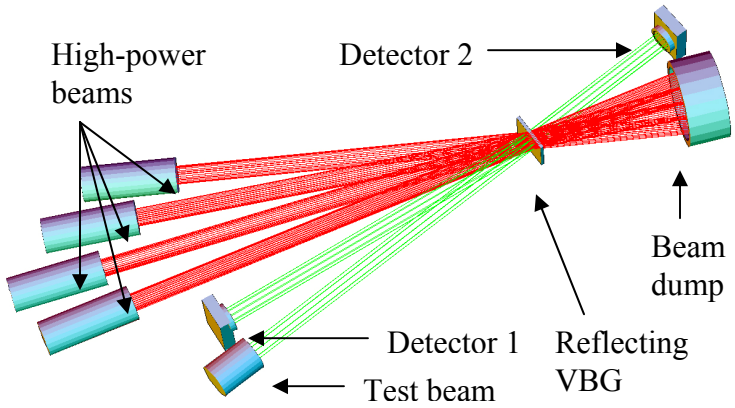

Figure 5.4. Optical setup used for testing behavior of a narrow-band reflecting VBG under high-power irradiation of 570 W with 2 kW/cm^2 power density on the grating.

In a similar experiment, the behavior of a narrow-band reflecting VBG with 20×20 mm aperture and 280 pm FWHM spectral selectivity has been studied. The grating is specifically designed for spectral beam combining of high-power beams around 1064 nm with 0.45 nm channel separation (spectral distance between peak and third minimum of spectral selectivity is 0.45 nm). The grating is non-resonantly irradiated by four fiber lasers with maximum CW power of 150 W each around 1064 nm (Fig. 5.4). Beam diameters of the high-power beams and

the wavelength-tunable test beam were ~ 6 mm ($FWe^{-2}M$). All beams are overlapped at the grating.

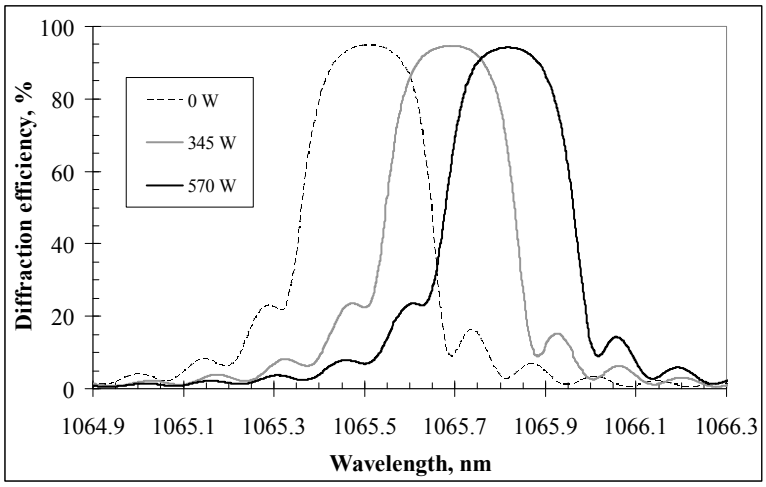

Figure 5.5. Spectral selectivity of a narrow-band reflecting VBG under high-power radiation up to 570 W around 1064 nm.

The behavior of spectral selectivity of the VBG under high-power radiation is shown in Fig. 5.5. The main effect of high-power radiation is long-wavelength-shifting of the resonant wavelength of the grating, while peak efficiency is almost unchanged (~ 0.5% drop at maximum power). Because resonant wavelength of VBGs can be angle-tuned, this shift can be easily accounted for and compensated by pre-tuning the grating for high-power operation. It can be seen from Fig. 5.6 that when VBG is pre-tuned for high-power operation, peak diffraction efficiency is restored within 15-20 minutes after high-power radiation is turned on. Once peak efficiency is reached, it is virtually unchanged for the rest of operation.

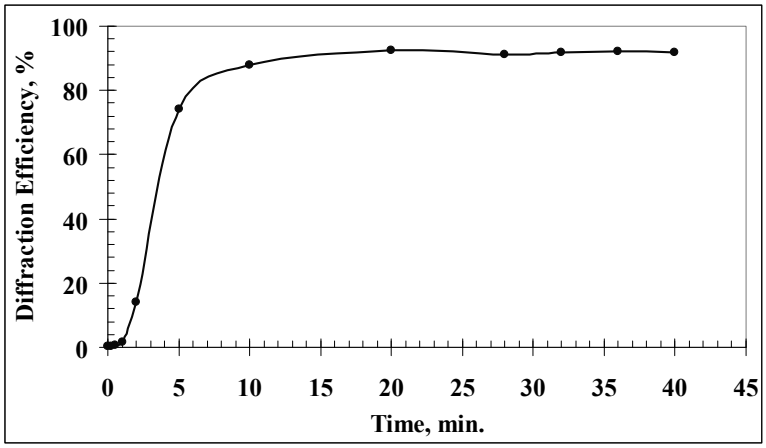

Figure 5.6. Temporal evolution of diffraction efficiency of a narrow-band reflecting VBG under 570 W of CW radiation around 1064 nm (grating is pre-tuned for high-power operation by angular adjustment).

In order to investigate grating-induced beam distortions of narrow-band VBGs under resonant high-power radiation, the same VBG is used for spectral beam combining of two fiber lasers with high channel density. Fiber lasers terminated by collimators produce unpolarized near-diffraction-limited beams 6 mm in diameter ($FWe^{-2}M$) with maximum CW power of ~ 160 W. Wavelengths of the lasers are offset by 0.45 nm. The beam with λ_1=1064.8 nm is transmitted through the grating undisturbed while the beam with λ_1=1064.35 nm, incident on the grating from the opposite side, is diffracted by the grating. The two beams were overlapped and collinear after the grating resulting in near-diffraction-limited spectrally-combined output beam. A high-quality low-power test beam is overlapped with the high-power beams on the grating. The test beam is diffracted by the grating and steered to a scanning beam profiler for analysis of grating-induced beam distortions (Fig. 5.7).

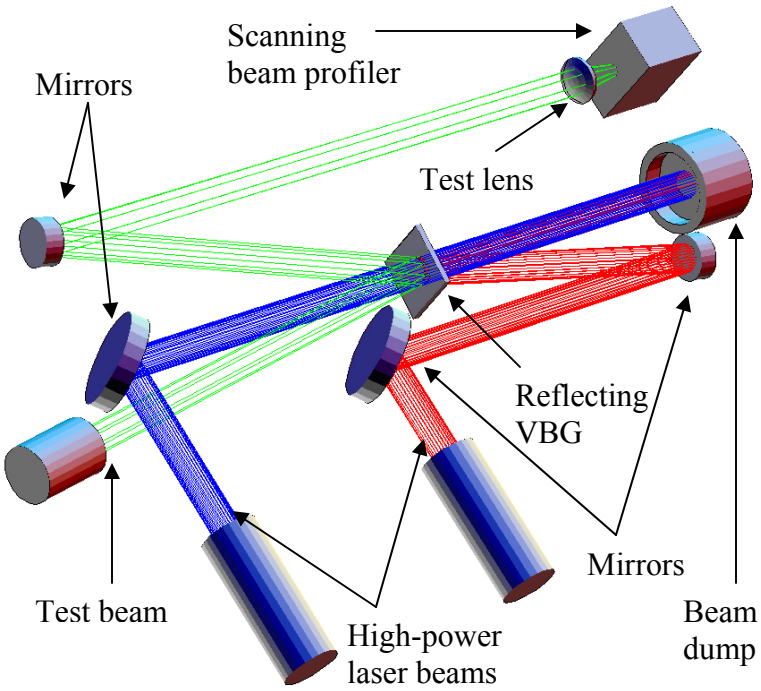

Figure 5.7. Optical setup for spectral beam combining of two high-power lasers with output power 305 W. A high-quality low-power test beam is used for analysis of grating-induced beam distortions when grating is under high power radiation.

Absolute efficiency of spectral beam combining of two fiber lasers of 95.9% was achieved. Efficiency was identical for low-power (25 W combined output) and high-power operation (305 W combined output), indicating no significant distortion of the grating under high power. Absence of grating distortion was validated by measuring beam quality of a test beam diffracted off the grating while under high power. M^2 of the diffracted test beam was 1.15 in two orthogonal directions for combined beam power of 305 W (Fig. 5.8), 25 W and stand-alone unloaded grating.

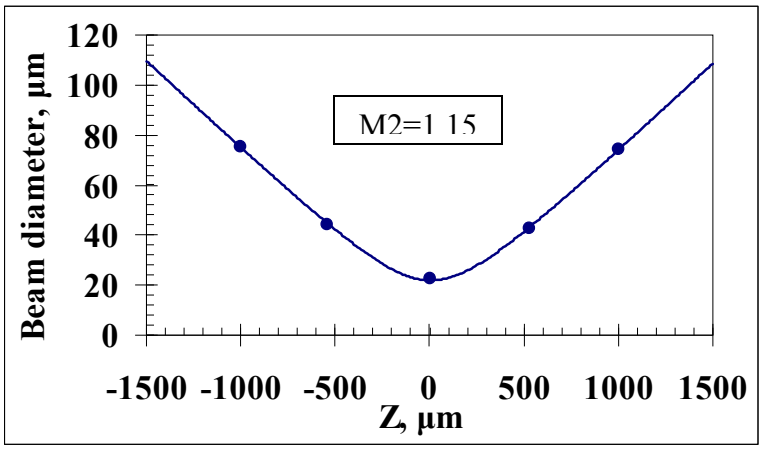

Figure 5.8. Beam quality measurement of a test beam diffracted by a reflecting VBG that is combining two high-power beams into a single near-diffraction-limited beam with 305 W output power.

The SBC system producing 305 W spectrally-combined output beam exhibited excellent stability. No temporal drift of combined beam power was observed over many hours of operation. Over the course of a few weeks, the SBC system was run multiple times, producing identical performances each time without any additional alignment.

This investigation of behavior of narrow-band reflecting VBGs under high power radiation has produced the following results. It was found that there is no significant grating distortion or deterioration of diffraction efficiency, spectral selectivity and other properties of VBGs under 100 W CW radiation with 0.5 kW/cm^2 and 5 kW/cm^2 power densities and 570 W CW radiation with 2 kW/cm^2 power density. It was shown that the Bragg wavelength is shifted to longer wavelengths under high-power radiation due to thermal expansion of PTR glass. The amount of shift can be pre-determined and compensated during grating fabrication or alignment. Spectral beam combining of two fiber lasers with 0.45 nm channel separation using volume Bragg gratings is demonstrated with 95.9% efficiency. It is shown that there is no performance deterioration or grating distortion at 305 W power in combined near-diffraction-limited beam.

CHAPTER SIX: FIBER LASER SYSTEM WITH KW-LEVEL SPECTRALLY-COMBINED OUTPUT

In this chapter experimental demonstration of a multi-channel fiber laser system with kW-level spectrally-combined output is discussed. Experimental setup of SBC laser system is shown in Fig. 6.1 and a photograph of assembled system is shown in Fig. 6.2. Output of each fiber laser is terminated by collimator/isolator assembly that is mounted on the optical table. High power beams are steered onto respective gratings by double-mirror assemblies. System output is captured by a water-cooled detector or beam dump.

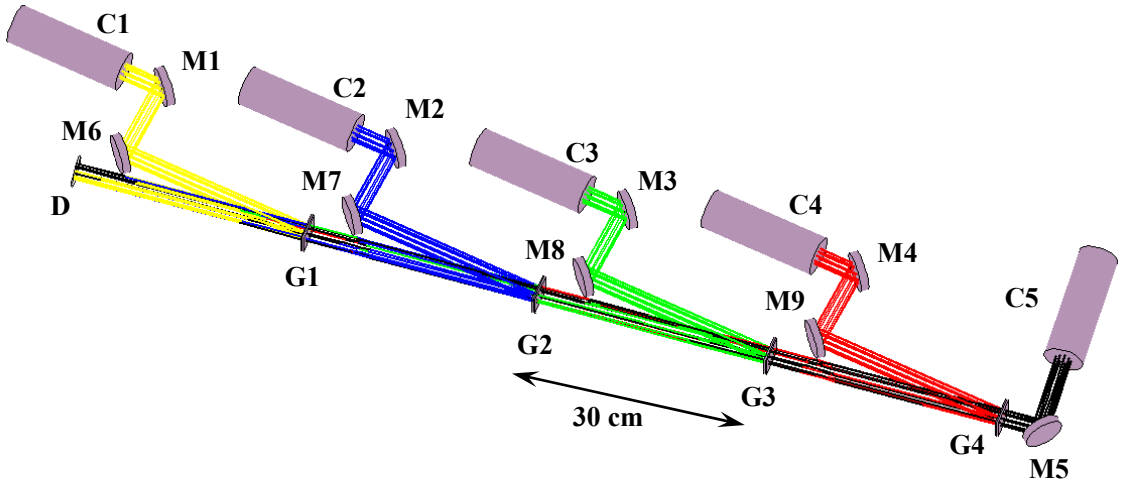

Figure 6.1. Experimental setup of a fiber laser system with kW-level spectrally-combined output. Five fiber lasers with offset wavelengths are combined using reflecting VBGs. C1-5: fiber laser collimators; M1-9: steering mirrors; G1-4: reflecting VBGs; D: detector or beam dump.

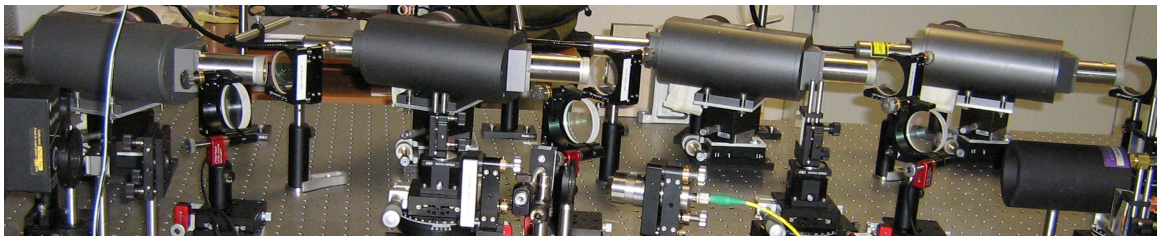

Figure 6.2. Photograph of a table-top fiber laser system with kW-level spectrally-combined output.

In this setup, five commercially-available Yb-doped fiber lasers (IPG Photonics model YLR-150-SF) have been spectrally combined into a single near-diffraction-limited beam using narrow-band reflecting volume Bragg gratings. Each laser provides randomly polarized beam with 6 mm diameter and CW power ~ 160 W. Source wavelengths are offset by ~ 0.5 nm around 1064 nm such that output spectrum occupies 2-nm bandwidth and consists of 5 equally-spaced lines (Fig. 6.3). Maximum output power of the system in a combined beam is 773 W and absolute system efficiency is 91.7%.

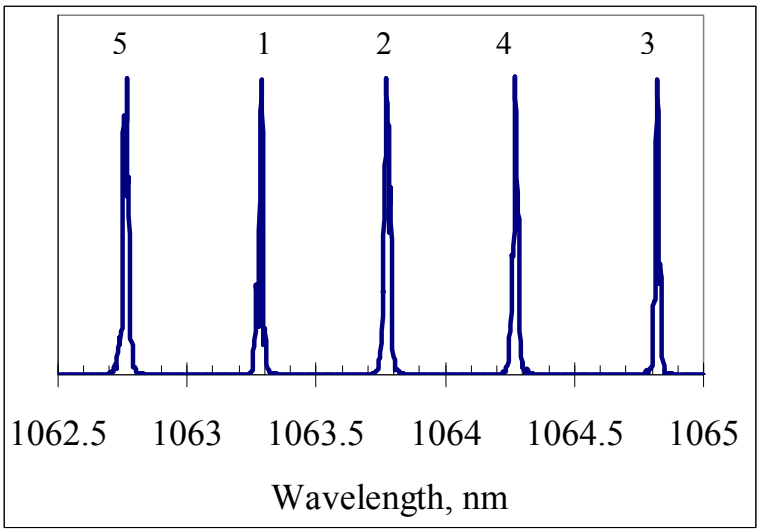

Figure 6.3. Spectrum of a spectrally-combined output beam with total power of 773 W. Respective channel number is noted.

Four narrow-band reflecting VBGs with clear aperture up to 20 mm (manufactured at OptiGrate) are used in this experiment. Gratings are designed to provide optimum system

efficiency – grating thickness 3.5 mm, refractive index modulation 300 ppm (3×10^{-4}). Period of each grating has been selected to match Bragg condition for wavelength of each laser at angle of incidence between 5-7°. Grating properties important for high-power spectral beam combining have been measured and are summarized in Table 6.1 for the four gratings used.

Table 6.1. Basic properties of gratings used in high-power SBC system.

VBG #	G1	G2	G3	G4
Max efficiency (7 mm beam), %	99.0	97.7	99.6	99.4
Material losses, %	1.3	1.2	1.4	1.3
Material losses, cm^{-1}	$1.6\cdot10^{-2}$	$2.0\cdot10^{-2}$	$1.8\cdot10^{-2}$	$1.5\cdot10^{-3}$
Absorption, cm^{-1}	$1.5\cdot10^{-3}$	$1.1\cdot10^{-3}$	$1.4\cdot10^{-3}$	$1.7\cdot10^{-3}$
Bragg wavelength at normal inc., nm	1065.39	1065.36	1066.62	1067.01
Bragg wavelength shift @ 150 W, pm	186	134	216	190
Channel wavelength, nm	1063.26	1063.77	1064.81	1064.28
Low-power Bragg angle, degree	5.4	4.6	4.9	6.0
Alignment wavelength, nm	1062.40	1063.25	1064.16	1063.90
High-power Bragg angle, degree	6.4	5.3	5.6	6.5

Spectral selectivity curves of these gratings are shown in Figs. 6.4, 6.5, 6.6, and 6.7 for different apertures of scanning beam. It can be seen from these figures that peak efficiency is about the same for beams with diameter of 6 and 15 mm and is slightly lower for a beam with 1 mm diameter. This decrease is due to finite angular selectivity of VBGs, which becomes significant for beams with far-field divergence higher then a few hundred μrad. This effect was theoretically described and analyzed earlier in this thesis. It is observed even for perfect gratings and high-quality Gaussian beams.

Fig. 6.8 compares spectral selectivity shown in Fig. 6.7 with a theoretical plane-wave efficiency curve. Bragg wavelength of this grating is 1067 nm at normal incidence and 1063 nm at angle of incidence ~ 7.3°. Small difference between the measured spectral selectivity and

theoretical plane-wave profile is due to finite beam divergence and grating vector non-uniformity across the aperture.

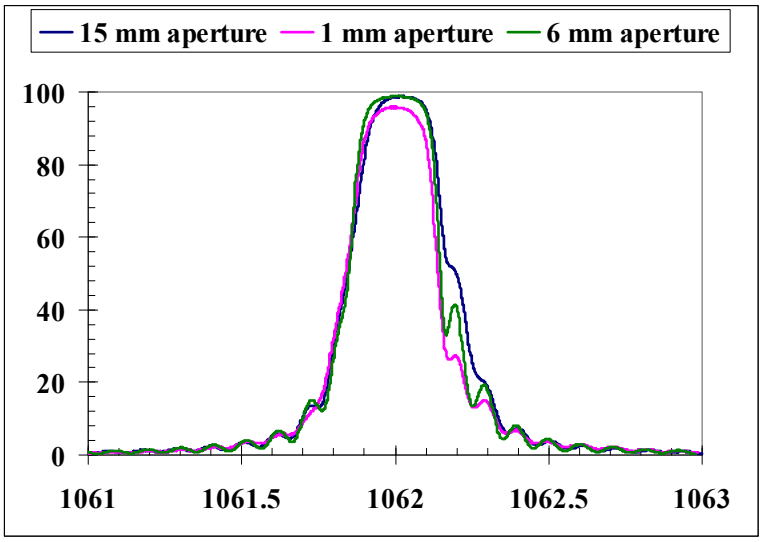

Figure 6.4. Spectral dependence of diffraction efficiency of a large-aperture narrow-band VBG used for dense high-power SBC (grating G1), measured at angle of incidence ~ 6.8° with different beam apertures.

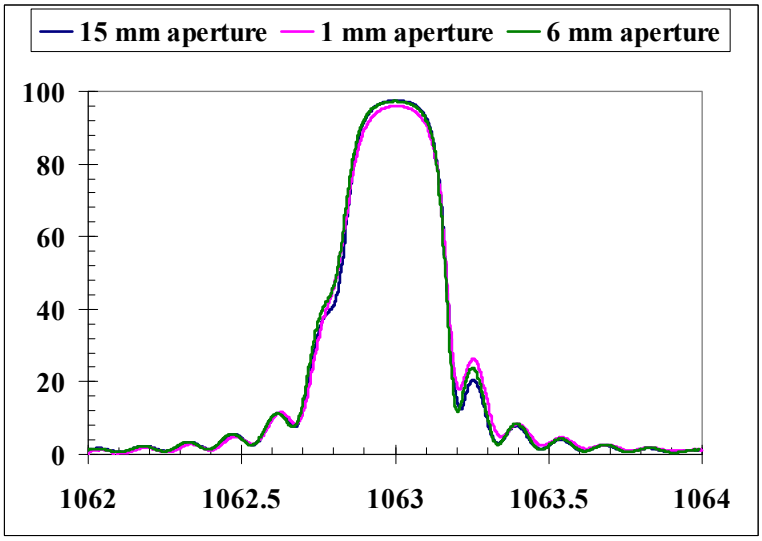

Figure 6.5. Spectral dependence of diffraction efficiency of a large-aperture narrow-band VBG used for dense high-power SBC (grating G2), measured at angle of incidence ~ 5.7° with different beam apertures.

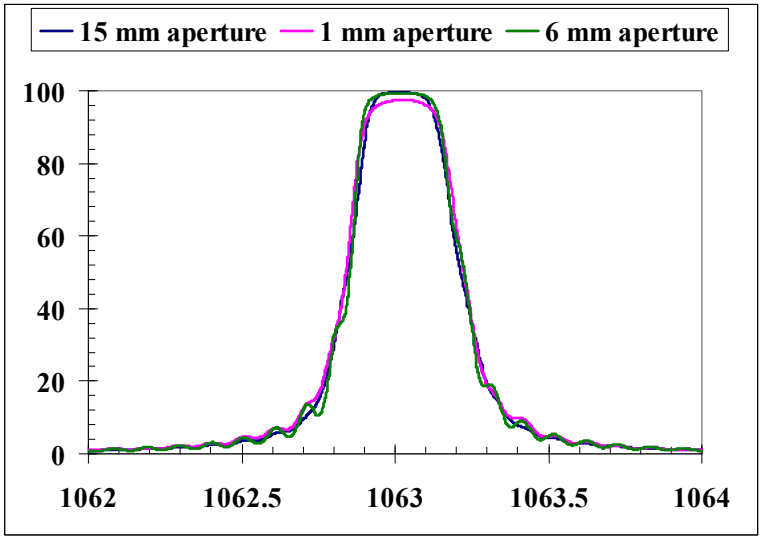

Figure 6.6. Spectral dependence of diffraction efficiency of a large-aperture narrow-band VBG used for dense high-power SBC (grating G3), measured at angle of incidence ~ 6.9° with different beam apertures.

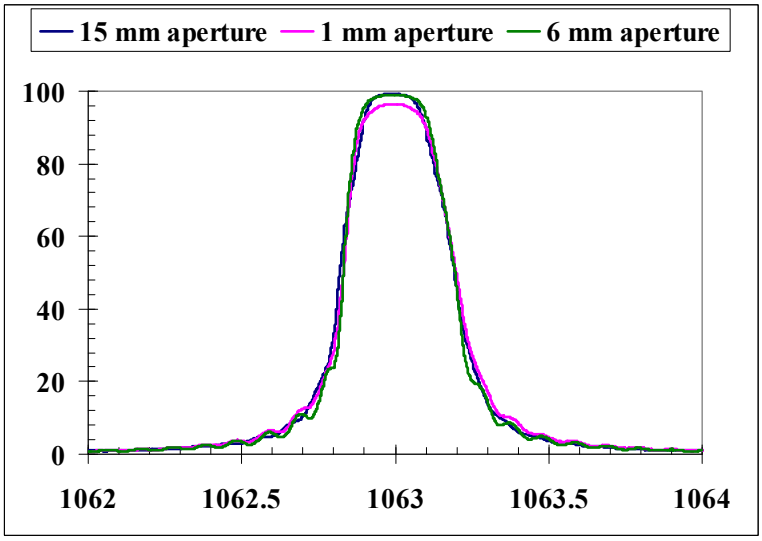

Figure 6.7. Spectral dependence of diffraction efficiency of a large-aperture narrow-band VBG used for dense high-power SBC (grating G4), measured at angle of incidence ~ 7.3° with different beam apertures.

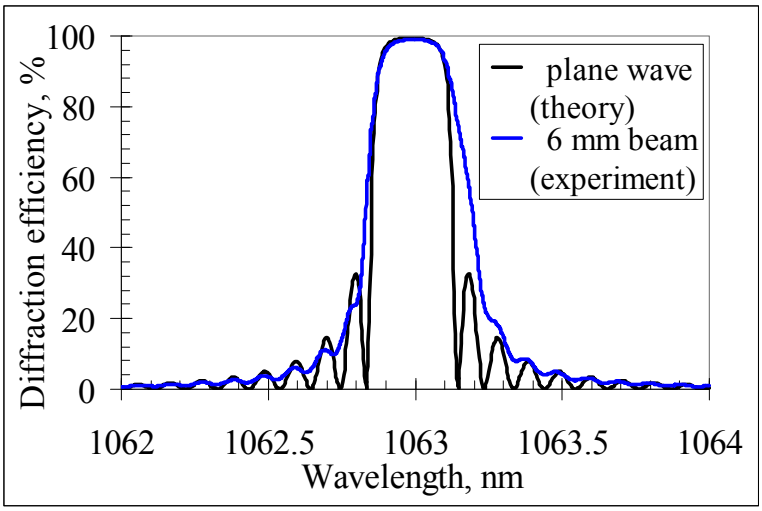

Figure 6.8. Spectral dependence of diffraction efficiency of a large-aperture narrow-band VBG used for dense high-power SBC (grating G4).

SBC gratings are aligned by a tunable diode laser, terminated by a high-quality collimator pointing in reverse direction. Gratings are not intentionally cooled during high-power operation. The system is aligned to compensate for thermal shift of resonant wavelengths of the gratings under high power radiation, following the preliminary test results (Table 6.1). After initial alignment, the system is extremely stable and requires no active adjustment. Diffraction losses at maxima and minima, material losses (scattering and absorption) and reflection from AR coated surfaces are the main contributions to system efficiency deviation from 100%. Absolute system efficiency is unchanged from day to day and during many hours of operation, without system re-alignment. Long-term output power stability is better then 1% at full power, roughly the same as temporal power stability of sources. The system is insensitive to ambient temperature changes on the order of a few degrees.

To exclude an effect of high power beams quality on results of measurements, distortions of gratings in high-power SBC system are studied by measuring propagation properties of a high-quality test beam diffracted by a grating located in a combined beam with total power up to 773 W and corresponding power density of 2.75 kW/cm^2. Test setup is shown in Fig. 6.9.

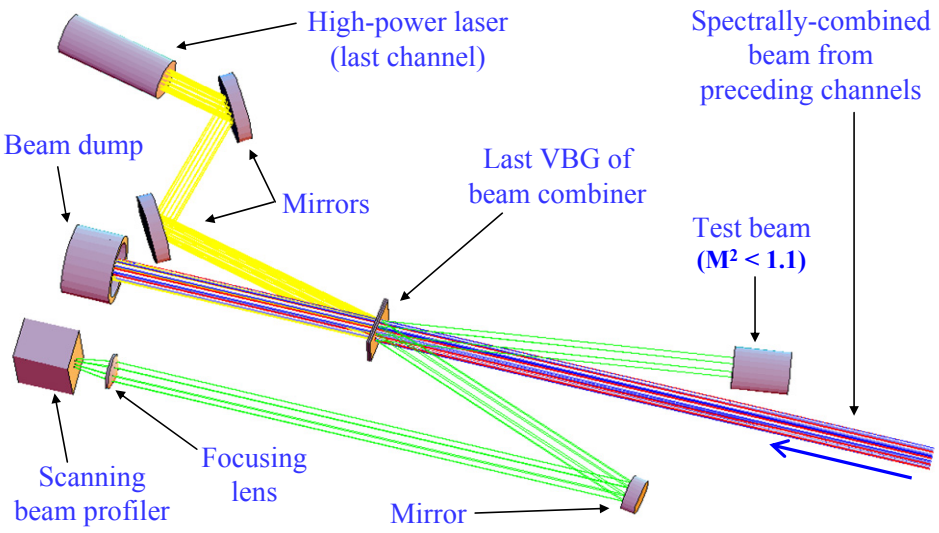

Figure 6.9. Experimental setup for measuring grating-induced beam distortions in a high-power SBC system.

Peak diffraction efficiency and spectral selectivity of the gratings are unchanged under high-power operation. Test beam diffracted by the grating operating in a combined beam with power of 773 W is near-diffraction-limited (Fig. 6.10) with best-fit $M^2 = 1.14$, indicating no significant grating distortion.

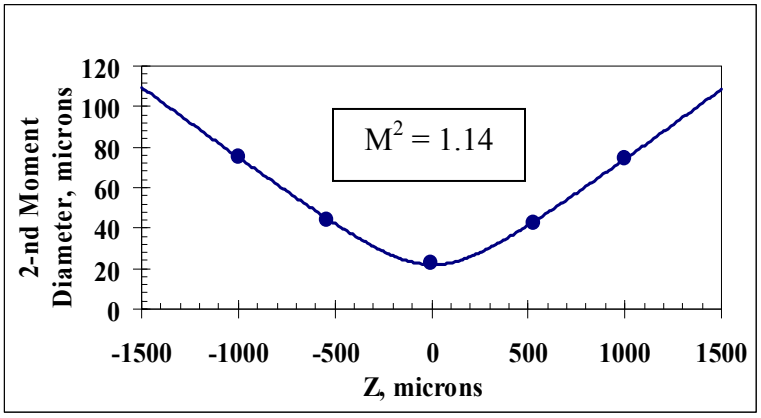

Figure 6.10. Caustic of a test beam around focal point of a test lens. The test beam is diffracted by a VBG operating in a combined beam with total power of 773W.

In this chapter we have demonstrated that laser systems can be efficiently power-scaled by spectral combination of multiple high-power lasers with offset wavelengths. Volume Bragg

gratings recorded in PTR glass are ideal elements for high spectral density beam combining of high-power radiation due to narrow spectral selectivity, low absorption and excellent thermo-mechanical properties. A laser system that combines five randomly polarized fiber lasers with 0.5 nm channel separation around 1064 nm using reflecting VBGs in PTR glass is demonstrated. Output power of the system is 773 W and combining efficiency is 91.7%. It is shown that VBGs introduce no significant beam distortions under high-power operation. The system can be further scaled by increasing the number of channels and/or power per channel.

CHAPTER SEVEN: SPECTRAL CONTROL OF FIBER LASERS USING VOLUME BRAGG GRATINGS

Efficient operation of a high-power SBC system with external VBGs, described in the previous section, requires that thermal equilibrium is not disturbed during operation. Ambient temperature fluctuations of more then a few degrees or failure of one of the channels require re-alignment of the system in order to restore original efficiency. This complication can be avoided if wavelengths of sources can be controlled. In this section we describe a fiber laser system in an external-cavity configuration with a narrow-band VBG for wavelength control. In our experiments we use a diode-pumped Yb-doped photonic crystal fiber with chirped fiber Bragg gratings (FBGs) on both ends. A high-efficiency chirped FBG on one end acts as an end mirror, while a low-efficiency chirped FBG on the other end acts as a weak output coupler in order to prevent fiber damage due to self-pulsing during alignment of external cavity [152]. A high-quality fiber-pigtailed collimator is fused to the output fiber of this laser and an external cavity is created by providing feedback to the laser with an output coupler located normally to the collimated output beam. Output coupler can be replaced with a reflecting VBG (Fig. 7.1), in which case spectral properties of the laser are influenced by the spectral selectivity and alignment of the VBG. Depending on spectral selectivity of the VBG compared to the gain bandwidth of the laser, emission linewidth can be significantly narrowed. In this configuration VBG acts as a spectral selector (determined by the width of spectral selectivity) and an output coupler (determined by diffraction efficiency) simultaneously. In order to achieve spectral

locking of the laser with a VBG, it is important that Bragg wavelength of the VBG is within the gain bandwidth of the fiber laser and the feedback provided by the grating is sufficient to overcome the coupling provided by the internal low-efficiency chirped FBG. Assuming this condition is satisfied and wavelength of the laser is "locked" to the Bragg wavelength of external VBG, such construction provides automatic wavelength adjustment. If Bragg wavelength of VBG is changed due to changes in ambient temperature or heating (for example, through absorption of high power laser radiation), wavelengths of the laser is shifted to automatically satisfy the new Bragg wavelength of the grating, without any additional alignment.

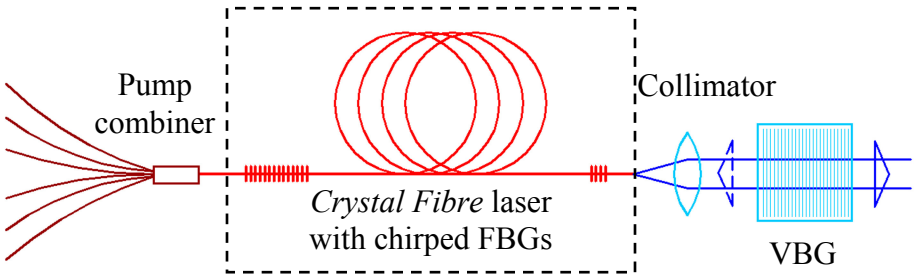

Figure 7.1. Fiber laser in an external cavity configuration with a VBG acting as an output coupler and a spectral selector simultaneously.

Such geometry can be used for spectral narrowing of fiber lasers, but spectral beam combining of such lasers requires additional combining elements, since VBG acts as an output coupler and not as a beam combiner. Moreover, central wavelength of the laser cannot be tuned by rotating the VBG, since feedback provided by the grating will no longer be coupled back into the amplifier. An alternative solution is a slight modification of this configuration (Fig. 7.2). In this scheme a VBG is used at a small angle in a combination with a broadband output coupler. Spectral properties of the laser are still determined by spectral properties of the VBG, but in such arrangement the grating can also act as a beam combiner. Moreover, central wavelength of the laser can be tuned by rotating the grating as shown in Fig. 7.2. In this configuration it is

beneficial to use VBGs with diffraction efficiency close to 100% and select an output coupler with reflectivity sufficient for providing feedback greater than the reflectivity of the internal low-efficiency chirped FBG.

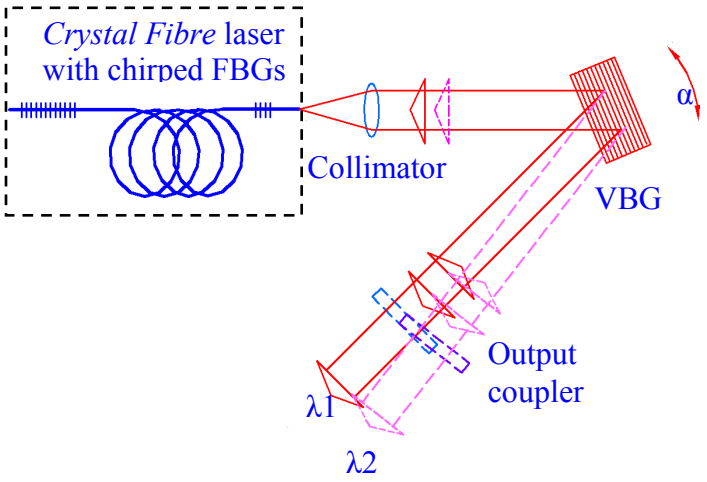

Figure 7.2. Fiber laser in an external cavity configuration with a broad-band output copuler and a VBG used for spectral control and tuning.

Both external-cavity configurations (Fig. 7.1 and Fig. 7.2) have been successfully demonstrated. An external cavity constructed according to Fig. 7.2 uses a reflecting VBG with 99.5% diffraction efficiency and an output coupler with 20% reflectivity. VBG with 3.7 mm thickness, 400 ppm refractive index modulation, and 1065.1 nm Bragg wavelength at normal incidence has spectral selectivity ~ 0.3 nm (FWHM). Spectral dependence of diffraction efficiency is shown in Fig. 7.3, measured at angle of incidence ~ 3.8° relative to the grating vector with a 3-mm diameter beam ($FWe^{-2}M$). Below laser threshold (I_{th}= 0.75 A) superluminescence is observed with bandwidth determined by the reflectivity bandwidth of chirped FBGs (Fig. 7.4, curve 1). Above threshold lasing occurs at 1064.26 nm with 64 pm FWHM linewidth at 6 A pumping current (Fig. 7.4, curve 2). When external cavity with a reflecting VBG and an output coupler is constructed, the low-efficiency FBG is suppressed by a stronger external feedback. In this configuration, laser wavelength is determined by the angle of

VBG and tuning across the 1 nm bandwidth of high-reflecting rear chirped FBG has been demonstrated. Laser linewidth is 46 pm FWHM at 6 A pumping current (Fig. 7.4, curve 3), determined by spectral selectivity of the VBG. Since spectral selectivity of the VBG is quite large, no significant linewidth narrowing occurs in this case.

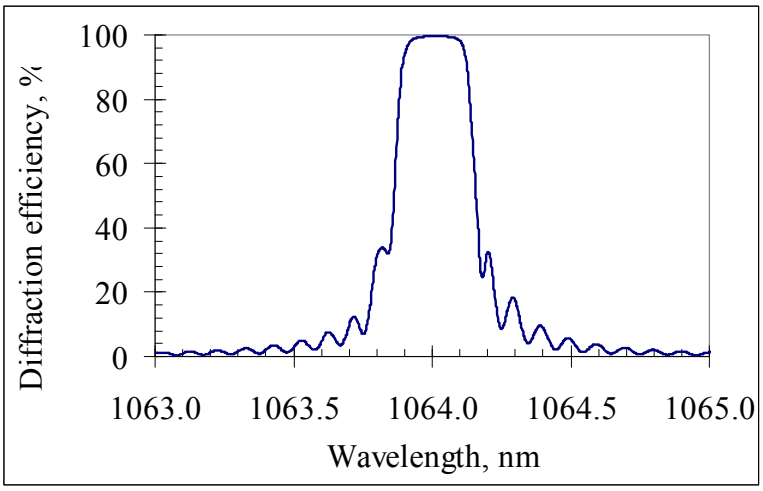

Figure 7.3. Spectral dependence of diffraction efficiency of a reflecting VBG used in an external cavity configuration with an output coupler.

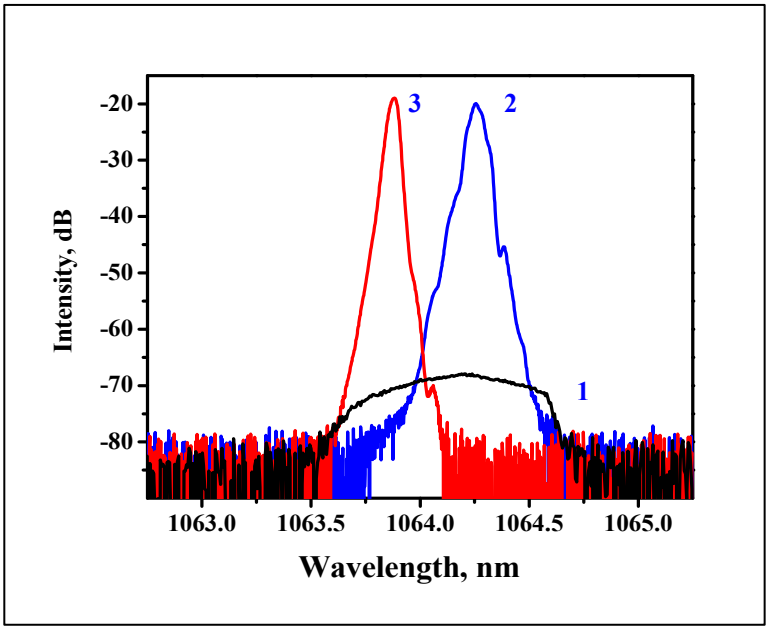

Figure 7.4. Emission spectrum of a fiber laser: 1 – superluminescence below threshold; 2 – laser emission above threshold with no external feedback; 3 – laser emission above threshold with external feedback (tunable by VBG angle).

An external cavity constructed according to Fig. 7.1 uses a reflecting VBG with diffraction efficiency ~ 83 % that also acts as an output coupler. This grating provides spectral selectivity of 50 pm (FWHM) around 1064.15 nm (Fig. 7.5). A combination of high diffraction efficiency and narrow spectral selectivity provides effective spectral narrowing of the fiber laser around central wavelength of 1064.15 nm, corresponding to Bragg wavelength of the grating. Laser linewidth, measured with a scanning Fabry-Perot interferometer, is narrowed down to 2 pm (FWHM) at 1 A pumping current (Fig. 7.6), although some broadening is observed at higher pumping current: 13 pm at 3 A, and 21 pm at 6 A.

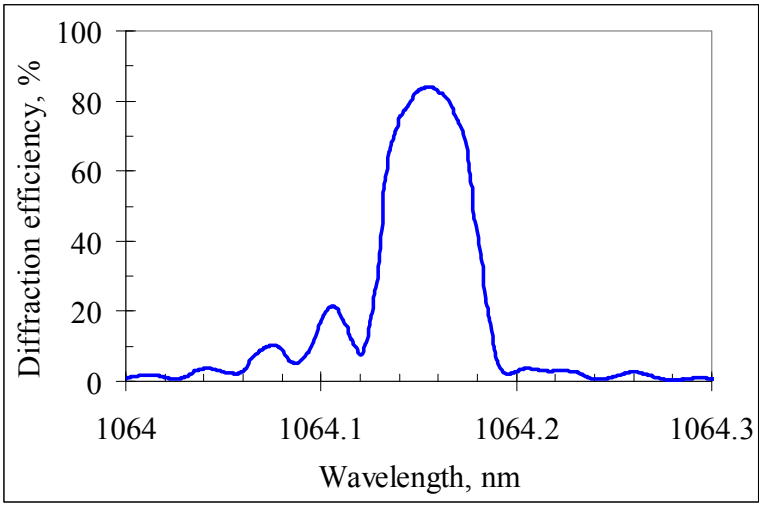

Figure 7.5. Spectral dependence of diffraction efficiency of a reflecting VBG used in an external cavity configuration without an output coupler.

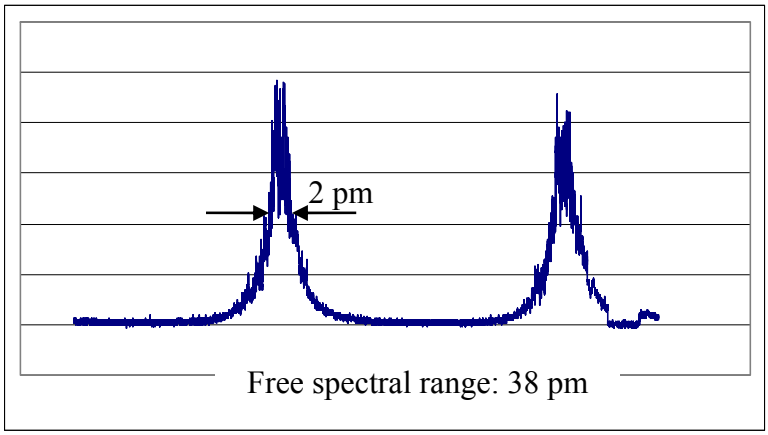

Figure 7.6. Scanning Fabry-Perot interferometer measurement of laser linewidth at 1 A pumping current.

High-power operation of such lasers will result in thermal shift of Bragg wavelength of the grating to a longer wavelength due to absorption of laser radiation. Since Bragg angle of the grating is restricted by cavity geometry, lasing wavelength is forced to shift automatically, following Bragg wavelength of the grating. As long as laser wavelength is within the bandwidth of the rear chirped FBG, wavelength shift occurs without significant decrease of output power. Due to small absorption of PTR glass, there is no significant thermal shift of Bragg wavelength at current power level of a few watts (limited by pump power). Nevertheless, the principle of automatic wavelength control of such laser is demonstrated by intentionally heating the grating to ~ 60° C. Such heating corresponds to absorption of ~ 1 kW laser radiation around 1064 nm. As the result of heating, laser wavelength was shifted by ~ 0.3 nm, without significant decrease of output power.

CHAPTER EIGHT: SPECTRAL BEAM COMBINING WITH PASSIVE WAVELENGTH CONTROL

Based on successful demonstration of spectral control of fiber lasers in an external-cavity configuration, described in the previous chapter, a novel design of a multi-channel self-aligned high-power SBC system is suggested. In this approach a common-cavity is created for all channels by using a common output coupler. Wavelengths of individual lasers are controlled by intra-cavity VBGs which also act as combining elements. Initial lasing wavelengths of channels are selected by respective VBGs with a certain spectral offset such that each VBG reflects the beam of respective channel wavelength while transmitting the rest of the beams with offset wavelengths. Spectral beam combining with high efficiency is achieved by matching spectral offset between channels to spectral selectivity of VBGs. Such SBC system retains perfect alignment as power of individual sources is increased. As resonant wavelengths of VBGs are shifted due to absorption of high-power radiation, lasing wavelengths are automatically adjusted to match the Bragg condition of VBGs. Automatic adjustment of wavelengths occurs as long as they are within the bandwidth supported by the amplifiers. The concept is illustrated in Fig. 8.1 for a 2-channel beam combiner.

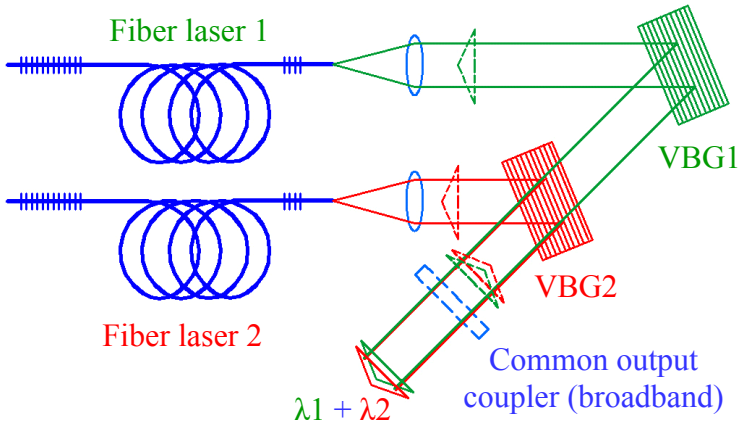

Figure 8.1. Common-cavity spectral beam combining setup with channel wavelengths passively controlled by intra-cavity VBGs.

A two-channel SBC system with passive wavelength control of laser sources demonstrated controllable stable operation. The SBC system consisted of two fiber lasers with output collimators, two narrow-band reflecting VBGs, and a common partially-reflecting output coupler. Two diode-pumped Yb-doped photonic crystal fibers with chirped fiber Bragg gratings (FBGs) on both ends were used. A high-efficiency chirped FBG on one end acts as a back mirror, while a low-efficiency chirped FBG on the other end acts as a weak output coupler in order to prevent fiber damage due to self-pulsing during alignment of an external cavity. Both lasers have luminescence linewidth (FWHM) of ~ 1 nm and peak lasing wavelength of ~ 1064.1 nm at 1 A current at pump diodes. Maximum of emission band is shifted to the longer-wavelength range with increasing of pumping current. Reflecting gratings VBG1 and VBG2 with spectral selectivity (FWHM) of 370 and 300 pm, peak diffraction efficiency of 98 and 94.5% and Bragg wavelength at normal incidence of 1065.4 and 1065.7 nm respectively are used in this experiment. Spectral dependence of diffraction efficiency of these gratings, scanned at small angles of incidence (corresponding to Bragg wavelength of 1064 nm) is shown in Figs. 8.2 and 8.3.

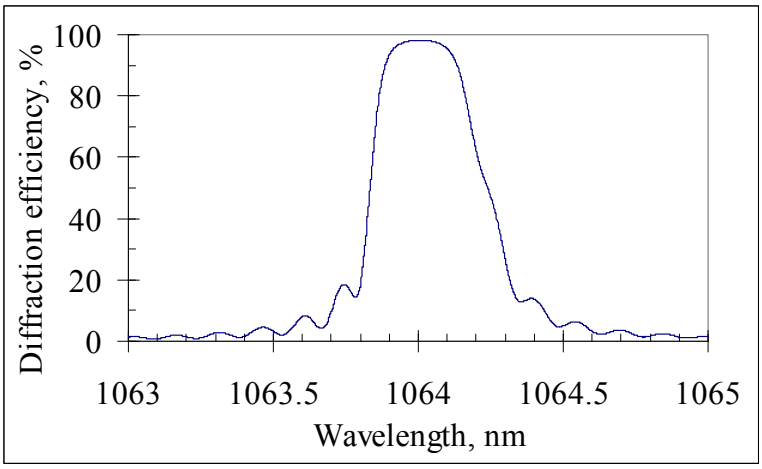

Figure 8.2. Spectral dependence of diffraction efficiency of a narrow-band reflecting VBG (VBG1).

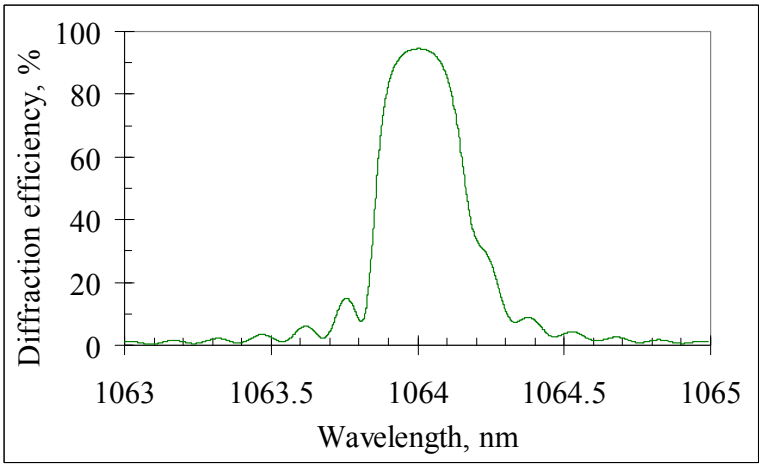

Figure 8.3. Spectral dependence of diffraction efficiency of a narrow-band reflecting VBG (VBG2).

By proper alignment of the gratings and output coupler, a stable two frequency generation is achieved. Both beams coincide in space and propagate along the same resonator axis determined by a common output coupler. In order to imitate behavior of VBGs under the influence of high-power laser radiation that results in heating of the grating, a copper grating holder with four 25 W miniature cartridge heaters has been designed. Temperature control is accomplished by a thermistor as a feedback element set into the holder. Two such devices intended for two VBGs used in the SBC experiment have been assembled and tested. It has been

shown that gratings mounted in these holders do not undergo geometrical distortion when heated up to 90° C. This temperature corresponds to heating of PTR grating by laser radiation of about 2 kW at 1064 nm.

In our experiments channel wavelengths are initially set to $\lambda 1$=1063.60 nm and $\lambda 2$ =1063.97 nm by angles of VBGs, with spectral separation of channels larger than spectral selectivity of VBGs to provide high-efficiency of combining (Fig. 8.4, top). Linewidths of individual channels are less than 100 pm at 4 A pumping current and no coherent interaction between channels occurs during oscillation. Radiation of two lasers is incoherently combined into a single near-diffraction-limited output beam. Due to heating of VBG2 its resonant wavelength is shifted to a longer wavelength. As a result, wavelength of the second laser has changed automatically to satisfy Bragg condition of the heated VBG2, while wavelength of the first laser has remained unchanged.

Heating of both gratings results in spectral shift of both channels without significant deterioration of power in the combined output beam. When both gratings are heated to ~ 60° C, the SBC system output consists of 2 lines shifted to 1063.89 and 1064.28 nm, with the initial spectral separation between channels preserved (Fig. 8.4, bottom). Total output power after heating is increased slightly from 5.1 W to 5.3 W due to a shift of the first laser wavelength to a spectral range, where the fiber laser has higher gain. These results are obtained for an SBC system with external output coupler of 20% reflectivity. It has been found that stable operation of such SBC system requires an output coupler with reflectivity not less than 10%.

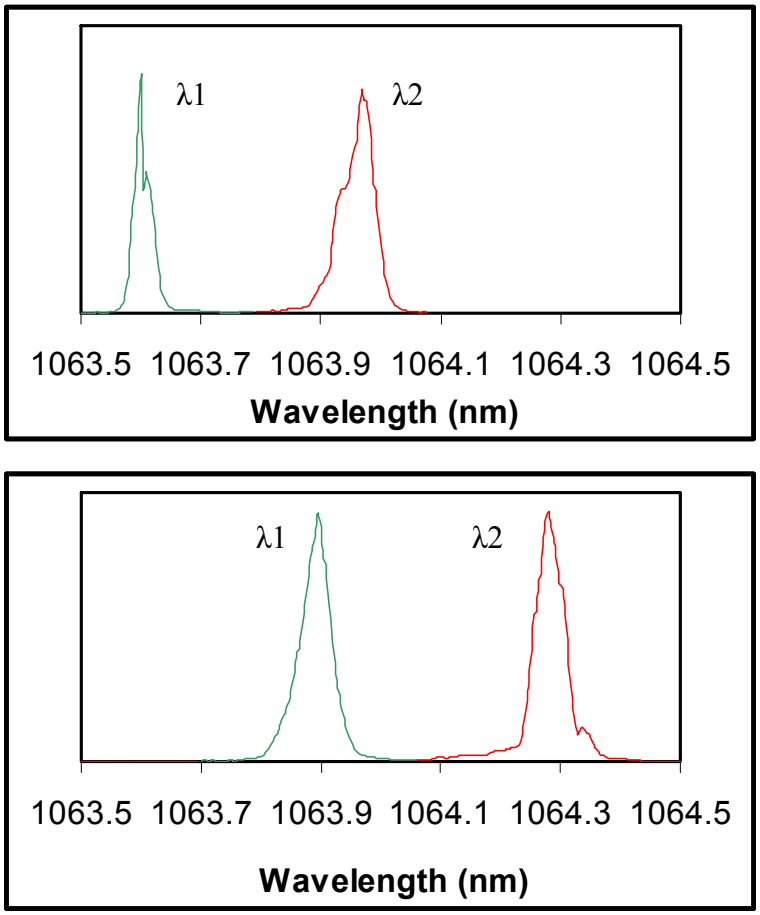

Figure 8.4. Thermal shift of resonant wavelengths in a 2-channel SBC system as a result of heating the gratings: top – room temperature; bottom – T = 60° C.

Performance of the 2-channel SBC system has been investigated at pumping current up to 6 A. In this case output power of the system is more than 10 W and spectral behavior during VBG heating is not changed in comparison with the previously described results. Maximum losses of the system do not exceed 10% and are mainly caused by moving into the edge of the gain spectrum. It has been found, that when spectral line of a laser is close to the edge of the laser luminescence bandwidth, lasing wavelength does not coincide with Bragg wavelength of a VBG (Fig. 8.5). This difference is determined by a convolution of diffraction efficiency of a VBG and gain of a fiber laser and is particularly large for wavelengths close to the edge of the luminescence bandwidth. When VBG is tuned to the shorter-wavelength edge of fiber laser gain,

lasing occurs at a wavelength longer than Bragg wavelength of the VBG and vice-versa. This effect results in a decrease of diffraction efficiency of the VBGs, since Bragg condition is not exactly satisfied. Lasing wavelength in the central part of laser gain (~ 0.5 nm) corresponds to Bragg wavelength of the VBG and diffraction losses are minimized.

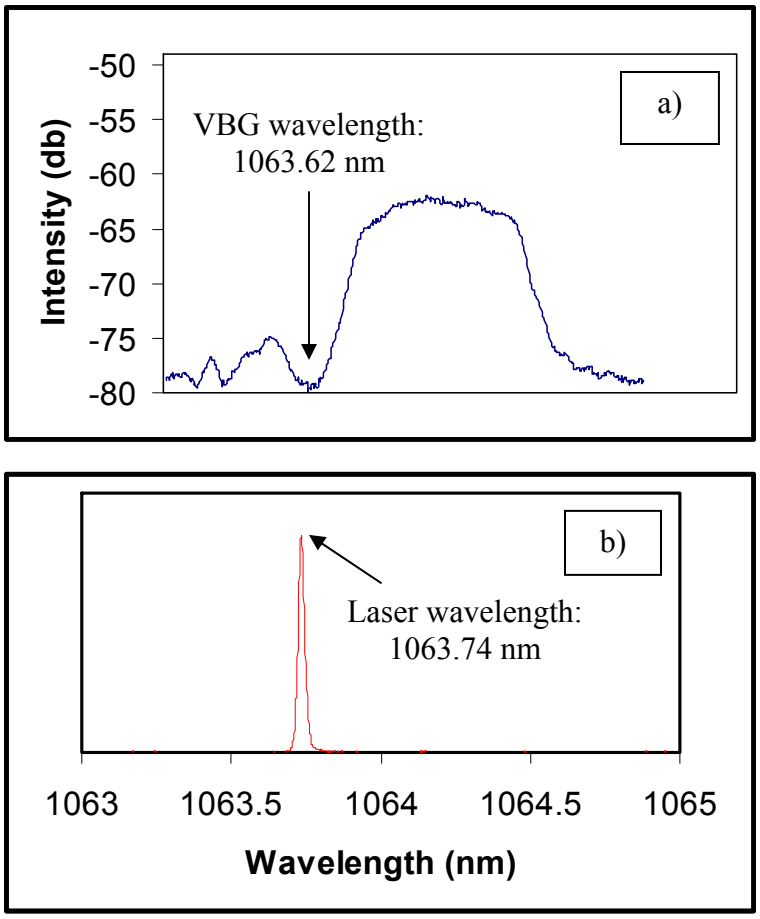

Figure 8.5. Emission spectra of a single fiber laser in external cavity configuration with a VBG and an output coupler: a) – spectrum of superluminescence (below threshold) transmitted through VBG (the dip around λ = 1063.62 nm is determined by Bragg wavelength of VBG); b) – spectrum of laser emission above threshold with feedback from the output coupler (spectral shift to λ = 1063.74 is determined by a convolution of VBG diffraction efficiency and fiber laser gain).

Stable operation of a 2-channel SBC system in a common-cavity configuration with automatic wavelength control of sources has been demonstrated. Output power of the system is about 10 W, limited by the available pump power. System performance does not deteriorate

when beam-combining VBGs are heated to 60° C, which is equivalent to heating of VBGs by about 1 kW of laser radiation around 1064 nm. It has been shown that wavelengths of individual sources automatically adjust to satisfy Bragg condition of the heated VBGs. This means that addition of new channels, failure of channels and increase of power per channel will have no effect on system efficiency. Moreover, a common-cavity SBC system can be operated in a wide range of ambient temperatures without need for re-alignment. This SBC system can be easily scaled by adding more channels and/or increasing power per channel (adding pump power to the amplifiers).

CHAPTER NINE: DESIGN OF 10-100 KW SPECTRALLY-COMBINED LASER SYSTEMS

Based on experimental results described in previous chapters and recent progress in development of high-power laser sources, particularly high-brightness diode and narrow-line fiber lasers, a laser system combining a large number of channels into a single near-diffraction-limed beam with 10 or even 100 kW power can be envisioned [61].

We suggest modular design of such system based on multiplexed volume Bragg gratings. A building block of such system is a compact monolithic multi-channel beam combiner module similar to the one demonstrated in Chapter 4 (Figs. 4.5 and 4.6). A stack of single gratings used in that experiment can be replaced with a single PTR-glass plate with multiple volume Bragg gratings (Fig. 9.1), each grating having a different Bragg wavelength and grating vector tilt. Such multi-grating element will perform identically to a stack of tilted gratings, described earlier. Multiple monolithic modules, combining 4 beams can be stacked linearly (Fig. 9.2). In this concept, each monolithic element combines 4 channels within 1-2 nm bandwidth, and central wavelength of each module is shifted by the same amount such that the spectra are not overlapping. A 5-module beam combiner with dimensions of 90x7x6 cm^3 (Fig. 9.2) is capable of combining 20 beams within 5-10 nm bandwidth. Modules can be mounted on a common frame to improve stability of the system.

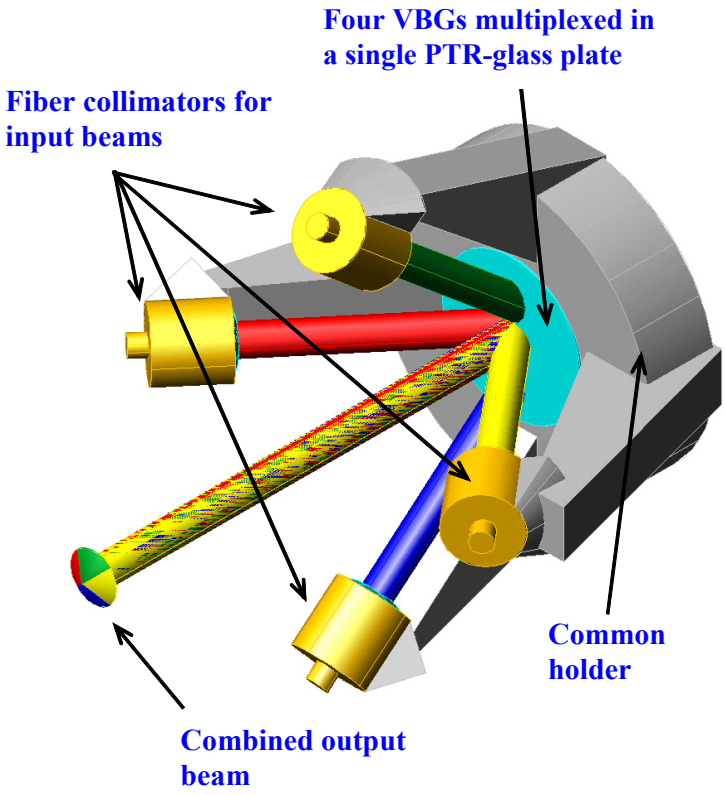

Figure 9.1. Compact monolithic 4-channel beam combining module based on multiplexed VBGs.

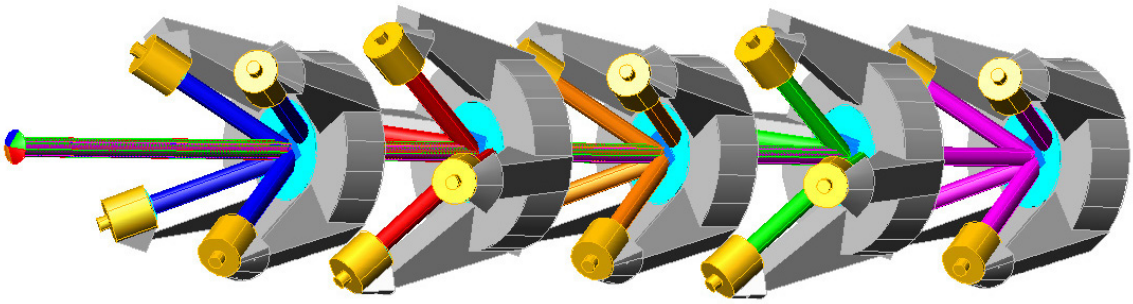

Figure 9.2. Concept of a 5-element stack of monolithic beam combiners.

Automatic passive wavelength control of lasers can be implemented similar to the technique described in Chapters 7 and 8. A common broadband output coupler can be located in the output beam of the system providing feedback to the lasers (Fig. 9.3). In this case the system can be operated in a wide range of ambient temperatures without need for re-alignment. If Bragg wavelengths of gratings are shifted due to heating or cooling, wavelengths of lasers follow

automatically. As long as laser wavelengths are within the gain bandwidth, system efficiency is not effected by this process.

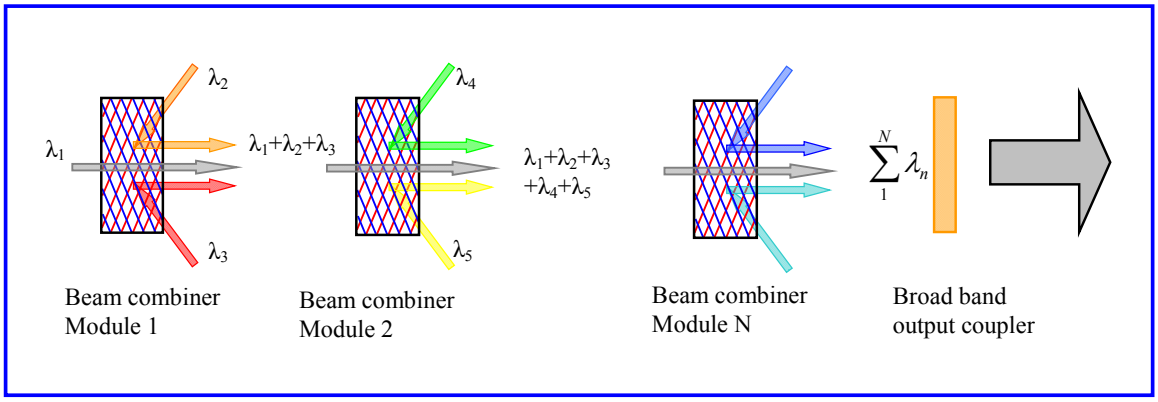

Figure 9.3. Concept of a multi-channel spectral beam combining system based on multiplexed VBGs with a common output coupler for automatic wavelength control of sources.

Basic parameters of spectral beam combining necessary to achieve 10 and 100 kW output power from the suggested laser system are summarized in Table 9.1. It should be noted that spectral beam combining with parameters listed in the table has been demonstrated in separate experiments described in previous chapters.

Table 9.1 Approximate metrics for design of high-power spectrally-combined laser systems.

Total power, kW	10	100
Lasers / module	4	8
Power / laser, W	500	1000
Power / module, kW	2	8
Number of modules	5	12
Combiner length, cm	100	240
Channel separation, nm	0.25	0.25
Bandwidth/module, nm	1	2
Total bandwidth, nm	5	28

CHAPTER TEN: CONCLUSION

Spectral beam combining is an effective technique for scaling high-power laser systems. Multiple high-power lasers with offset wavelengths can be combined into a single near-diffraction-limited beam with increased power and brightness using dispersive optical elements. Volume Bragg gratings recorded in photo-thermo-refractive glass are ideal elements for high spectral density beam combining of high-power radiation. They provide narrow spectral selectivity and can be used for spectral beam combining of multiple channels with spectral separation of 0.5 nm and below. Low absorption in visible and near-IR regions of spectrum and excellent thermo-mechanical properties of PTR glass allow it to withstand high power radiation with high power density.

The goal of the work performed within the scope of this dissertation is to investigate possibility of dense spectral beam combining with volume Bragg gratings in photo-thermo-refracting glass and identify possible limitations. It has been shown that transmitting volume Bragg gratings are capable of spectral beam combining with absolute efficiency > 90%, however their application is limited to spectral separation of channels > 1 nm. For spectral beam combining with channel separation < 1 nm reflecting volume Bragg gratings provide better performance, offering tolerance to beam divergence due to wide angular acceptance and polarization insensitivity.

Spectral beam combining of five channels within 1-2 nm bandwidth around 1064 and 1550 nm with absolute efficiency 92-94% and near-diffraction-limited output beam using

reflecting volume Bragg gratings has been demonstrated. A compact monolithic 4-channel beam-combining module with similar efficiency has been developed. Behavior of narrow-band VBGs under high-power laser radiation has been investigated for power levels up to 570 W and power density up to 5 kW/cm^2. It has been shown that VBGs introduce no significant beam distortions under high-power operation. This has led to demonstration of a laser system with kW-level output power obtained by spectral beam combining of five randomly polarized fiber lasers with 0.5 nm channel separation around 1064 nm using reflecting volume Bragg gratings with absolute efficiency of combining > 90%. Spectral narrowing and control of fiber lasers by reflecting volume Bragg gratings have been demonstrated. Two fiber lasers have been combined in a common-cavity configuration with 0.4 nm spectral separation. Wavelength of each laser is controlled by a grating such that thermal shift of resonant wavelength associated with absorption of high-power radiation results in automatic shift of laser wavelength in order to satisfy Bragg condition.

Parameters of spectral beam combining achieved in these experiments enable a compact laser system capable of producing near-diffraction-limited output beams with 10-100 kW power. Such system combines a large number of channels with small spectral separation. Modular design of the system is suggested.

APPENDIX: PULSE STRETCHING AND COMPRESSION USING CHIRPED VOLUME BRAGG GRATINGS

Introduction to Chirped Volume Bragg Gratings

High-power ultrashort laser pulses have found applications in many fields of modern science. Direct optical amplification of low-power ultrashort pulses can result in detrimental nonlinear effects and laser-induced damage of amplifying medium due to extremely high peak power of amplified pulses. In order to mitigate these effects, a technique of chirped pulse amplification (CPA) has been developed [153]. Using this technique, ultrashort pulses are stretched before amplification using dispersive optical elements. Stretched pulses are then amplified to moderate peak power, preventing damage of amplification medium. Finally, amplified stretched pulses are compressed by dispersive optical elements, resulting in high peak power. The highest peak power that can be obtained using this technique is determined by damage threshold of compressor components. Traditionally, pulse stretching and compression in CPA systems is performed using pairs of surface diffraction gratings [154]. Conventional technology uses metal-coated gratings, however a serious limitation of such compressors is associated with restricted average-power handling capacity. Existing diffraction-grating compressors can typically tolerate tens of watts of average power. With highest-power fiber lasers exceeding 1-kW level, this limitation is becoming the main obstacle to power scaling of ultrashort-pulse laser technology. Implementation of grating-pair stretchers and compressors with high dispersion (high pulse stretching and compression ratio) is also challenging due to

requirements for highly-uniform large-aperture gratings and large grating separation distance. Such gratings are expensive, difficult to manufacture, fragile, and cannot be used in harsh environments. Stretchers and compressors based on these gratings are bulky, difficult to align and susceptible to vibrations and misalignment.

A breakthrough in development of CPA laser systems was achieved by replacing pairs of surface gratings with chirped fiber Bragg gratings in pulse stretchers and compressors [155,156]. This approach has dramatically increased robustness of CPA systems and enabled their use in harsh environments, outside of research laboratories. However, limited aperture of chirped fiber Bragg gratings imposes limitations on peak power achievable with fiber-based pulse compressors due to nonlinear effects and laser induced damage. The use of chirped volume Bragg gratings for pulse stretching and compression has been proposed in order to overcome the mode-area limitation of chirped fiber Bragg gratings [157]. Recent invention of volume Bragg gratings with variable period (volume longitudinally Chirped Bragg Gratings, CBGs) recorded in PTR glass [158] has changed dramatically a design of high power femtosecond lasers. Replacing of bulky pairs of conventional surface gratings with compact and robust CBGs for stretching and compression of laser pulses in CPA systems enabled decrease of size and weight of those systems by several times. Large-aperture PTR-glass chirped Bragg gratings are capable of handling ten-to-hundred times higher average power than can be achieved using conventional surface-grating based technology [159]. Recently, an Yb-doped fiber CPA system that uses chirped Bragg gratings for pulse stretching and compression was demonstrated, providing 50 W average output power with 4.6 picosecond pulses centered at 1055 nm [160]. CPA system with compressed pulse duration down to 670 fs and similar average power has been reported [161].

Recent results to be published by the same group report pulses of 200 fs duration obtained from a power-scalable-Yb-fiber-CPA system that uses CBG-based stretcher and compressor.

Origin of dispersion of chirped Bragg gratings is spectral dependence of group delay of a broadband laser pulse reflected by the grating. Fig. A.1 shows such grating with period that is variable in z-direction. Period of the grating is varied such that Bragg condition for different wavelengths is satisfied at different locations along the direction of light propagation (z). This means that different wavelengths of a spectrally broad pulse, reflected at different locations, acquire different group delay due to the difference in the optical paths inside the grating. Fig. A.2 shows a laser beam incident on a chirped Bragg grating from the right-hand side and reflected by the grating. Monochromatic beam with three different wavelengths is used in Fig. A.2 (a-c). The beam is reflected by the grating at different locations along the z-axis, where local period of the grating corresponds to a Bragg condition for a given wavelength. In Fig. A.2 (d), a laser pulse with broad bandwidth is reflected by the same grating. In this case no sharp plane of reflection is observed and the reflection is distributed through the thickness of the grating with different spectral components of the beam reflected at different locations along the z-axis. The optical path lengths difference between the different spectral components leads to a frequency-dependent group delay. For a broadband pulse incident on the grating, the diffracted pulse is either stretched or compressed in time, depending on the spectral phase of the input pulse. If spectral phase of the input pulse and dispersion of the grating are known, output pulse duration and exact pulse shape can be determined. More detailed description of the principle of pulse stretching and compression by a volume diffractive grating with variable period is given in [158].

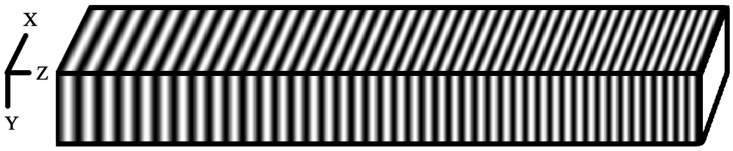

Figure A.1. Volume Bragg grating with variable period along the beam propagation (z-direction) – volume longitudinal chirped Bragg grating (CBG). Grating period and thickness are not in scale; thickness is usually tens of thousand times larger than the period.

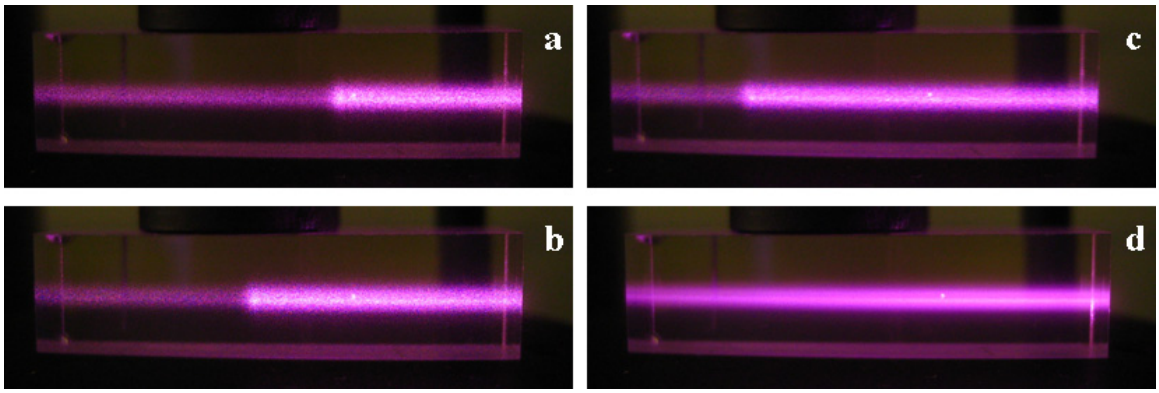

Figure A.2. Laser beam reflected by a chirped Bragg grating: a-c – monochromatic CW beam at different wavelengths, d – broadband mode-locked laser beam. The input beam is incident on the grating from the right-hand side.

Nonlinear Technique For Dispersion Characterization

Introduction

While the usefulness of PTR-glass chirped Bragg gratings for CPA has been demonstrated experimentally, only a phenomenological description of pulse stretching and compression properties of these elements has been given in prior work. A quantitative model of grating dispersion that accounts for higher-order dispersion terms, would allow calculation of exact shape and duration of a pulse diffracted by a CBG from spectral phase and intensity of an

arbitrary input pulse. It means that pulse propagation through other elements of a CPA laser system, particularly amplifying medium, can be modeled rigorously. Such modeling can be critical in design of high-power CPA systems. It also allows using chirped Bragg gratings in conjunction with other dispersive elements (surface grating based stretchers and compressors, prism pairs, chirped mirrors, etc.) to compensate for dispersion of amplifier and other elements of a CPA system and achieve efficient control of dispersion. Finally, a quantitative model that relates grating dispersion to physical properties of a CBG can open a new research direction, namely engineering of basic CBG parameters to modify higher-order dispersion. This technology can potentially lead to a much broader range of applications of CBGs in dispersion compensation and femtosecond pulse shaping.

In order to develop a quantitative model of dispersion and determine pulse stretching and compressing capabilities of PTR-glass chirped Bragg gratings, a method for measuring dispersion properties of these elements, including higher-order dispersion terms needs to be developed. Dispersion of optical materials is traditionally measured using Fourier-Transform Spectral Interferometry (FTSI) [162]. However, characterization of dispersion of chirped Bragg gratings using FTSI is significantly complicated, since dispersion of these elements is many orders of magnitude higher than dispersion of most materials, at least for the same thickness of samples. While it is theoretically possible to extract spectral phase of a pulse stretched by a chirped Bragg grating using FTSI, spectral measurements with extremely fine resolution are required, far beyond the limit of modern spectrometric devices. To overcome this limitation, we propose using cross-correlation frequency-resolved optical gating for dispersion characterization of CBGs and other highly-dispersive optical elements. This technique is based on spectrally resolved second-order cross-correlation (sum frequency generation) of a stretched pulse with a

reference ultra-short pulse. Accurate dispersion characterization of optical elements with high pulse stretching ratio is possible using this method, without requirements for very fine resolution of spectral measurements of cross-correlation signal.

Frequency-resolved optical gating (FROG) [163] has been introduced as a technique for characterization of intense ultra-short pulses. SHG FROG, the most sensitive FROG variant, uses second harmonic generation as gating mechanism. The test pulse is split into two parts which are mixed in a nonlinear crystal and the SHG signal is spectrally resolved as a function of the delay between the two pulses. However, traditional FROG technique is limited to high-intensity short pulses, and is not suitable for characterization of highly chirped stretched pulses. A reference-type measurement approach, cross-correlation frequency-resolved optical gating (XFROG) [164] introduced to characterize low-intensity ultra-short pulses, is based on sum frequency generation between the high-intensity reference pulse and a weak test pulse. This approach has been used for studying ultra-short pulse propagation in fibers [165-167]. XFROG technique can be adopted for dispersion characterization of optical elements with high pulse stretching ratio (chirped Bragg gratings, traditional surface-grating-based pulse stretchers, etc). The phase retrieval algorithm is significantly simplified when cross-correlation of an ultra-short high-intensity reference pulse with a highly-chirped stretched pulse is analyzed. Spectral phase of a stretched pulse and dispersion of the stretcher can be retrieved without having a well-characterized reference pulse, as long as reference pulse duration is much shorter than the stretched test pulse. We believe this technique can provide good accuracy of dispersion measurement for optical elements with pulse stretching ratio of 20 and above. The high limit for the stretching ratio that can be measured with this technique is limited by the instantaneous intensity of the stretched pulse, required for efficient non-linear interaction with the reference pulse.

Measurement Procedure

Experimental setup for measuring dispersion of chirped Bragg gratings is shown in Fig. A.3. An ultra-short pulse from an amplifier is split by the beam-splitter. One part of the pulse is reflected by a chirped Bragg grating and the pulse is stretched due to dispersion of the grating. Spectral phase of this test pulse provides full information about dispersion properties of the grating under test. Another part of the pulse is directed along a variable-delay arm and serves as an ultra-short reference pulse. The two pulses are incident onto a non-linear crystal, oriented for maximum second harmonic generation (SHG). Each of the pulses generates a second-harmonic pulse propagating in the same direction as the pulses. Additionally, non-linear interaction of the two pulses produces sum-frequency generation (SFG) signal that propagates along the axis bisecting the angle between the two beams. Spectrum of SFG signal is collected by a spectrometer as delay τ is varied. In this arrangement, the stretched pulse is time-gated by the reference pulse. Spectral content of the gated temporal slice of the test pulse can be retrieved from SFG spectrum if spectrum of the reference pulse is known. By varying the delay τ between the two pulses, the time-frequency trace and spectral phase of the test pulse can be found. In case of a highly chirped test pulse with well-behaved spectral phase, phase retrieval procedure is significantly simplified. If spectral content of the time-gated slice of the test pulse is narrow compared to the required accuracy of dispersion measurement, spectral phase of the stretched pulse can be retrieved by a self-referencing algorithm, without using the reference pulse spectrum. Data acquisition and phase retrieval are significantly simplified in this case.

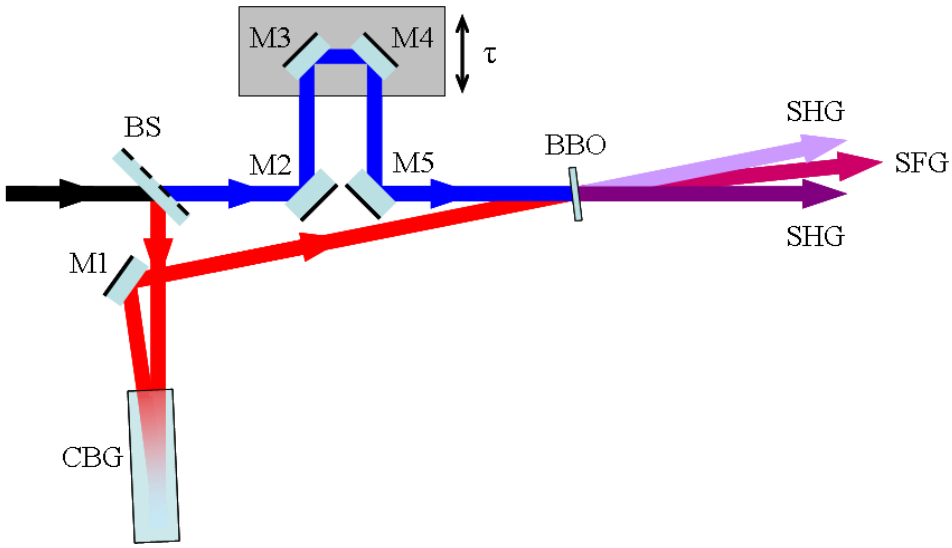

Figure A.3. Optical scheme for dispersion characterization of CBGs. BS – beam-splitter, M1-M5 – mirrors, BBO – non-linear crystal, CBG – chirped volume Bragg grating.

The optical setup of Fig. A.3 is used to characterize dispersion of a chirped Bragg grating. The grating has the following key parameters: thickness 27.2 mm, center wavelength ~ 801.5 nm, bandwidth ~ 10.5 nm, average relative diffraction efficiency ~ 65% (Fig. A.4) and material losses ~ 20% (measured outside of the reflection band). A Ti:S amplifier delivering 60 fs pulses with energy ~60 μJ per pulse at 1 kHz repetition rate is used as an input. Beam diameter is ~ 2mm (full width at e^{-2} maximum). The pulses have a bandwidth of ~ 22 nm (full width at half maximum) centered around 807 nm. The grating provides stretch ratio ~ 2000 with stretched pulse duration on the order of 150-200 ps. A type 1 BBO crystal with 0.25 mm thickness is used for sum-frequency generation. Spectrum of SFG signal (Fig. A.5) is collected for various values of delay τ. Fig. A.6 shows the shift of SFG spectrum as the delay τ is varied and the stretched pulse is sliced (time-gated) by the reference pulse. Since the spectrum of the reference beam is virtually unchanged during the experiment, this shift represents temporal variation of the frequency (wavelength) of the stretched pulse.

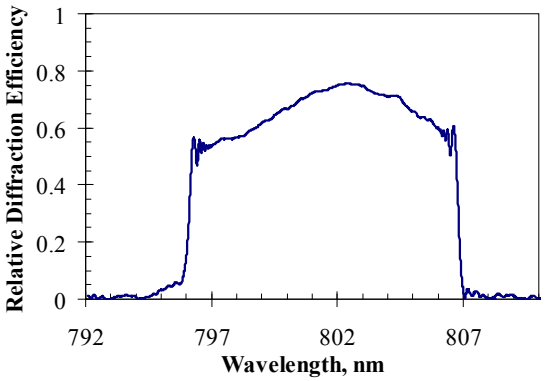

Figure A.4. Spectral dependence of relative diffraction efficiency of a chirped Bragg grating under test.

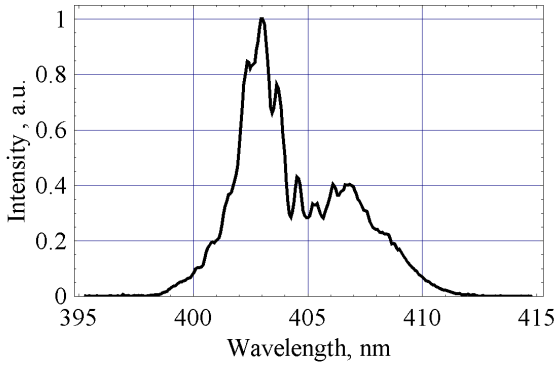

Figure A.5. A sample of collected SFG spectrum.

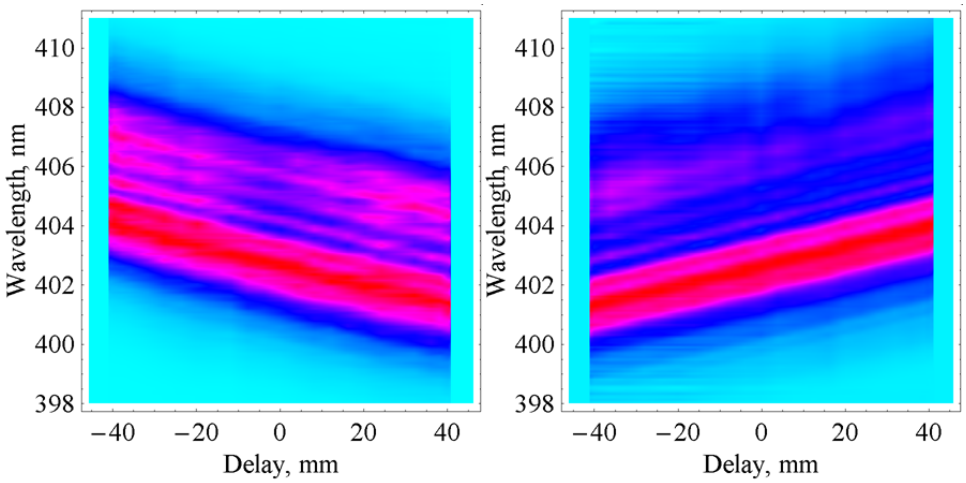

Figure A.6. SFG spectrum as a function of delay τ for two orientations of the grating with opposite faces of the grating used as the input face.

Dispersion Analysis

Using data of Fig. A.6, spectral dependence of time delay of the stretched pulse due to dispersion of the chirped Bragg grating can be extracted. Consequently, dispersion of the grating can be analyzed. A linear fit to the experimental data (Fig. A.7) yields first-order dispersion parameter: 26.3 ps/nm and -25.6 ps/nm for the two orientations of the grating. These values multiplied by grating bandwidth (10.5 nm) correspond to the round-trip time through the thickness of the grating, indicating good accuracy of measurements.

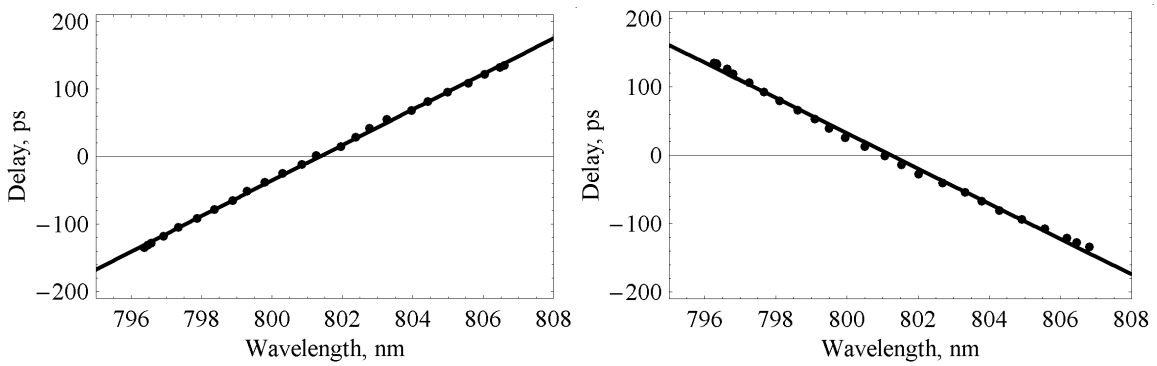

Figure A.7. Spectral dependence of time delay in a stretched pulse for two orientations of the grating with opposite faces of the grating used as the input face. Points – experimental data, lines – linear fits.

In general, dispersion of optical elements is characterized in terms of change in spectral phase of a laser pulse with broad bandwidth after propagation through the dispersive optical element. The change in spectral phase of a pulse can be described by a Taylor series expansion about central frequency ω_0:

$$\varphi(\omega) = \varphi_0 + \left.\frac{\partial\varphi}{\partial\omega}\right|_{\omega=\omega_0} \cdot(\omega-\omega_0) + \frac{1}{2}\left.\frac{\partial^2\varphi}{\partial\omega^2}\right|_{\omega=\omega_0} \cdot(\omega-\omega_0)^2 + \frac{1}{6}\left.\frac{\partial^3\varphi}{\partial\omega^3}\right|_{\omega=\omega_0} \cdot(\omega-\omega_0)^3 + \ldots \quad \text{(A.1)}.$$

The terms corresponding to the different orders are: φ_0 – a common phase term, $\left.\frac{\partial\varphi}{\partial\omega}\right|_{\omega=\omega_0}$ – group delay, $\left.\frac{\partial^2\varphi}{\partial\omega^2}\right|_{\omega=\omega_0}$ – group delay dispersion (GDD), and $\left.\frac{\partial^3\varphi}{\partial\omega^3}\right|_{\omega=\omega_0}$ – third-order dispersion (TOD). Group delay describes an overall time delay of the pulse without an effect on pulse shape, while GDD, TOD, and other higher-order coefficients of the expansion affect temporal pulse duration and shape. Knowledge of GDD allows one to predict approximate temporal duration of a stretched/compressed pulse, while TOD and higher-order terms can be used to determine the exact pulse shape. GDD, TOD, and other higher-order coefficients of the expansion provide full information on dispersion properties of a dispersive optical element under test. For ultrashort pulses with moderate spectral bandwidth (up to tens of nm), contribution of terms higher than TOD is negligibly small, so we are primarily interested in quantifying GDD and TOD of PTR-glass chirped Bragg gratings.

In order to quantify dispersion in terms of parameters used in Eq. A.1, a polynomial fit to the collected data is performed in the frequency domain. Results of this fit are shown in Fig. A.8. Dispersion coefficients found from the fits are: $GDD = \left.\frac{\partial^2\varphi}{\partial\omega^2}\right|_{\omega=\omega_0} = -8.9\cdot10^6\ fs^2$, $TOD = \left.\frac{\partial^3\varphi}{\partial\omega^3}\right|_{\omega=\omega_0} = -4.5\cdot10^7\ fs^3$ for one orientation of the grating and $GDD = \left.\frac{\partial^2\varphi}{\partial\omega^2}\right|_{\omega=\omega_0} = +8.6\cdot10^6\ fs^2$, $TOD = \left.\frac{\partial^3\varphi}{\partial\omega^3}\right|_{\omega=\omega_0} = +1.1\cdot10^8\ fs^3$ for another orientation. As expected, the dispersion coefficients are of opposite signs for the two orientations. The difference in magnitudes of GDD and TOD for the two orientations is attributed to the variation of grating properties across the aperture. Since no particular attention was paid to preserving the

absolute position of a CBG when grating orientation was changed, we believe that different locations on the grating aperture were sampled during the two measurements.

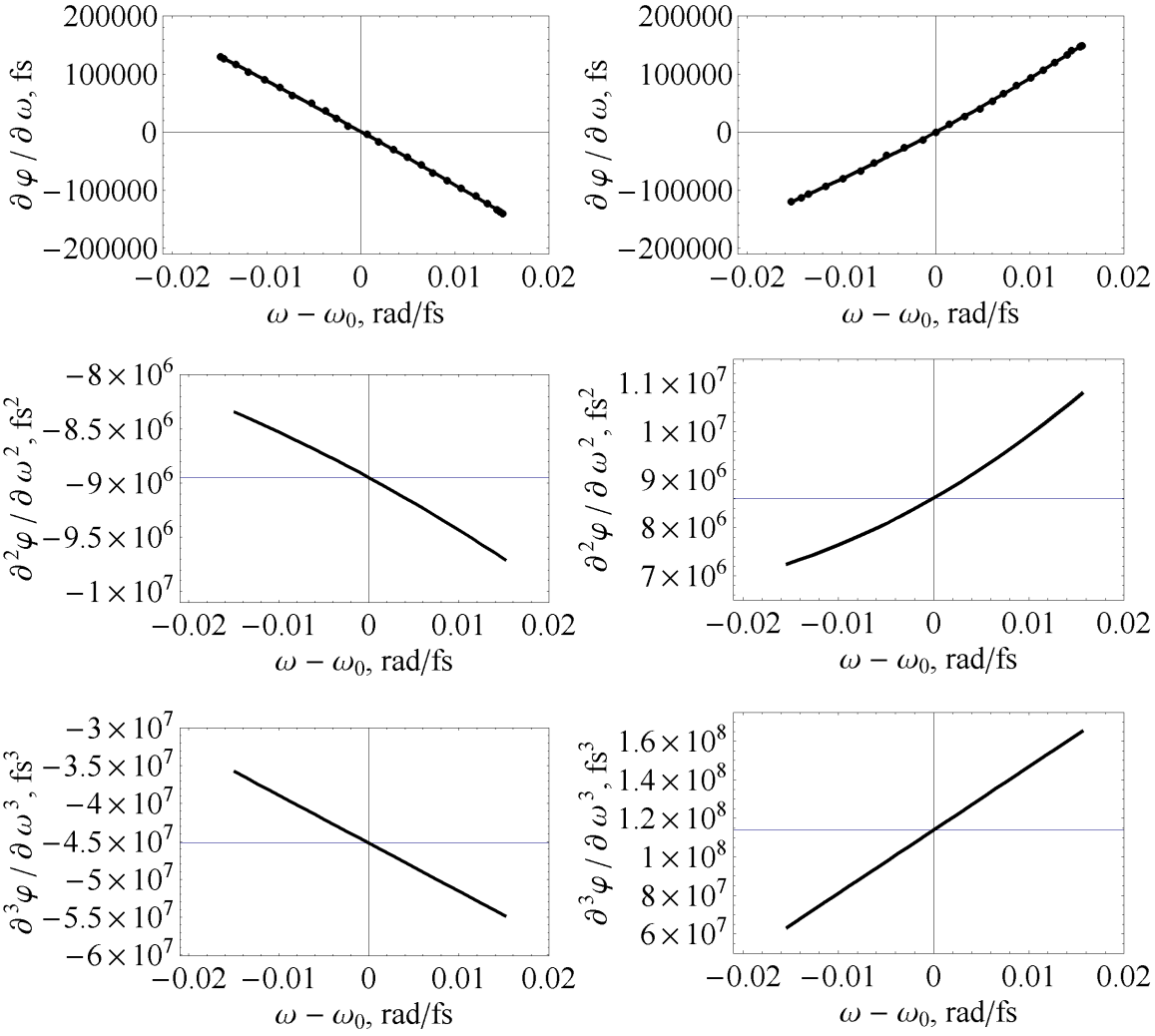

Figure A.8. Analysis of dispersion properties of a chirped Bragg grating for two orientations of the grating with opposite faces of the grating used as the input face. Points – experimental data, lines – polynomial fits.

To conclude, a method for dispersion characterization of highly-dispersive chirped volume Bragg gratings based on spectrally resolved cross-correlation of a stretched pulse with a reference ultra-short pulse is suggested. Accurate dispersion characterization of optical elements with high pulse stretching ratio is possible using this method, without requirements for very fine resolution of spectral measurements of cross-correlation signal. The proposed technique is used

to measure dispersion of a chirped Bragg grating recorded in PTR glass. The measurement is performed for two orientations of the grating with opposite faces of the grating used as the input face. It is shown that dispersion of the grating has an opposite sign and almost the same magnitude for the two orientations of the grating. Higher-order dispersion is analyzed for both configurations. Results of these experiments show that chirped Bragg gratings in PTR glass provide dispersion almost linear with wavelength. Some variation of dispersion across the aperture of the grating is found, mostly in the amount of third-order dispersion contribution.

Pulse Stretching/Compression Experiments

Chirped Bragg gratings can be used as pulse stretching and compression components of a CPA system. The same (or identical) grating that is used for pulse stretching can be used for re-compression with the opposite face of the grating used as an input face. Since dispersion of a chirped Bragg grating has the same magnitude and opposite sign when the opposite faces are used as an input face, exact dispersion cancellation can be achieved and ultrashort pulses can be re-compressed to near-bandwidth-limited duration.

In the following subsections two experimental demonstrations of pulse stretching and compression by chirped volume Bragg gratings are described. The two experiments have significant differences that show flexibility of using CBGs for pulse stretching and compression. In the first experiment, a single CBG is used for stretching and compression simultaneously. The beams are incident on the CBG at normal incidence (perpendicular to grating planes). Beams reflected by the CBG are counter-propagating and overlapped with the incident beams. Beam injection and extraction is realized by using polarization rotation and polarizing optical elements.

In the second experiment separate gratings with similar properties are used for pulse stretching and compression. The use of polarizing elements is avoided by directing incident beams onto the grating at small angles such that reflected and incident beams are spatially separated. Another difference between the two experiments is the use of different laser sources and consequent modification of CBG parameters. In the first experiment a Ti:S oscillator with 6 nm FWHM (full width half maximum) bandwidth centered around 801.5 nm is used. An Yb-doped-crystal oscillator used in the second experiment delivers femtosecond pulses with 7 nm FWHM bandwidth, centered around 1028 nm.

Stretching and Compression Using a Single Grating

A chirped Bragg grating with parameters described in section A.2 is used to stretch near-bandwidth-limited 140 fs pulses to about 130 ps and re-compress the pulses back to near-bandwidth-limited duration. A commercial Ti:S oscillator delivering 140 fs pulses at repetition rate of 82 MHz with 2 W average power is used as an input. In our experiment the input beam with horizontal polarization is directed onto a chirped Bragg grating through a Glan-Taylor prism and a quarter-wave plate (Fig. A.9). The beam incident on the Bragg grating is circularly-polarized. It should be noted that diffraction properties of chirped Bragg gratings are polarization-independent since they are used at normal incidence. The beam is reflected by the grating, the polarization is changed to vertical as it passes through the quarter-wave plate again, and the beam is reflected by the Glan-Taylor onto a steering mirror. The pulses are stretched to ~ 130 ps as the beam is reflected by the chirped Bragg grating. Another Glan-Taylor prism and a quarter-wave plate are used to redirect the stretched pulse onto the same Bragg grating from the opposite side. The pulses are re-compressed by the grating. Polarization of the beam reflected by

the grating becomes horizontal after it passes through a quarter-wave plate and the beam is transmitted through the Glan-Taylor prism.

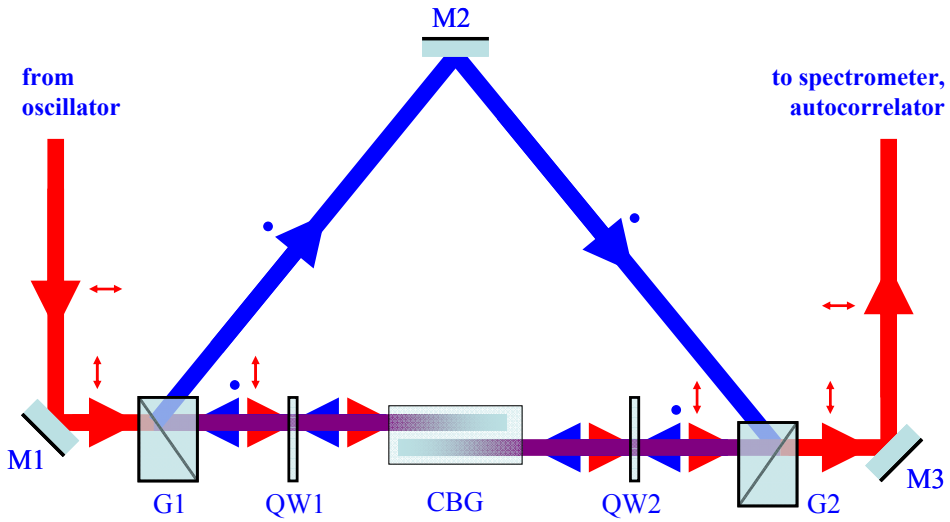

Figure A.9. Experimental setup for stretching and re-compression of ultrashort pulses using a chirped Bragg grating. CBG – chirped Bragg grating, G1-G2 – Glan-Taylor prisms, QW1-QW2 – quarter-wave plates, M1-M3 – mirrors.

The bandwidth of an input pulse is ~ 6 nm (full width half maximum) centered around 801.5 nm (Fig. A.10). The bandwidth of a stretched pulse is slightly narrowed to ~ 5.4 nm (full width half maximum) due to the spectrally-dependent diffraction efficiency of the grating and is sharply cut at the level of ~ 10% by the 10.5 nm bandwidth of the grating. Spectral bandwidth of the recompressed pulse is further narrowed by the grating to ~ 4.7 nm (full width half maximum).

Spectrum of a pulse in the frequency domain $I(\upsilon)$ is proportional to $|E(\upsilon)|^2$. $E(\upsilon)$ and $E(t)$ are related by a Fourier Transform. Temporal shape of a pulse is proportional to $|E(t)|^2$. Assuming flat spectral phase, it is possible to calculate "transform-limited" or "bandwidth-limited" pulse shape from intensity spectrum of the pulse. The transform-limited pulse represents the shortest pulse possible for a given spectrum. A pulse with the same bandwidth and non-flat spectral phase is "chirped" and is always longer than the transform-limited pulse. Spectra of Fig.

A.10 are used to calculate transform-limited pulse shapes (Fig. A.11). Transform-limited pulse duration is 110 fs for the input pulse and 155 fs for the re-compressed pulse (full width half maximum).

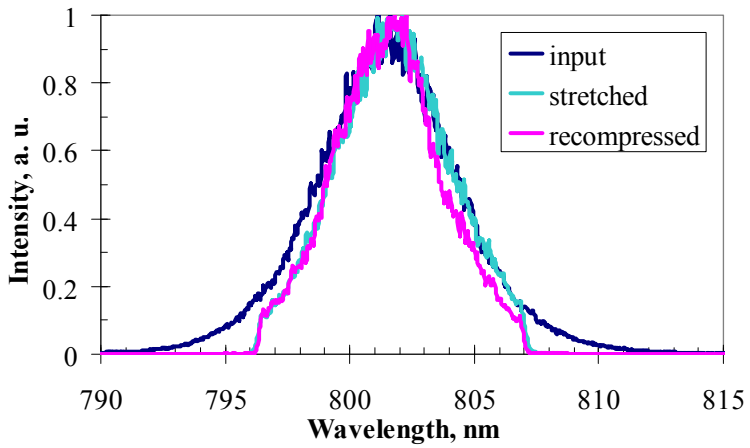

Figure A.10. Spectra of input, stretched, and re-compressed pulses.

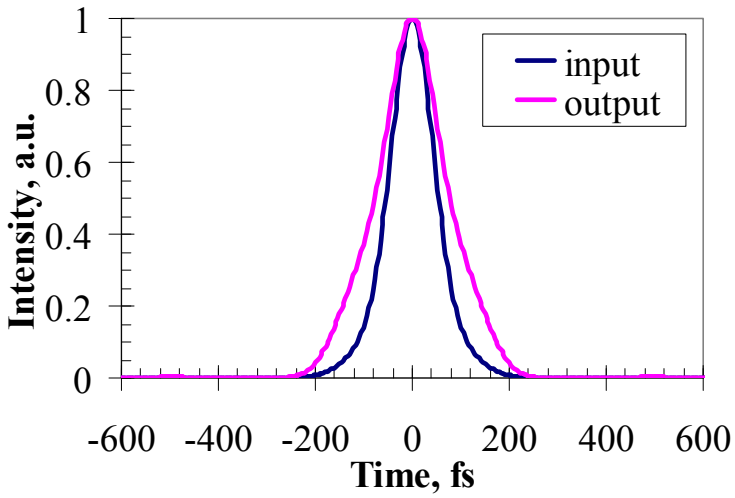

Figure A.11. Theoretically calculated pulse shape limited by the bandwidth of input and output pulses.

Temporal shape and duration of ultrashort pulses can not be measured directly. Most commonly, an autocorrelation of the pulse is measured and certain temporal and spectral shape of the pulse is assumed to quote the pulse duration value. Assumption of a wrong pulse shape

can be a source of significant error. When temporal shape of a pulse is not known, but pulse spectrum is available, autocorrelation of a transform-limited pulse shape can be calculated and compared to a measured autocorrelation trace of the pulse. The ratio of widths of the measured and theoretical autocorrelations can be used to determine the ratio between the real pulse duration and the transform-limited value (a "times-transform-limited" factor). Autocorrelations calculated for the bandwidth-limited pulse shapes of Fig. A.11 are shown in Fig. A.12. Full widths at half maximum of the autocorrelations are 168 and 261 fs for the input and output pulses respectively. Autocorrelation traces of input and output pulses measured using a collinear intensity autocorrelator are shown in Fig. A.13. Full widths at half maximum of the measured autocorrelations are 214 and 332 fs for the input and output pulses respectively. From the ratio of autocorrelation widths, both the input and the output pulses are about 1.27 times-transform-limited. It means that almost perfect pulse re-compression by the chirped Bragg grating is achieved.

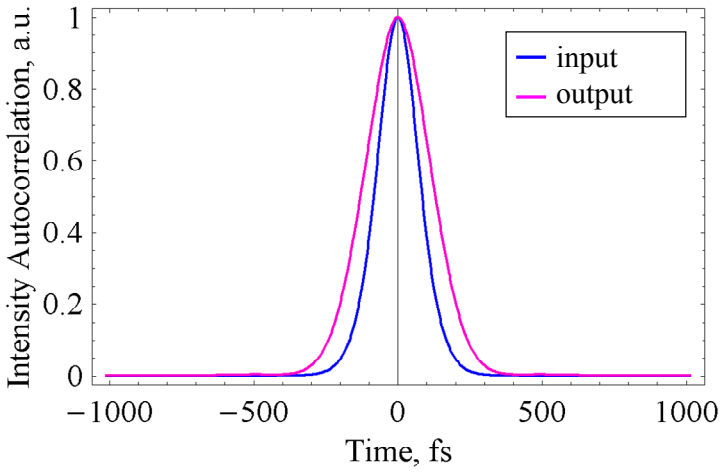

Figure A.12. Theoretical autocorrelation traces of transform-limited input and output pulses.

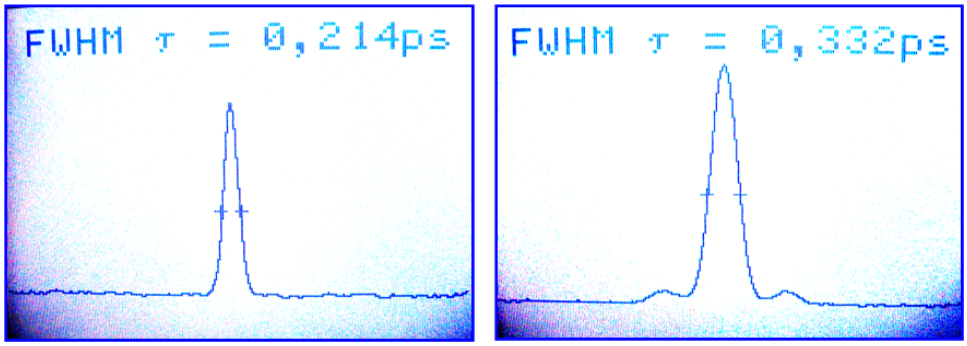

Figure A.13. Measured autocorrelation traces of input (left) and output (right) pulses.

Applying the times-transform-limit factor to the transform-limited pulse shapes of Fig. A.11, pulse duration can be estimated: ~ 140 fs (input) and ~ 195 fs (output). The difference in pulse duration is caused by spectral narrowing shown in Fig. A.10, which leads to increased transform-limited duration for the re-compressed pulse. This narrowing occurs due to spectral non-uniformity of diffraction efficiency and the finite bandwidth of the grating (Fig. A.4). Even though pulse re-compression to near-transform-limited pulse duration by a chirped Bragg grating is demonstrated experimentally, output pulse is somewhat longer than the original pulse. When re-compression to the original pulse duration is required, chirped Bragg gratings with spectrally-uniform diffraction efficiency and wider bandwidth have to be used. We estimate that bandwidth of the grating equal to twice the pulse bandwidth (full width at half maximum) is sufficient for pulse re-compression to the duration of the original input pulse. Chirped Bragg gratings with wider bandwidth and very high spectrally-uniform diffraction efficiency have been recently demonstrated and will be used in the future experiments.

Stretching and Compression Using Separate Gratings

Optical setup and alignment of stretcher and compressor can be significantly simplified by using two separate CBGs at small angles of incidence (Fig. A.14). Pulse stretching and compression using this arrangement has been demonstrated in the following experiment.

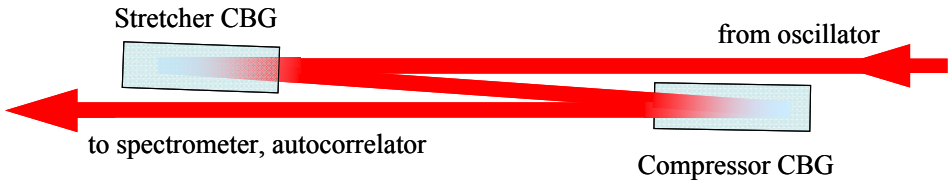

Figure A.14. Optical setup for pulse stretching and compression using two separate CBGs at small angles of incidence.

A femtosecond oscillator that delivers transform-limited pulses with 7 nm FWHM bandwidth centered around 1028 nm (Fig. A.15) at 44 MHz repetition rate is used. Intensity autocorrelation of oscillator pulses measured using a non-collinear autocorrelator has FWHM of 245 fs. This autocorrelation is fit, assuming $Sech^2$ temporal intensity shape of a pulse, yielding 155 fs FWHM of pulse intensity. Transform-limited pulse duration calculated from the collected spectrum of Fig. A.15 is 142 fs with autocorrelation FWHM of 225 fs (Fig. A.16). It means that oscillator pulses are near-transform-limited in duration (~1.1× transform-limit).

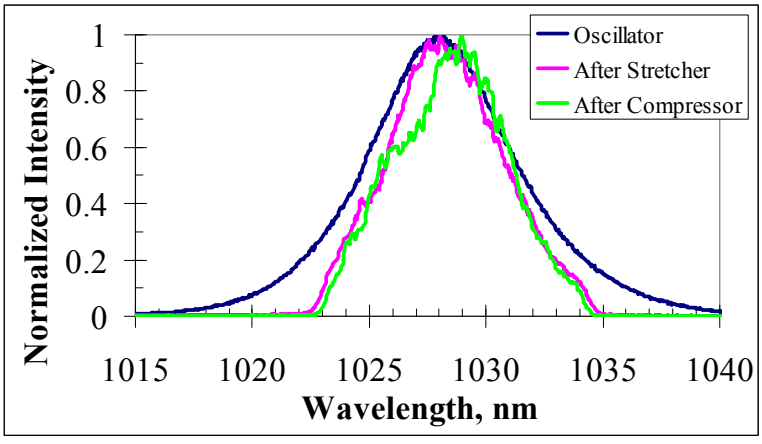

Figure A.15. Spectrum of oscillator pulses and pulses after CBG stretcher and CBG compressor.

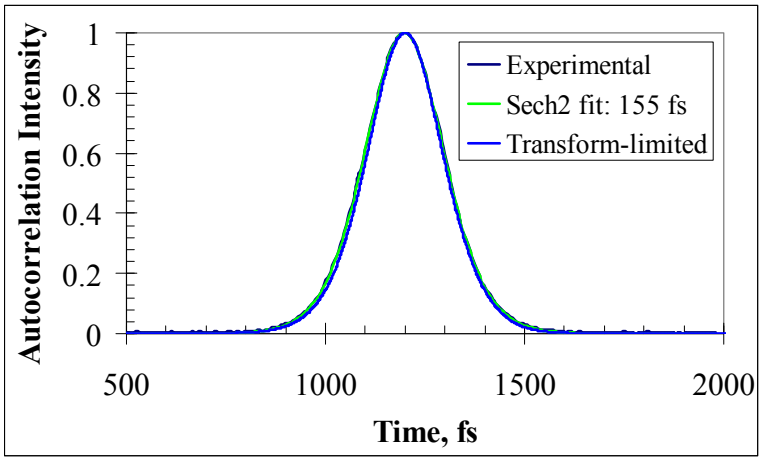

Figure A.16. Autocorrelation function of oscillator pulses. Experimental data is overlapped with an autocorrelation of $Sech^2$ pulses and a calculated autocorrelation of transform-limited pulses.

Pulse train from oscillator is directed onto a 32-mm thick volume diffractive grating with a linearly variable period. This grating has central wavelength of 1028 nm, FWHM bandwidth of 11.6 nm, and diffraction efficiency > 95% over ~ 10 nm bandwidth (Fig. A.17).

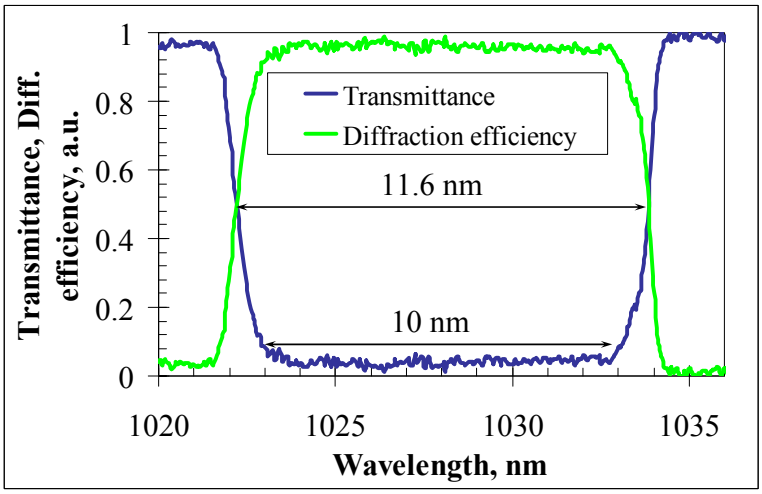

Figure A.17. Transmittance and diffraction efficiency of a pulse-stretching CBG.

Pulses diffracted by this grating are stretched to about 160 picoseconds duration (FWHM). Due to the sharp edges of the diffraction efficiency profile (Fig. A.17), spectrum of the stretched pulse is modified by the grating (Fig. A.15). Overall shape of the spectrum is no longer $Sech^2$, long tails of pulse bandwidth are cut and FWHM is reduced to ~ 5.6 nm.

Next, the pulses are re-compressed using a CBG with properties similar to the stretcher grating. Compressor CBG has thickness of 32 mm with period varying linearly with thickness at the same rate as the stretcher grating. Bandwidth of this grating is about 11.6 nm FWHM and diffraction efficiency > 95% bandwidth is ~ 10.1 nm (Fig. A.18).

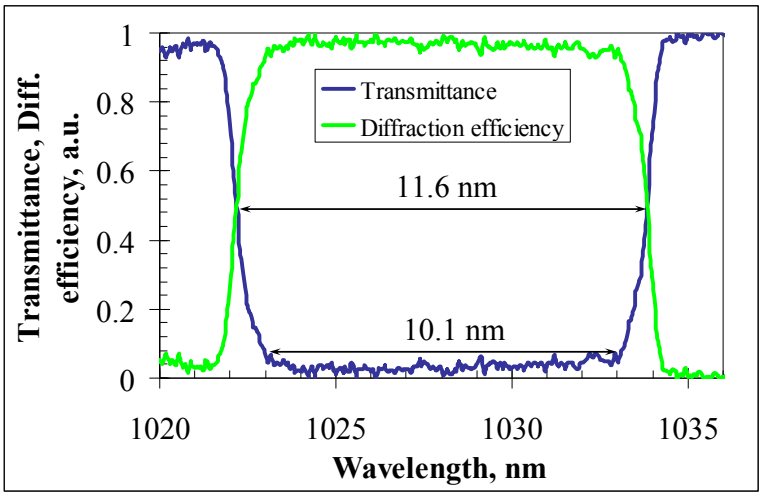

Figure A.18. Transmittance and diffraction efficiency of a pulse-compressing CBG.

Spectrum of compressed pulses is shown in Fig. A.15. Using this spectrum, a transform-limited shape of compressed pulses is calculated. FWHM duration of the transform-limited pulse is 332 fs. An autocorrelation of transform-limited pulses is calculated (Fig. A.19) with FWHM about 450 fs.

Experimental trace 1 shows a "wing-free" autocorrelation with 520 femtoseconds FWHM. Estimated pulse duration is 385 femtoseconds, or 1.15× transform-limit. Small adjustments of stretcher and compressor gratings allow improvement of compressed pulse duration close to the transform-limit at the expense of small wings appearing in the trace. Experimental trace 2 shows an autocorrelation with 470 femtoseconds FWHM, which is close to the autocorrelation of a transform-limited pulse. FWHM duration of compressed pulses is estimated at 350 femtoseconds (1.05× transform-limited pulse duration). Small wings can be

noted on this trace away from the main peak. To summarize these results, compressed pulses with duration of 370 ± 20 femtoseconds FWHM are obtained, corresponding to 1.1 ± 0.05 times transform-limited pulse duration (determined from the spectrum of compressed pulses). This value is the same as the times-diffraction-limit factor of the pulses delivered by a femtosecond oscillator used in these experiments.

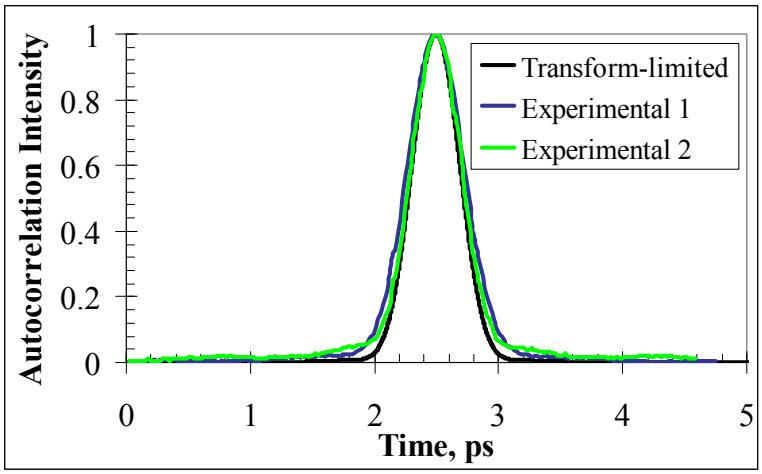

Figure A.19. Measured autocorrelation traces of compressed pulses and calculated autocorrelation of the transform-limited pulse.

These results demonstrate stretching and near-perfect re-compression of femtosecond pulses by chirped volume Bragg gratings. It should also be noted that these results were repeated when stretcher and compressor gratings were interchanged. Another interesting property of chirped volume Bragg gratings that was confirmed experimentally is reciprocity of pulse stretching and compression with respect to the sign of dispersion. Orientations of both CBGs used in this experiment were changed, such that opposite faces of the gratings were used as input faces. In this case the sign of dispersion imposed by the stretcher and compressor are reversed. However, due to the match in magnitude of dispersion between the two CBGs, near-ideal pulse re-compression was achieved in this case, as well.

Chirped Pulse Amplification System

The experiment described in the last sub-section of the previous section has been extended to include a free-space regenerative amplifier after pulse stretching. In this experiment, the same seed oscillator, delivering 155-fs pulses with 7 nm FWHM bandwidth centered around 1028 nm is used. The same CBG, previously described, is used to stretch seed pulses to about 160 picoseconds duration. These pulses are amplified in the regenerative amplifier to various energy levels by varying the number of round-trips and repetition rate of the amplifier. In our experiments we used amplifier repetition rates between 1 and 80 kHz, pulse energy up to 0.5 mJ (limited by the onset of non-linear effects in the amplifying medium) and average power up to 2W. The same CBG, previously described, is used at a small angle of incidence, to compress the amplified pulses with throughput power efficiency exceeding 80%.

Highly-dispersive optical components of the amplifier (mainly isolator and Pockel's cell) result in additional uncompensated dispersion, calculated at about 70000 fs^2. As a result, ideal dispersion compensation is not achieved after amplified pulses are re-compressed by a CBG. In this case, duration of amplified pulses was measured at ~ 950 fs after compression. In our further experiments additional dispersion of amplifier components was compensated by using broadband chirped mirrors in the amplifier. Optimum intra-cavity dispersion was found to be between -2200 and -2500 fs^2/round-trip. In our experiments we used a set of chirped mirrors with total dispersion of -2350 fs^2/round-trip. These mirrors provide good cancellation of dispersion of other amplifier components, such that near-transform-limited pulse duration after CBG compression was achieved in our experiments at various repetition rates from 1 to 80 kHz and pulse energy up to 0.5 mJ.

In our experiments, chirped pulse amplification with pulse stretching and compression by CBGs was demonstrated at a variety of repetition rates from 1 to 80 kHz, pulse energy up to 0.5 mJ and average power up to 2 W. With all possible combinations of these parameters, amplified pulse re-compression to near-transform-limited durations between 320 and 380 fs has been achieved. This spread of pulse duration values is not due to residual dispersion of re-compressed pulses, but is rather determined by the spectrum of amplified pulses, which varies slightly, depending on the repetition rate and pulse energy. Experimental results for two characteristic regimes of CPA system (1 kHz and 80 kHz) are presented below, since other regimes that were investigated during these experiments yielded similar results.

At 80 kHz repetition rate, maximum pulse energy that could be extracted from the amplifier was 25 μJ (2 W average power). Pulse spectrum before and after compressor CBG is shown in Fig. A.20. Measured autocorrelation trace of re-compressed pulses is shown in Fig. A.21. Best fit to this data was obtained assuming $Sech^2$ temporal intensity shape of a pulse, yielding 360 fs FWHM of pulse intensity. Transform-limited pulse duration, calculated from spectrum of Fig. A.20 (after compressor) is 355 fs FWHM. These results demonstrate perfect re-compression of amplified pulses to the near-transform-limited pulse duration.

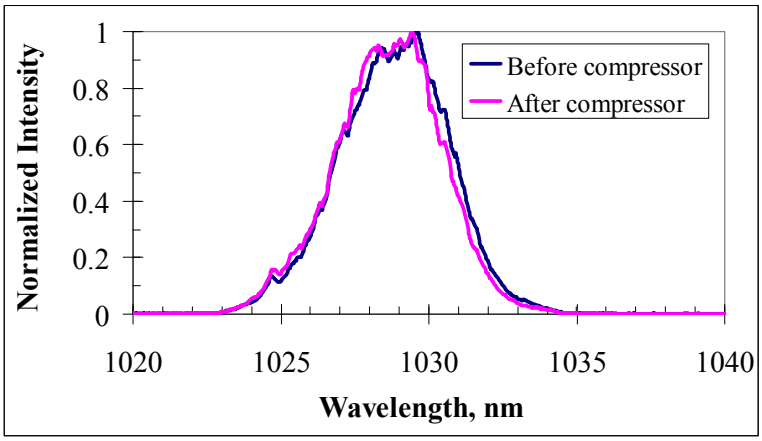

Figure A.20. Spectrum of amplified pulses before and after CBG compressor (25 μJ pulse energy).

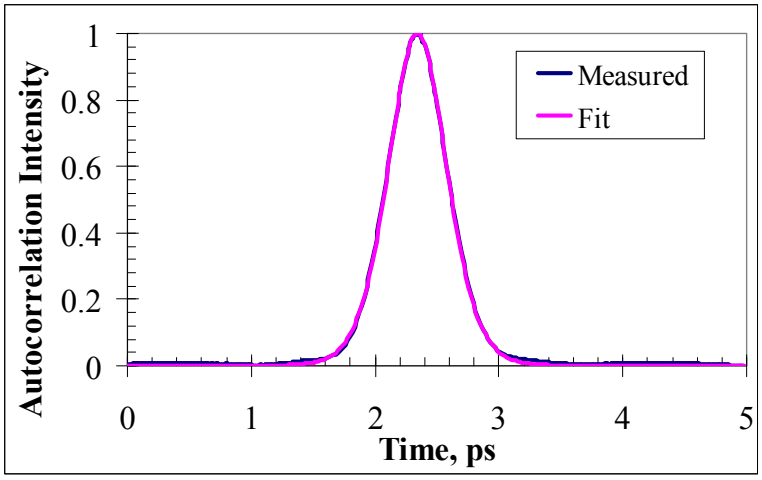

Figure A.21. Measured autocorrelation trace of compressed pulses (25 μJ) and best fit autocorrelation for 360-fs $Sech^2$ pulses.

Higher pulse energies can be achieved from the amplifier at lower repetition rates. At 1 kHz repetition rate, re-compressed pulse duration of 330 fs FWHM was achieved at energies up to 250 μJ per pulse. Fig. A.22 shows an autocorrelation trace of recompressed pulses with 250 μJ energy before compressor (~ 200 μJ after compressor). Best fit is obtained assuming $Sech^2$ temporal intensity shape of a pulse, yielding 330 fs FWHM of pulse intensity. Slightly shorter pulse duration at lower repetition rates is due to slightly broader amplifier gain bandwidth, as a result of higher inversion in the amplification medium (longer storing time).

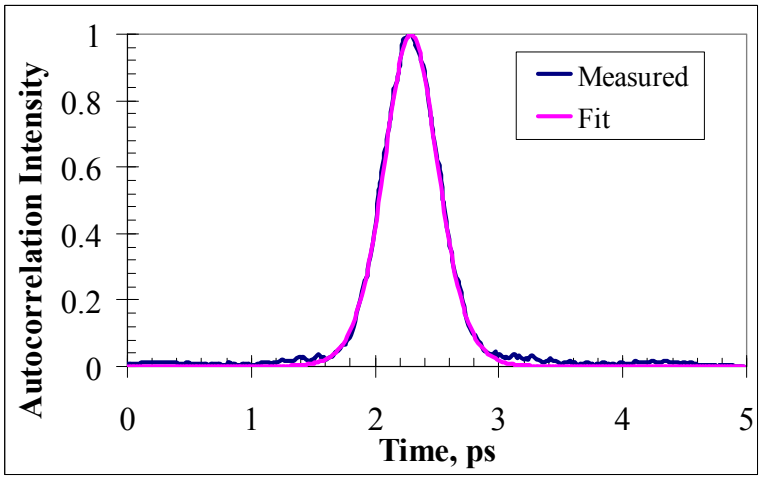

Figure A.22. Measured autocorrelation trace of compressed pulses (250 μJ) and best fit autocorrelation for 330-fs $Sech^2$ pulses.

For pulse energies higher than 250 μJ, duration of output pulse was increased. Best fits to measured autocorrelations assuming $Sech^2$ temporal intensity shape of pulses yielded 360 and 460 fs pulse duration at 390 and 460 μJ pulse energies, respectively. This deterioration of re-compressed pulse duration was explained by examining pulse spectra. Fig. A.23 shows spectra of 460-μJ pulses before and after compression. Some modulation can be noted on pulse spectrum before the compressor. This modulation is explained by the onset of non-linear effects, particularly self phase modulation (SPM) in the amplifying medium. These effects set a limit on pulse energy that can be extracted from the amplifier in the present configuration at ~ 500 μJ to avoid amplifier damage. Further development of spectral modulation and other modifications are observed in pulse spectrum after compression. These effects can be explained by SPM and other non-linear effects in the volume of compressor CBG. Specifically, the onset of white light generation, another non-linear effect, can be noticed on the inset of Fig. A.23. Spectral components at wavelength 1020-1023 nm are generated in a compressed pulse that is reflected by the grating. These spectral components are not present in the spectrum of incident amplified pulse. Moreover, these wavelengths are located outside of the reflection band of the compressor grating (Fig. A.18), and cannot be directly reflected by the compressor CBG. It is clear that these spectral components are generated in the volume of the grating, when pulse is being reflected and compressed by the CBG.

To mitigate non-linear effects and achieve pulse compression to near-transform-limited duration, beam size on the grating should be increased. In the experiment described above, beam diameter on the grating was ~ 1.5 mm $FWe^{-2}M$, peak power of a compressed pulse exiting ~ 1.3 GW, and corresponding power density ~ 70 GW/cm^2. By increasing beam diameter to ~ 2.3 mm $FWe^{-2}M$, peak power density is decreased to ~ 30 GW/cm^2. In this case, non-linear effects in

compressor CBG are avoided and re-compression to near-transform-limited pulse duration was achieved up to 500 μJ, the maximum pulse energy available from the amplifier. Fig. A.24 shows an autocorrelation trace of recompressed pulses with 500 μJ energy before compressor (~ 400 μJ after compressor). Best fit assuming $Sech^2$ temporal intensity shape of a pulse yields pulse duration of 345 fs FWHM.

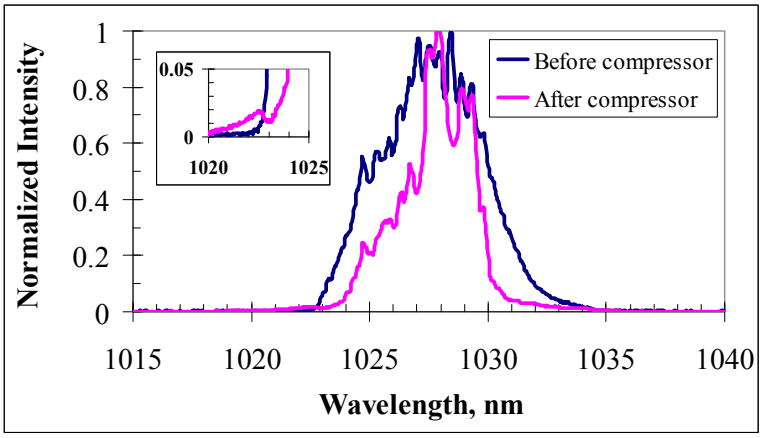

Figure A.23. Spectrum of amplified pulses before and after CBG compressor (460 μJ pulse energy). Inset – close-up of the main graph, showing an onset of white light generation in the volume of pulse-compressing CBG.

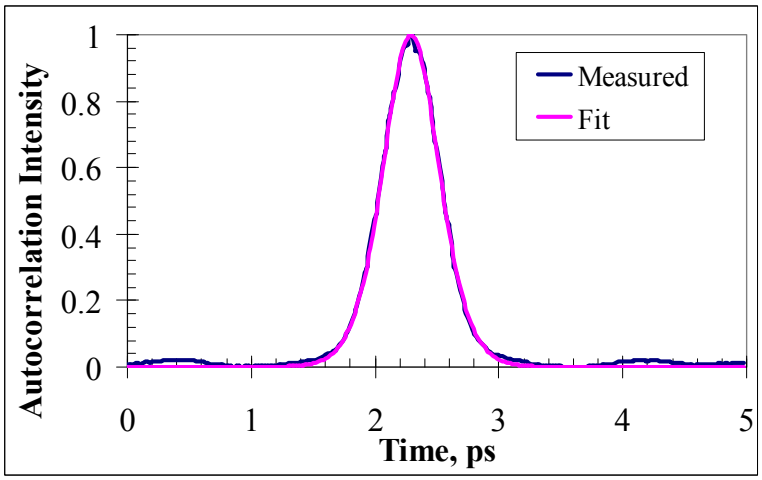

Figure A.24. Measured autocorrelation trace of compressed pulses (500 μJ) and best fit autocorrelation for 345-fs $Sech^2$ pulses.

It was shown experimentally that stretcher and compressor VBGs in the described CPA system can be interchanged. Also, orientations of both CBGs can be changed, such that opposite

faces of the gratings are used as input faces. In this case the sign of dispersion imposed by the stretcher and compressor are reversed. In all cases, perfect recompression of amplified pulses to near-transform-limited duration was experimentally demonstrated at various amplifier repetition rates and pulse energies up to 500 μJ. No influence of the sign of stretcher (compressor) dispersion on duration of re-compressed pulses was observed.

To the best of author's knowledge this is the first time that non-linear effects are observed in a pulse-compressing CBG, therefore no explanation of which effects dominate and how non-linearities are developed exists. Some description of non-linear properties of PTR glass can be found in [147,168], however a particular case of pulse-compressing CBGs in PTR-glass is significantly different from bulk PTR glass, due to highly non-uniform power density distribution inside the sample. Development of a rigorous model of high-power chirped pulse propagation inside PTR-glass CBGs will help better understand limitations of using these elements for pulse compression. Although development of such model it is outside of the scope of this work, the following empirical suggestion can be made, based on the results of presented experiments. As pulse energy from femtosecond amplifiers is scaled into the mJ range, chirped volume Bragg gratings with apertures on the order of 1 cm and 3 cm will be required to efficiently compress 300-fs and 30-fs pulses (respectively) to near-transform-limited duration.

To summarize experimental results presented in this Appendix, CPA system using CBG-based stretcher and compressor has been demonstrated. Efficient re-compression of amplified pulses to near-transform-limited duration on the order of 350 fs is achieved at repetition rates from 1 to 80 kHz, average power up to 2 W and pulse energy up to 500 μJ. No influence of the sign of stretcher (compressor) dispersion on duration of re-compressed pulses is observed.

LIST OF REFERENCES

[1] O. Andrusyak, I. Ciapurin, V. Rotar, A. Sevian, G. Venus, and L. Glebov. "Dense spectral beam combining with volume Bragg gratings in PTR glass". Proc. of Nineteenth Annual Solid State and Diode Laser Technology Review, BC-3 (2006).

[2] A. Sevian, O. Andrusyak, I. Ciapurin, G. Venus, and L. Glebov, "Spectral beam combining with volume Bragg gratings: Cross-talk analysis and optimization schemes," Proc. SPIE 6216, 62160V (2006).

[3] O. Andrusyak, I. Ciapurin, V. Smirnov, G. Venus, and L. Glebov. "Spectral beam combining of fiber lasers with increased channel density". Proc. SPIE 6453, 64531L (2007).

[4] A. Sevian, O. Andrusyak, I. Ciapurin, G. Venus, and L. Glebov. "Ultimate efficiency of multi-channel spectral beam combiners by means of volume Bragg gratings". Proc. SPIE 6453, 64530R (2007).

[5] O. Andrusyak, I. Ciapurin, A. Sevian, V. Smirnov, G. Venus, L. Glebov, "Power Scaling of Laser Systems Using Spectral Beam Combining with Volume Bragg Gratings in PTR Glass," Conference on Lasers and Electro-Optics, CLEO 2007, OSA Technical Digest, JTuA85 (2007).

[6] O. Andrusyak, V. Smirnov, G. Venus, and L. Glebov. "Narrow-band volume Bragg gratings in PTR glass under high-power CW laser radiation." Proc. of Twentieth Annual Solid State and Diode Laser Technology Review, P-1 (2007).

[7] O. Andrusyak, V. Rotar, A. Sevian, V. Smirnov, G. Venus, and L. Glebov. "Spectral beam combining by stack of volume Bragg gratings in PTR glass." Proc. of Twentieth Annual Solid State and Diode Laser Technology Review, BC2-2 (2007).

[8] A. Sevian, O. Andrusyak, I. Ciapurin, V. Smirnov, G. Venus, and L. Glebov, "Efficient power scaling of laser radiation by spectral beam combining," Opt. Lett. 33, 384-386 (2008).

[9] A. Sevian, O. Andrusyak, I. Ciapurin, V. Smirnov, G. Venus, and L. Glebov, "Efficient power scaling of laser radiation by spectral-beam combining: erratum," Opt. Lett. 33, 760-760 (2008).

[10] O. Andrusyak, I. Ciapurin, V. Smirnov, G. Venus, N. Vorobiev, and L. Glebov, "External and common-cavity high spectral density beam combining of high power fiber lasers," Proc. SPIE 6873, 687314 (2008).

[11] O. Andrusyak, D. Drachenberg, V. Smirnov, G. Venus, and L. Glebov, "Fiber laser system with kW-level spectrally-combined output," Proc. of 21-st Annual Solid State and Diode Laser Technology Review (2008).

[12] N. Vorobiev, O. Andrusyak, V. Smirnov, G. Venus and L. Glebov, "Spectral beam combining of fiber lasers with automatic wavelength control," Proc. of 21-st Annual Solid State and Diode Laser Technology Review (2008).

[13] O. Andrusyak, V. Smirnov, G. Venus, and L. Glebov, “Spectral Beam Combining of Fiber Lasers by Volume Bragg Gratings,” in Frontiers in Optics, OSA Technical Digest (CD) (Optical Society of America, 2008), paper FWG3 (2008).
[14] O. Andrusyak, V. Smirnov, G. Venus, N. Vorobiev, and L. Glebov, “Applications of volume Bragg gratings for spectral control and beam combining of high power fiber lasers,” Proc. SPIE 7195, 71951Q (2009).
[15] O. Andrusyak, V. Smirnov, G. Venus, V. Rotar, and L. Glebov, “Spectral Combining and Coherent Coupling of Lasers by Volume Bragg Gratings,” Selected Topics in Quantum Electronics, IEEE Journal of, March/April 2009, 10 pages (in print, published on-line 10 Feb 2009).
[16] O. Andrusyak, V. Smirnov, G. Venus and L. Glebov, “Beam combining of lasers with high spectral density using volume Bragg gratings,” Opt. Comm., 4 pages (accepted 7 Mar 2009).
[17] O. Andrusyak, M. Bubelnik, J. Mares, T. McGovern, and C. W. Siders, “Single-pulse and burst-mode ablation of gold films measured by quartz crystal microbalance,” Proc. SPIE 5647, 61 (2005).
[18] M. Fisher, C. Siders, E. Johnson, O. Andrusyak, C. Brown, and M. Richardson, “Control of filamentation for enhancing remote detection with laser induced breakdown spectroscopy”, Proc. SPIE 6219, 621907 (2006).
[19] C. Siders, J. Bullington, O. Andrusyak, “Optical pulse stretching and compression,” World patent WO/2005/018062. 2005 Feb 24. Int. Cl. A61B 18/20; A61B 17/00; A61B 19/00 (2005).
[20] O. Andrusyak, L. Canioni, I. Cohanoschi, E. Rotari, V. Smirnov, G. Venus, L. Glebov, “Dispersion characterization of chirped volume Bragg gratings using a non-linear cross-correlation technique,” 6 pages (prepared for Applied Optics).
[21] O. Andrusyak, L. Canioni, I. Cohanoschi, E. Rotari, V. Smirnov, G. Venus, L. Glebov, “Stretching and compression of near-infrared ultrashort pulses by chirped volume Bragg gratings ,” 4 pages (prepared for Optics Letters).
[22] O. Andrusyak, L. Canioni, M. Delaigue, I. Cohanoschi, E. Rotari, V. Smirnov, G. Venus, L. Glebov, “Compression of 0.5-mJ amplified laser pulses to 350-fs transform-limited duration by a chirped volume Bragg grating,” 6 pages (prepared for Optics Express).
[23] L. Glebov, V. Smirnov, O. Andrusyak, L. Canioni. US Patent Application. (prepared).
[24] T.H. Maiman, “Stimulated Optical Radiation in Ruby,” *Nature* **187**, 493-494 (1960).
[25] F. J. McClung and R. W. Hellwarth, "Giant Optical Pulsations from Ruby," *J. Appl. Phys.* **33**, 828 (1962).
[26] K. Gürs, "Beats and modulation in optical ruby laser," in Quantum Electronics III (Columbia University Press, New York 1964).
[27] H. Statez, C.L. Tang, "Zeeman effect and nonlinear interactions between oscillationg laser modes", in Quantum Electronics III (Columbia University Press, New York 1964).
[28] M. DiDomenico, "Small-signal analysis of internal (coupling type) modulation of lasers," J. Appl. Phys. 35, 2870-2876 (1964).
[29] A. Yariv, "Internal modulation in multimode laser oscillators," J. Appl. Phys. 36, 388-391 (1965).
[30] L.E. Hargrove, R.L. Fork, M.A. Pollack, "Locking of He-Ne laser modes induced by synchronous intracavity modulation," Appl. Phys. Lett. 5, 4-5 (1964).

[31] H.W. Mocker, R.J. Collins, "Mode competition and self-locking effects in a Q-switched ruby laser," Appl. Phys. Lett. 7, 270-273 (1965).
[32] F. P. W. Schmidt, F. P. Schäfer: "Self-mode-locking of dye-lasers with saturable absorbers," Phys. Lett. 26A, 258-259 (1968).
[33] E.P. Ippen, C.V. Shank, A. Dienes: "Passive mode locking of the cw dye laser," Appl. Phys. Lett. 21, 348-350 (1972).
[34] G. Kachen, L. Steinmetz, and J. Kysilka, "Selection and amplification of a single mode-locked pulse," Appl. Phys. Lett. 13, 229 (1968).
[35] E. M. Campbell, J. T. Hunt, E. S. Bliss, D. R. Speck, and R. P. Drake, "Nova experimental facility (invited)," Rev. Sci. Instrum. 57, 2101 (1986).
[36] C. Bibeau, D. R. Speck, R. B. Ehrlich, C. W. Laumann, D. T. Kyrazis, M. A. Henesian, J. K. Lawson, M. D. Perry, P. J. Wagner, and T. L. Weiland, "Power, energy, and temporal performance of the Nova laser facility with recent improvements to the amplifier system," Appl. Opt. 31, 5799-5809 (1992).
[37] D. Strickland and G. Morou, "Chirped pulse amplification," Opt. Comm. 56, 219 (1985).
[38] Maine, P.; Strickland, D.; Bado, P.; Pessot, M.; Mourou, G., "Generation of ultrahigh peak power pulses by chirped pulse amplification," Quantum Electronics, IEEE Journal of, vol.24, no.2, pp.398-403 (1988).
[39] M. D. Perry and G. Mourou, "Terawatt to Petawatt Subpicosecond Lasers," Science 264 (5161), 917 (1994).
[40] Patel, C. K. N., "Continuous-wave laser action on vibrational-rotational transitions of CO2". Physical Review 136 (5A), A1187–A1193 (1964).
[41] E. T. Gerry, "Gasdynamic lasers," IEEE Spectrum, vol. 7, pp. 51-58 (1970).
[42] L. R. Migliore, *Encyclopedia of Optical Engineering* (Dekker, New York, 2003), p. 880.
[43] J. Waypa, J.G. Gish, "Advanced High-Energy Laser Technology," Northrop Grumman Mission Systems' Technology Review Journal, Vol. 8, No. 2, Fall/Winter 2000, pp. 69-78.
[44] Hall, Robert N.; G. E. Fenner, J. D. Kingsley, T. J. Soltys, and R. O. Carlson, "Coherent Light Emission From GaAs Junctions," Physical Review Letters 9 (9), 366–369 (1962).
[45] Robert Steele, "Laser marketplace 2008: Diode lasers track long-term trend," Laser Focus World 44 (2) (2008).
[46] Kathy Kincade, Stephen Anderson, "Laser marketplace 2008: Innovation opens the door for next wave of success," Laser Focus World 44 (1) (2008).
[47] Andre Timmermann et al., "Next generation high-brightness diode lasers offer new industrial applications," Proc. SPIE 6876, 68760U (2008).
[48] V. Gapontsev et al., "8xx - 10xx nm highly efficient single emitter pumps," Proc. SPIE 6876, 68760I (2008).
[49] R. Ostendorf et al., "10 W high-efficiency high-brightness tapered diode lasers at 976 nm," Proc. SPIE 6876, 68760H (2008).
[50] C. Wessling et al., "50 W passively cooled, fiber coupled diode laser at 976 nm for pumping fiber lasers using 100 μm fiber bundles," Proc. SPIE 6876, 687614 (2008).
[51] D. M. Grasso et al., "Fiber-coupled laser systems for high-power and high-brightness applications," Proc. SPIE 6552, 655211 (2007).
[52] V. Krause and A. Koesters, "Brilliant high-power diode lasers based on broad area lasers," Proc. SPIE 6876, 687615 (2008).

[53] Hanxuan Li et al., "High-efficiency, high-power diode laser chips, bars, and stacks," Proc. SPIE 6876, 68760G (2008).
[54] J. Dellunde, A. Valle, L. Pesquera, and K. A. Shore, "Transverse-mode selection and noise properties of external-cavity vertical-cavity surface-emitting lasers including multiple-reflection effects," J. Opt. Soc. Am. B 16, 2131-2139 (1999).
[55] George Venus et al., "Volume Bragg semiconductor lasers with near diffraction limited divergence," Proc. of SPIE 6216, 621602, (2006).
[56] A. Gourevitch, G. Venus, V. Smirnov, and L. Glebov, "Efficient pumping of Rb vapor by high-power volume Bragg diode laser," Opt. Lett. 32, 2611-2613 (2007).
[57] B. L. Volodin, S. V. Dolgy, E. D. Melnik, E. Downs, J. Shaw, and V. S. Ban, "Wavelength stabilization and spectrum narrowing of high-power multimode laser diodes and arrays by use of volume Bragg gratings," Opt. Lett. 29, 1891-1893 (2004).
[58] Patrick Friedmann et al., "5 W frequency stabilized 976 nm tapered diode lasers," Proc. SPIE 6876, 68761J (2008).
[59] A. Gourevitch, G. Venus, V. Smirnov, D. A. Hostutler, and L. Glebov, "Continuous wave, 30 W laser-diode bar with 10 GHz linewidth for Rb laser pumping," Opt. Lett. 33, 702-704 (2008).
[60] Y. Zheng and H. Kan, "Effective bandwidth reduction for a high-power laser-diode array by an external-cavity technique," Opt. Lett. 30, 2424-2426 (2005).
[61] C. Martin Stickley; Mark E. Filipkowski; Enrique Parra; Marie Sandrock, "High Power Laser Diodes and Applications to Direct Diode HELs," Lasers and Electro-Optics Society, LEOS 2006. 19th Annual Meeting of the IEEE, pp.468-469 (2006).
[62] R. L. Byer, “Diode laser-pumped solid-state lasers”, Science 239, 742 (1988).
[63] D. W. Hughes, “Laser diode pumped solid-state lasers”, J. Phys. D: Appl. Phys. 25, 563 (1992).
[64] D. C. Hanna and W. A. Clarkson, “A review of diode-pumped lasers”, in Advances in Lasers and Applications (eds. D. M. Finlayson and B. Sinclair), Taylor & Francis, London (1999).
[65] W. Koechner, “Thermal lensing in a Nd:YAG laser rod”, Appl. Opt. 9 (11), 2548 (1970).
[66] J. Steffen et al., “Fundamental mode radiation with solid-state lasers”, IEEE J. Quantum Electron. QE-8 (2), 239 (1972).
[67] N. Hodgson et al., “High power TEM00 mode operation of diode-pumped solid-state lasers”, Proc. SPIE 3611, 119 (1999).
[68] S. Chénais et al., “Thermal lensing in diode-pumped ytterbium lasers - Part I: theoretical analysis and wavefront measurements”, IEEE J. Quantum Electron. 40 (9), 1217 (2004).
[69] H. J. Eichler et al., “Thermal lensing and depolarization in a highly pumped Nd:YAG laser amplifier”, J. Phys. D: Appl. Phys. 26, 1884 (1993).
[70] J. D. Foster and L. M. Osterink, J. Appl. Phys. 41, 3656 (1970).
[71] P. P. Sorokin and M. J. Stevenson, “Stimulated infrared emission from trivalent uranium”, Phys. Rev. Lett. 5 (12), 557 (1960).
[72] R. L. Aggarwal et al., “Measurement of thermo-optic properties of Y3Al5O12, LuAl5O12, YAlO3, LiYF4, LiLuF4, BaY2F8, KGd(WO4)2, and KY(WO4)2 laser crystals in the 80–300 K temperature range”, J. Appl. Phys. 98, 103514 (2005).
[73] Brown, D.C., "Ultrahigh-average-power diode-pumped Nd:YAG and Yb:YAG lasers," Quantum Electronics, IEEE Journal of , vol.33, no.5, pp.861-873, 1997.

[74] P. A. Schulz and S. R. Henion, “Liquid-nitrogen-cooled Ti:Al2O3 laser,” IEEE J. Quantum Electron., vol. 27, no. 4, pp. 1039–1047, Apr. 1991.
[75] D. C. Brown, “Nonlinear thermal distortion in YAG rod amplifiers,” IEEE J. Quantum Electron., vol. 34, no. 12, pp. 2383–2392, Dec. 1998.
[76] T. Y. Fan et al., “Cryogenic Yb3+-doped solid-state lasers”, IEEE J. Sel. Top. Quantum Electron. 13 (3), 448 (2007).
[77] K. Ueda; N. Uehara, “Laser-diode-pumped solid state lasers for gravitational wave antenna”, Proc. SPIE 1837, 336–345 (1993).
[78] K. Contag et al., "Multi-hundred watt CW diode pumped Yb:YAG thin disc laser,” Proc. SPIE 2986, p.23 (1997).
[79] Stewen, C.; Contag, K.; Larionov, M.; Giesen, A.; Hugel, H., "A 1-kW CW thin disc laser," Selected Topics in Quantum Electronics, IEEE Journal of , vol.6, no.4, pp. 650-657, Jul/Aug 2000.
[80] M. Karszewski, et al., “100 W TEM operation of Yb :YAG thin disc laser with high efficiency,” in OSA Trends in Optics and Photonics, Advanced Solid-State Lasers, W. A. Bosenberg and M. M. Frejer, Eds. Washington, DC: Opt. Soc. Amer., vol. 19, p. 125 (1998).
[81] Giesen, A.; Speiser, J., "Fifteen Years of Work on Thin-Disk Lasers: Results and Scaling Laws," *Selected Topics in Quantum Electronics, IEEE Journal of* , vol.13, no.3, pp.598-609, May-june 2007.
[82] TRUMPF Laser Division, http://www.trumpf-laser.com/ (accessed March 8, 2009).
[83] E. Snitzer, “Proposed fiber cavities for optical masers”, J. Appl. Phys. 23 (1), 36 (1961).
[84] A. Tünnermann, T. Schreiber, F. Röser, A. Liem, S. Höfer, H. Zellmer, S. Nolte, and J. Limpert, “The renaissance and bright future of fibre lasers,” J. Phys. B 38, 681 (2005).
[85] Michel J. F. Digonnet, Rare-earth-doped Fiber Lasers and Amplifiers (Marcel Dekker, 2001).
[86] Paschotta, R.; Nilsson, J.; Tropper, A.C.; Hanna, D.C., "Ytterbium-doped fiber amplifiers," Quantum Electronics, IEEE Journal of , vol.33, no.7, pp.1049-1056, Jul 1997.
[87] A. Galvanauskas, “Ultrashort-pulse fiber amplifiers”, in Ultrafast Lasers: Technology and Applications (eds. M. Fermann, A. Galvanauskas, G. Sucha), Marcel Dekker, New York (2002), Chapter 4, pp. 155-218.
[88] J. C. Knight, "Photonic crystal fibers and fiber lasers (Invited)," J. Opt. Soc. Am. B 24, 1661-1668 (2007).
[89] L. Dong, W. H. Loh, J. E. Caplen, J. D. Minelly, K. Hsu, and L. Reekie, "Efficient single-frequency fiber lasers with novel photosensitive Er/Yb optical fibers," Opt. Lett. 22, 694-696 (1997).
[90] Valentin Gapontsev and William Krupke, "Fiber lasers grow in power," Laser Focus World 38 (8) (2002).
[91] D. Walton, S. Gray, J. Wang, M. Li, X. Chen, A. Liu, L. Zenteno, and A. Crowley, “Kilowatt - Level, Narrow - Linewidth Capable Fibers and Lasers,” Proc. of SPIE 6453 (2007).
[92] J. D. Hansryd, “Increase of the SBS threshold in a short highly nonlinear fiber by applying a temperature distribution,” J. Lightwave Tech. 19, 1691-1697 (2001).
[93] Chi-Hung Liu, Almantas Galvanauskas, Victor Khitrov, Bryce Samson, Upendra Manyam, Kanishka Tankala, David Machewirth, and Stefan Heinemann, "High-power

single-polarization and single-transverse-mode fiber laser with an all-fiber cavity and fiber-grating stabilized spectrum," Opt. Lett. 31, 17-19 (2006).
[94] P. S. J. Russell, “Photonic-Crystal Fibers,” J. Lightwave Tech. 24, 4729-4749 (2006).
[95] J. C. Baggett, T. M. Monro, K. Furusawa, and D. J. Richardson, “Comparative study of large-mode holey and conventional fibers,” Opt. Lett. 26, 1045-1047 (2001).
[96] G. Bonati, H. Voelckel, T. Gabler, U. Krause, A. Tünnermann, J. Limpert, A. Liem, T. Schreiber, S. Nolte, and H. Zellmer, "1.53 kW from a single Yb-doped photonic crystal fiber laser," Photonics West, Late Breaking Developments, Session 5709-2a (The International Society for Optical Engineering , 2005).
[97] Y. Jeong, J. Sahu, D. Payne, and J. Nilsson, "Ytterbium-doped large-core fiber laser with 1.36 kW continuous-wave output power," Opt. Express 12, 6088-6092 (2004).
[98] J. Limpert, F. Röser, S. Klingebiel, T. Schreiber, C. Wirth, T. Peschel, R. Eberhardt, and A. Tünnermann, “The Rising Power of Fiber Lasers and Amplifiers,” IEEE J. Sel. Top. Quantum Eletron. 13, 537 (2007).
[99] S. Gray, A. Liu, D. T. Walton, J. Wang, M. -J. Li, X. Chen, A. B. Ruffin, J. A. DeMeritt, and L. A. Zenteno, "502 Watt, single transverse mode, narrow linewidth, bidirectionally pumped Yb-doped fiber amplifier," Opt. Express 15, 17044-17050 (2007).
[100] D. Gapontsev, “6 kW CW Single Mode Ytterbium Fiber Laser in All-Fiber Format,” in Solid State and Diode Laser Technology Review (Albuquerque, 2008).
[101] Jay W. Dawson, Michael J. Messerly, Raymond J. Beach, Miroslav Y. Shverdin, Eddy A. Stappaerts, Arun K. Sridharan, Paul H. Pax, John E. Heebner, Craig W. Siders, and C.P.J. Barty, "Analysis of the scalability of diffraction-limited fiber lasers and amplifiers to high average power," Opt. Express 16, 13240-13266 (2008).
[102] Valentin P. Gapontsev, “Recent progress on high-power CW fiber lasers,” in Fiber Lasers VI: Technology, Systems, and Applications, 7195 (San Jose, CA 2009).
[103] T. Y. Fan, “Laser beam combining for high-power, high-radiance sources”, IEEE J. Sel. Top. Quantum Electron. 11 (3), 567 (2005).
[104] D. Y. Shen, J. K. Sahu, and W. A. Clarkson, "Highly efficient Er,Yb-doped fiber laser with 188W free-running and > 100W tunable output power," Opt. Express 13, 4916-4921 (2005).
[105] R. Mellish, N. P. Barry, S. C. Hyde, R. Jones, P. M. W. French, J. R. Taylor, C. J. van der Poel, and A. Valster, "Diode-pumped Cr:LiSAF all-solid-state femtosecond oscillator and regenerative amplifier," Opt. Lett. 20, 2312- (1995).
[106] J. R. Leger, “External methods of phase locking and coherent beam addition of diode lasers,” in Surface Emitting Semiconductor Lasers and Arrays, G. A. Evans and J. M. Hammer, Eds. Boston, MA: Academic, pp. 379–433 (1993).
[107] S. R. Chinn, “Review of edge-emitting coherent laser arrays,” in Surface Emitting Semiconductor Lasers and Arrays, G. A. Evans and J. M. Hammer, Eds. Boston, MA: Academic, pp. 9–70 (1993).
[108] D. Botez, “Monolithic phase-locked semiconductor laser arrays,” in Diode Laser Arrays, D. Botez and D. R. Scrifres, Eds. Cambridge, U.K.: Cambridge Univ. Press, pp. 1–67 (1994).
[109] D. F. Welch and D. G. Mehuys, “High-power coherent, semiconductor laser, master oscillator power amplifiers and amplifier arrays,” in Diode Laser Arrays, D. Botez and D. R. Scrifres, Eds. Cambridge, U.K.: Cambridge Univ. Press, pp. 72–122 (1994).

[110] I. S. Goldobin, N. N. Evtikhiev, A. G. Plyavenek, and S. D. Yakubovich, “Phase-locked integrated arrays of injection lasers,” Sov. J. Quantum Electron., vol. 19, pp. 1261–1284 (1989).
[111] Rice, R. R., Davis, J. A., Whitely, J. S., Hollister, J. H., and Ruggieri, N. F., “Coherent Fiber MOPA,” Presented at 14th Annual Solid State and Diode Laser Technology Review, Sean Ross, ed., Albuquerque, NM (2001).
[112] Augst, S.J., Fan, T. Y., and Sanchez, A. D., “Coherent Beam Combining and Phase Noise Measurements of Yt fiber Amplifiers,” Opt. Lett. 29, 474-476 (2004).
[113] S. J. Augst, J. K. Ranka, T. Y. Fan, and A. Sanchez, "Beam combining of ytterbium fiber amplifiers (Invited)," J. Opt. Soc. Am. B 24, 1707-1715 (2007).
[114] Shay, T. M., Benham, V., Baker, J. T., Ward, B., Sanchez, A. D., Culpepper, M. A., Pilkington, D., Spring, J., Nelsen, D., and Lu, C. A., “First Experimental Demonstration of Self-Synchronous Phase Locking of an Optical Array,” Opt. Express, 14, 12022-12027 (2006).
[115] Shay, T. M., Baker, J. T., Sanchez, A. D., Robin, C. A., Vergien, C. L., Zerinque, C., Gallant, D., Lu, C. A., and Bronder, T. J. , “Electronic Phasing of High Power Fiber Amplifier Arrays,” Proceedings of the IEEE Lasers and Electro-Optics Society Annual Meeting 2008, pg. 783 (2008).
[116] T. M. Shay, J. T. Baker, A. D. Sanchez, C. A. Robin, C. L. Vergien, C. Zeringue, D. Gallant, Chunte A. Lu, Benjamin Pulford, T. J. Bronder, and Arthur Lucero, “High-power phase locking of a fiber amplifier array,” Proc. SPIE 7195, 71951M (2009).
[117] T. H. Loftus, A. M. Thomas, M. Norsen, J. Minelly, P. Jones, E. Honea, S. A. Shakir, S. Hendow, W. Culver, B. Nelson, and M. Fitelson, "Four-Channel, High Power, Passively Phase Locked Fiber Array," in Advanced Solid-State Photonics, OSA Technical Digest Series (CD), paper WA4 (2008).
[118] J. Anderegg, S. Brosnan, E. Cheung, P. Epp, D. Hammons, H. Komine, M. Weber, and M. Wickham, Proc. SPIE 6102, 61020U-1 (2006).
[119] Eric C. Cheung, James G. Ho, Gregory D. Goodno, Robert R. Rice, Josh Rothenberg, Peter Thielen, Mark Weber, and Michael Wickham, "Diffractive-optics-based beam combination of a phase-locked fiber laser array," Opt. Lett. 33, 354-356 (2008).
[120] K. Nosu, H. Ishio, and K. Hashimoto, “Multireflection optical multi/demultiplexer using interference filters,” Electron. Lett., vol. 15, pp. 414–415, (1979).
[121] Regelskis, K.; Kai-Chung Hou; Raciukaitis, G.; Galvanauskas, A., "Spatial-dispersion-free spectral beam combining of high power pulsed Yb-doped fiber lasers," Conference on Lasers and Electro-Optics and Conference on Quantum Electronics and Laser Science. CLEO/QELS 2008 (2008).
[122] P. O. Minott and J. B. Abshire, “Grating rhomb diode laser power combiner,” Proc. SPIE vol. 756, pp. 38–48 (1987).
[123] J. A. R. Rall, P. L. Spadin, R. K. Zimmerman, and W. Maynard, “Test results of a diffraction grating beam combiner,” Free-Space Laser Commun. Technol., vol. 1218, pp. 264–275 (1990).
[124] C. C. Cook and T. Y. Fan, “Spectral beam combining of Yb-doped fiber lasers in an external cavity,” in OSA Trends in Optics and Photonics, Vol. 26, Adv. Solid-State Lasers, M. M. Fejer, H. Injeyan, and U. Keller, Eds. Washington, DC: Optical Society of America, pp. 163–166 (1999).

[125] V. Daneu, A. Sanchez, T.Y. Fan, H. K. Choi,G.W. Turner, and C. C. Cook, “Spectral beam combining of a broad-stripe diode laser array in an external cavity,” Opt. Lett., vol. 25, pp. 405–407 (2000).
[126] Bochove, E.J., "Theory of spectral beam combining of fiber lasers," Quantum Electronics, IEEE Journal of , vol.38, no.5, pp.432-445 (2002).
[127] Huang, R. K.; Chann, B.; Missaggia, L. J.; Donnelly, J. P.; Harris, C. T.; Turner, G. W.; Goyal, A. K.; Fan, T. Y.; Sanchez-Rubio, A., "High-Brightness Wavelength Beam Combined Semiconductor Laser Diode Arrays," Photonics Technology Letters, IEEE , vol.19, no.4, pp.209-211 (2007).
[128] F. Röser, S. Klingebiel, A. Liem, T. Schreiber, S. Höfer, J. Limpert, T. Peschel, R. Eberhard, and A. Tünnermann, “Spectral combining of fiber lasers,” in Fiber Lasers III, A. J. Brown, J. Nilsson, D. J. Harter, and A. Tünnermann, eds., Proc. SPIE 6102, 61020T (2006).
[129] S. Klingebiel, F. Röser, B. Ortaç, J. Limpert, and A. Tünnermann, "Spectral beam combining of Yb-doped fiber lasers with high efficiency," J. Opt. Soc. Am. B 24, 1716-1720 (2007).
[130] S. J. Augst, A. K. Goyal, R. L. Aggarwal, T. Y. Fan, and A. Sanchez, “Wavelength beam combining of ytterbium fiber lasers,” Opt. Lett. 28, 331–333 (2003).
[131] S. J. Augst, J. K. Ranka, T. Y. Fan, and A. Sanchez, "Beam combining of ytterbium fiber amplifiers," J. Opt. Soc. Am. B 24, 1707-1715 (2007).
[132] T. H. Loftus, A. Liu, P. R. Hoffman, A. M. Thomas, M. Norsen, R. Royse, and E. Honea, "522 W average power, spectrally beam-combined fiber laser with near-diffraction-limited beam quality," Opt. Lett. 32, 349-351 (2007).
[133] C. Wirth, O. Schmidt, I. Tsybin, T. Schreiber, T. Peschel, F. Brückner, T. Clausnitzer, J. Limpert, R. Eberhardt, A. Tünnermann, M. Gowin, E. ten Have, K. Ludewigt, and M. Jung, "2 kW incoherent beam combining of four narrow-linewidth photonic crystal fiber amplifiers," Opt. Express 17, 1178-1183 (2009).
[134] I.V. Ciapurin, L.B. Glebov, L.N. Glebova, V.I. Smirnov, E.V. Rotari, "Incoherent combining of 100-W Yb-fiber laser beams by PTR Bragg grating. In Advances in Fiber Devices," L. N. Durvasula, Editor, Proceedings of SPIE 4974, 209-219 (2003).
[135] Loftus, T.H.; Thomas, A.M.; Hoffman, P.R.; Norsen, M.; Royse, R.; Anping Liu; Honea, E.C., "Spectrally Beam-Combined Fiber Lasers for High-Average-Power Applications," Selected Topics in Quantum Electronics, IEEE Journal of , vol.13, no.3, pp.487-497, (2007).
[136] G. P. Agrawal, Nonlinear Fiber Optics, 3rd ed. (Academic, 2001).
[137] H. Kogelnik, “Coupled wave theory for thick hologram gratings,” Bell Syst. Tech. J. 48, 2909 (1969).
[138] M. W. McCall, Math. and Comp. Modeling 34, 1483 (2001).
[139] M. R. Chatterjee and D. D. Reagan, Opt. Eng. 38(7), 1113 (1999).
[140] T. Erdogan, Opt. Comm. 157, 249 (1998).
[141] J. Zhao, P. Yeh, M. Khoshnevisan, and I. McMichael, J. Opt. Soc. Am. B 17(6), 898 (2000).
[142] M. G. Moharam, T. K. Gaylord, J. Opt. Soc. Am. 71, 811 (1981).
[143] D. Yevick, L. Thylen, J. Opt. Soc. Am. 72, 1084 (1982).
[144] I.Ciapurin, L.Glebov, and V.Smirnov. “Modeling of Gaussian Beam Diffraction on Volume Bragg Gratings in PTR Glass." Practical Holography XIX: Materials and

Applications. Eds: T.H. Jeong, H. Bjelkhagen. Proceedings of SPIE 5742, pp. 183-194 (2005).
[145] Igor V. Ciapurin, Leonid B. Glebov, and Vadim I. Smirnov, "Spectral combining of high-power fiber laser beams using Bragg grating in PTR glass," Proc. SPIE 5335, p. 116 (2004).
[146] O.M. Efimov, L.Glebov, V.Smirnov. "High efficiency volume diffractive elements in photo-thermo-refractive glass," United States Patent 6,673,497 (2004).
[147] L. A. Siiman, Ultrashort Laser Pulse Interaction with Photo-Thermo-Refractive Glass, Ph.D. Thesis, University of Central Florida (2008).
[148] V.A. Borgman, L.B. Glebov, N.V. Nikonorov, G.T. Petrovskii, V.V. Savvin, and A.D. Tsvetkov, "Photo-thermal refractive effect in silicate glasses," Soviet Physics-Doklady 34, 1011-1013 (1989).
[149] A.E. Siegman, Lasers (University Science, Mill Valley, Calif.,1986).
[150] ISO 11146:1999, "Lasers and laser-related equipment – Test methods for laser beam parameters – Beam widths, divergence angle and beam propagation factor".
[151] T.F. Johnston, Jr., "Beam propagation (M2) measurement made as easy as it gets: the four-cuts method," Applied Optics 37, p. 4840-61 (1998).
[152] Ammar Hideur, Thierry Chartier, Cafer Ozkul, Francois Sanchez, "Dynamics and stabilization of a high power side-pumped Yb-doped double-clad fiber laser," Optics Communications, 186, 4-6, pp. 311-317 (2000).
[153] D. Strickland and G. Mourou, "Compression of amplified chirped optical pulses" Opt. Commun. 56, 219 (1985).
[154] Treacy, E., "Optical pulse compression with diffraction gratings," Quantum Electronics, IEEE Journal of, vol.5, no.9, pp. 454-458, Sep 1969.
[155] A. Boskovic, M. J. Guy, S. V. Chernikov, J. R. Taylor, and R. Kashyap, "All-fibre diode pumped, femtosecond chirped pulse amplification system," Electron. Lett. 31, 877-879 (1995).
[156] A. Galvanauskas, M. E. Fermann, D. Harter, K. Sugden, and I. Bennion, "All-fiber femtosecond pulse amplification circuit using chirped Bragg gratings," Appl. Phys. Lett. 66, 1053-1055 (1995).
[157] A. Galvanauskas, M. E. Fermann, "Optical pulse amplification using chirped Bragg gratings", US patent 5,499,134, March 12, 1996.
[158] Leonid B. Glebov, Emilie Flecher, Vadim I. Smirnov, Almantas Galvanauskas, Kai-Hsiu Liao, "Stretching and compression of laser pulses by means of high efficiency volume diffractive gratings with variable periods in photo-thermo-refractive glass", US patent 7,424,185 B2, Sep. 9, 2008.
[159] K.-H. Liao, M.-Y. Cheng, E. Flecher, V.I. Smirnov, L. Glebov, and A. Galvanauskas, "Large-aperture chirped volume Bragg grating based fiber CPA system," Opt. Express 15, 4876-4882 (2007).
[160] G.Chang, C.-H. Liu, K.-H. Liao, V.Smirnov, L.Glebov, and A.Galvanauskas, "50-W Chirped-Volume-Bragg-Grating Based Fiber CPA at 1055-nm", 20th Annual Solid State and Diode Laser Technology Review, SSDLTR-2007 Technical Digest, FW1-11 (2007).
[161] G. Chang et al, "32 W Femtosecond Yb-Fiber CPA System Based on Chirped-Volume-Bragg-Gratings," paper CThB3, CLEO/QELS (2008).

[162] L. Lepetit, G. Cheriaux, and M. Joffre, “Linear techniques of phase measurement by femtosecond spectral interferometry for applications in spectroscopy”, J. Opt. Soc. Am. B 12, 2467 (1995).
[163] R. Trebino and D. J. Kane, "Using Phase Retrieval to Measure the Intensity and Phase of Ultrashort Pulses: Frequency-Resolved Optical Gating," J. Opt. Soc. Am. A 11, 2429-2437 (1993).
[164] S. Linden, H. Giessen, and J. Kuhl, “XFROG – a new method for amplitude and phase characterization of weak ultrashort pulses.” Phys. Status Solidi B 206, 119–124 (1998).
[165] N. Nishizawa and T. Goto, “Experimental analysis of ultrashort pulse propagation in optical fibers around zero dispersion region using cross-correlation frequency resolved optical gating,” Opt. Express 8, 328–334 (2001).
[166] J. M. Dudley, X. Gu, L. Xu, M. Kimmel, E. Zeek, P. O’Shea, R. Trebino, S. Coen, and R. S. Windeler, “Cross-correlation frequency-resolved optical gating analysis of broadband continuum generation in photonic crystal fiber: simulations and experiments,” Opt. Express 10, 1215–1221 (2002).
[167] A. Efimov, A. J. Taylor, “Cross-correlation frequency-resolved optical gating for studying ultrashort-pulse nonlinear dynamics in arbitrary fibers,” Appl. Opt. 44 4408–4411 (2005).
[168] S. Santran, M. Martinez-Rosas, L. Canioni, L. Sarger, L. N. Glebova, A. Tirpak, and L. B. Glebov, "Nonlinear refractive index of photo-thermo-refractive glass," Optical Materials, 28, 401-407 (2006).